RADIATION AND DYNAMICS OF THE ATMOSPHERE OF MARS

by

Alan M. Gadian
Atmospheric Physics Group
Imperial College of Science and Technology

A thesis submitted for the degree of Doctor of Philosophy in the University of London.

August 1976

ABSTRACT

Using data collected by Mariner 9 and Mars 3, the large scale dynamics and radiative properties in the Martian winter hemisphere are studied in this thesis.

A tephigram is produced which helps to determine the cloud composition and is useful when discussing the stability of the measured temperature profiles. These temperatures are generally larger than those computed theoretically using the 14/15 micron absorption band of carbon dioxide, of which the atmosphere is mainly composed. Comparing the observed and theoretical temperatures enables one to calculate, by means of the Emden approximations, the necessary heat fluxes required to maintain the measured profiles. In the winter hemisphere the dynamics are responsible for a part of this difference.

The quasi-geostrophic potential vorticity equation, with Newtonian damping to account for the rapid radiative cooling in the carbon dioxide atmosphere, is solved numerically. Values for the phase speed and wave-number of the most rapidly growing wave are compared with measurements from the Mariner 9 photographs. Heat fluxes are obtained using the transfer coefficient theory, since the eigenvalue method used cannot provide magnitudes for the heat fluxes.

Finally, topographically forced stationary long waves on a spherical planet are also studied. Heat flux magnitudes and the temperature structures in the vertical, are obtained for different Martian conditions: again the equations are solved numerically. This thesis gives an insight into some of the important large scale dynamical processes in the winter hemisphere.

LIST OF CONTENTS

		Page No.
ABSTRACT		2
CHAPTER 1:	INTRODUCTION	
1.0	Introduction	6
1.1	The planet Mars	6
1.2	The topography of Mars	7
1.3	The atmosphere of Mars	11
1.4	Previous work	11
CHAPTER 2:	THE VERTICAL TEMPERATURE STRUCTURE AND THE CORRESPONDING RADIATIVE EQUILIBRIUM PROFILES	
2.0	Introduction	16
2.1	Tephigram	16
2.2	Lee waves and the tephigram	19
2.3	The radiative equilibrium temperature profile	24
CHAPTER 3:	BAROCLINIC EDDIES: A THEORETICAL BACKGROUND	
3.0	Introduction	33
3.1	Small amplitude waves on a Beta plane	33
3.2	Computation	44
CHAPTER 4:	ACCURACY ANALYSIS OF THE COMPUTATION AND THE EFFECT OF NEWTONIAN DAMPING	
4.0	Introduction	46
4.1	Comparison with the analytic solutions for the Eady Model	46
4.2	Convergence of solutions when the density and Beta effects are included	48
4.3	The effect of the vertical variation of the static stability	48
4.4	Convergence of solutions with Newtonian damping	51
4.5	Accuracy and convergence of the model with F=0 as an upper lid	51
4.6	Effect of radiation on the Eady wave	52
4.7	General effects on the phase speed and growth rate by Newtonian damping	54

CHAPTER 5: RESULTS OBTAINED FROM THE BAROCLINIC EDDY MODEL

5.0 Introduction 57

5.1 The effect of the density scale height and the Beta parameter on the earth 57

5.2 Newtonian damping on the earth's baroclinic eddies 57

5.3 The effect of static stability, B, on the earth 61

5.4 Radiational damping used in the computation for Mars 64

5.5 The static stability, B, and discussion of the Green model on Mars 65

5.6 Solutions for F=0 as the upper boundary condition 76

5.7 General comments 79

5.8 Baroclinic heat fluxes 80

5.9 Concluding comments 82

CHAPTER 6: THE THEORY OF LONG TOPOGRAPHICALLY FORCED WAVES ON MARS

6.0 Introduction 84

6.1 The equation 84

6.2 Boundary conditions 87

6.3 Comparison of numerical results with analytic solutions 88

6.4 Derivation of heat fluxes 91

CHAPTER 7: THE RESULTS OF THE LONG WAVE THEORY

7.0 Introduction 93

7.1 An analysis of the topography 93

7.2 Static stability, the wind field and the radiational damping parameters 95

7.3 Effect of the modified Boussinesq set equations on the results 97

7.4 Results 97

7.4.1 Varying the height of the upper lid 105

7.4.2 Varying the static stability 106

7.4.3 Effect of Newtonian radiative damping 106

7.4.4 Different wind profiles 108

7.4.5 Other modifications 109

7.5 Concluding remarks 109

CHAPTER 8: SUMMARY 111

REFERENCES 113

ACKNOWLEDGEMENTS 116

APPENDIX A.1

CHAPTER 1: INTRODUCTION

1.0 Introduction

Physical laws and processes are often discovered only by keeping some parameters of the system constant and varying others in a critical way. By examination of other atmospheres we will learn more about these important principles which govern motions of these atmospheres and hence give greater insight into the circulations found on the earth.

This next section contains a brief summary of the information known about the Martian atmosphere. Mariner 9 and Mars 3 are the main sources of data for the work in this thesis, but it must be noted that there is still controversy about, for example, the composition of the atmosphere. In addition earth based radar information has been used in the production of the surface topographical map.

1.1 The planet Mars

The planet Mars has a mass of 10.8% of the earth's mass with a value for the acceleration due to gravity, g, of 3.76 ms^{-2}. Although the mean radius of the Martian orbit around the sun is approximately 2.3×10^{8}km compared with the earth's mean orbital radius of about 1.5×10^{8} km, thus giving a Martian solar constant of 610 Wm^{-2}, since the albedo of the planet and its atmosphere is about 0.15, the actual radiation absorbed is the same as on earth and, in fact, the same as on Venus. However the resulting meteorology is different for each planet and in this thesis we aim to discuss some aspects of the Martian circulation. These solar fluxes give a Martian radiative equilibrium temperature of about 220^{o}K. The planetary rotation period is 24 hours 32 mins and the spin axis is inclined at about 65^{o} to the orbital plane, both similar to the terrestrial values. The planet's orbital period is, however, 687 days and the radius of Mars is about 3,380 km.

1.2 The topography of Mars

The topography of Mars shows many significant features which affect the atmospheric circulation. Direct occultation measurements of the surface and of the mean atmospheric surface pressure (6.1 mb surface) indicate that, because of different observed eccentricities, then either the polar atmospheric surface pressure is greater than the corresponding equatorial pressure, or equivalently there is a range of mountains about 4 km high, decreasing in height with increasing latitude (Runcorn, 1973). Analysis of the motion of Martian satellites gives good agreement, as it should, with the eccentricity found from measurements of the mean 6.1 mb. atmospheric surface pressure. Figures 10 and 11 give the height contours above the mean 6.1 mb, atmospheric surface and an 8×8 harmonic analysis of the height contours, both being taken from Christensen (1975). It is interesting to note that the mean surface height is about 3 km lower in the northern hemisphere. The four large volcanoes, around 120^{o} longitude and 0^{o} latitude must present a large obstruction to the mean circulation in the northern hemisphere. The mountains and basins as shown on the harmonic analysis, Figure 11, also must have a great effect on the large scale flow. The importance of the mountains is further demonstrated since the volcanoes are the same order of magnitude as the density scale height of about 12 km, and the amplitudes of the longitudinal fourier components of the surface topography often exceeds 1 km for wavenumbers less than eight. This is explained in more detail in Chapter 6, but the comparable terrestrial amplitudes are only 200 metres. In Chapter 7 the resulting heat transport of large scale topographically forced flows will be discussed. Much of this study has tended to be concentrated on the northern hemisphere winter, since the winter hemisphere has a larger pole to equator temperature difference which I think results in more interesting dynamics which can be verified by observable cloud patterns.

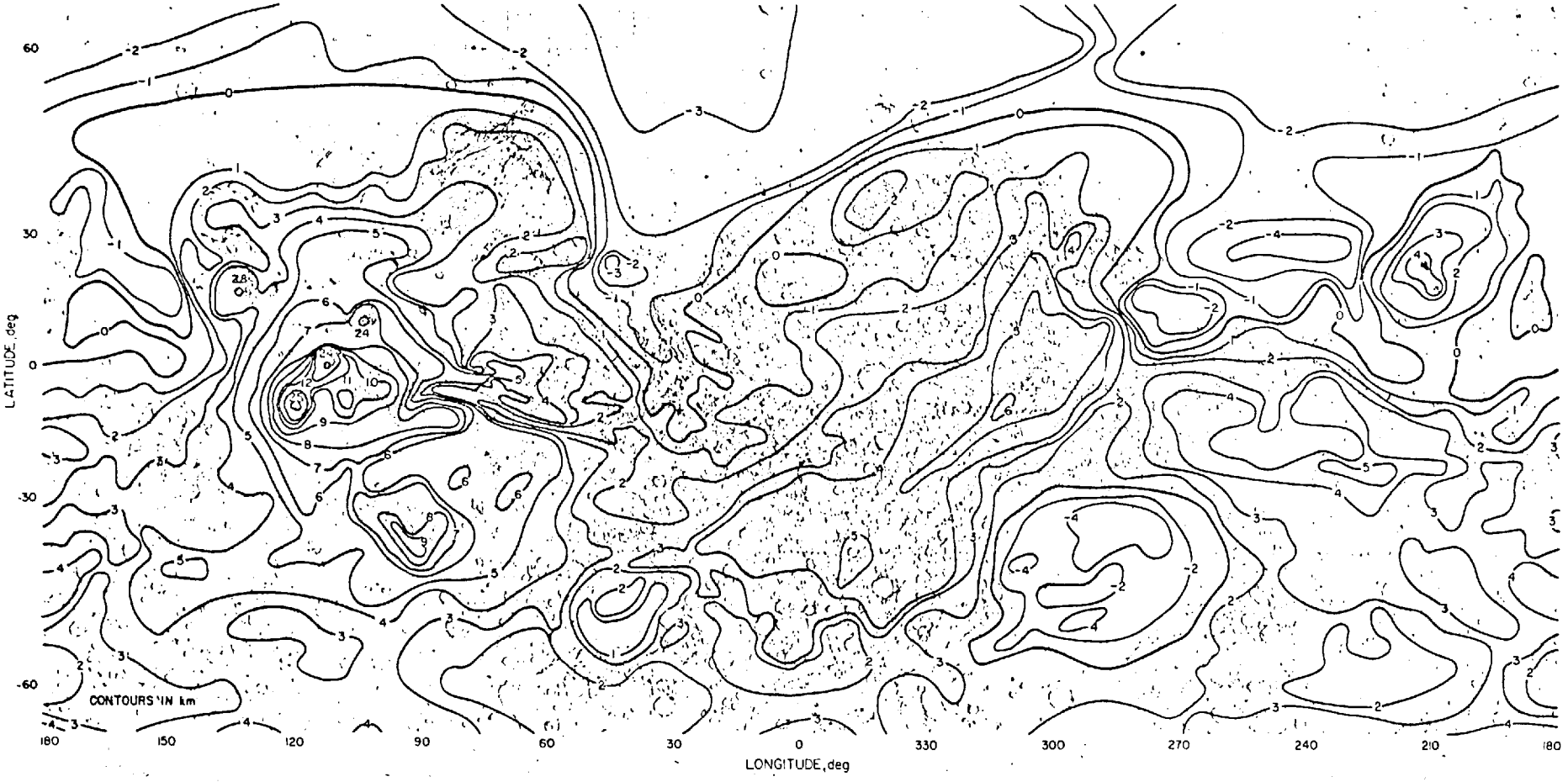

Figure 10: Topographical map produced with data from Mariner 9. The contours are shown above the 6.1mb isobaric surface (after Christensen, 1975).

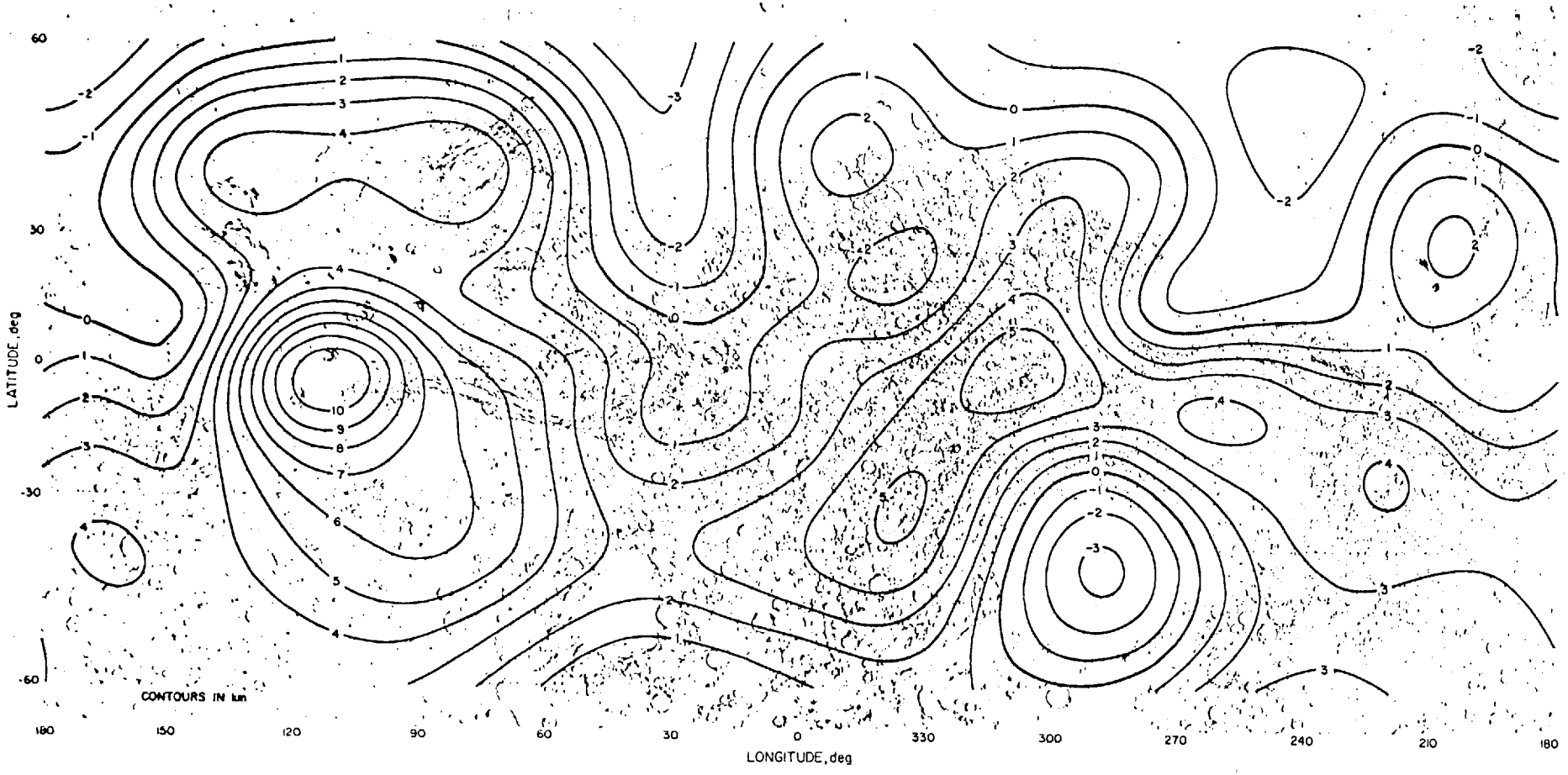

Figure 11: 8x8 harmonic fit to the topographical data on Mars. Contours are shown above the 6.1 mb isobaric surface (after Christensen, 1975).

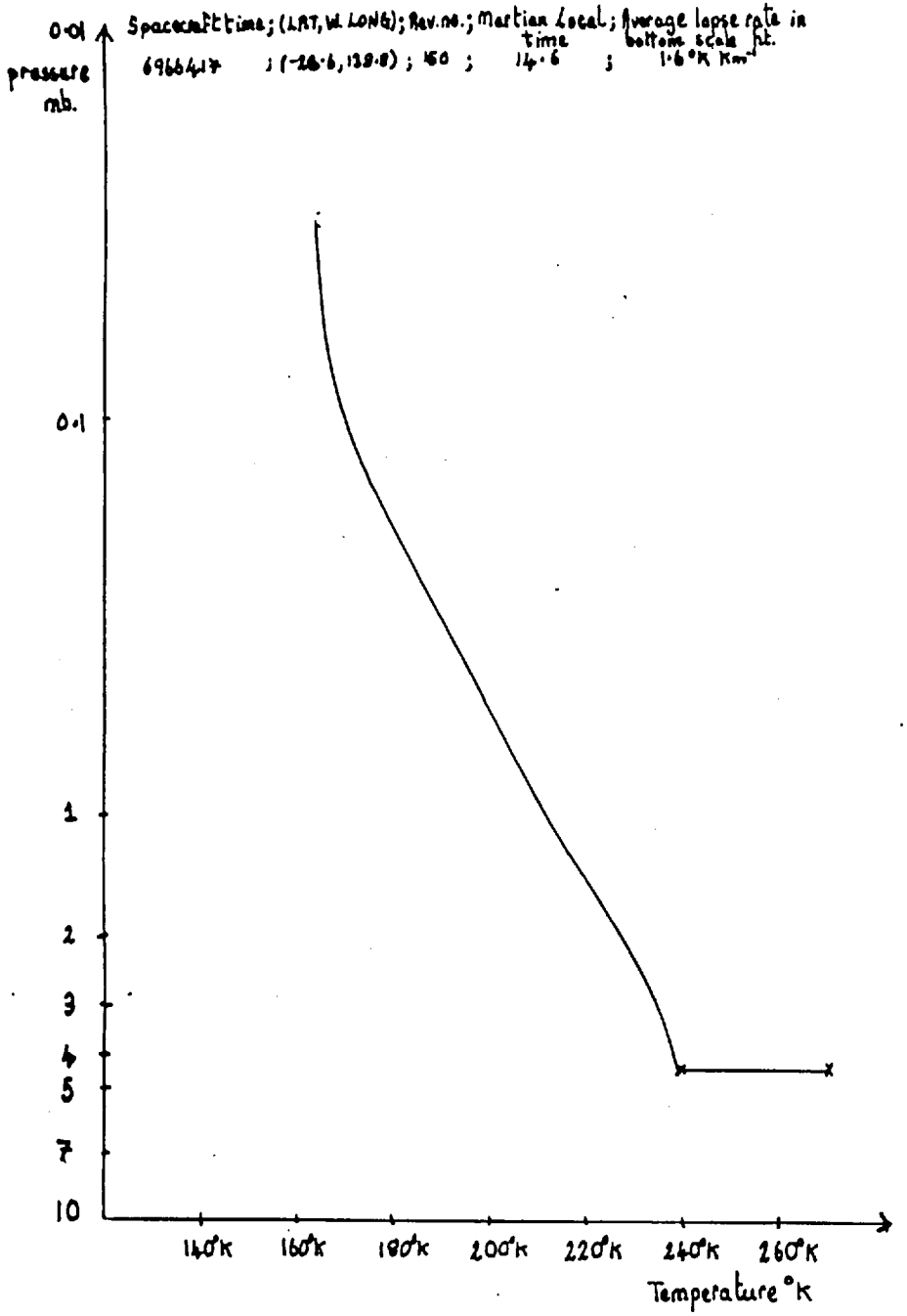
Spacecraft time; (LAT, W. LONG); Rev. no.; Martian Local time; Average lapse rate in bottom scale ht.
6966417 ; (-26·6, 139·8) ; 150 ; 14·6 ; 1·6°K Km⁻¹
0·01
pressure mb.
0·1
1
2
3
4
5
7
10
140°K
160°K
180°K
200°K
220°K
240°K
260°K
Temperature °K

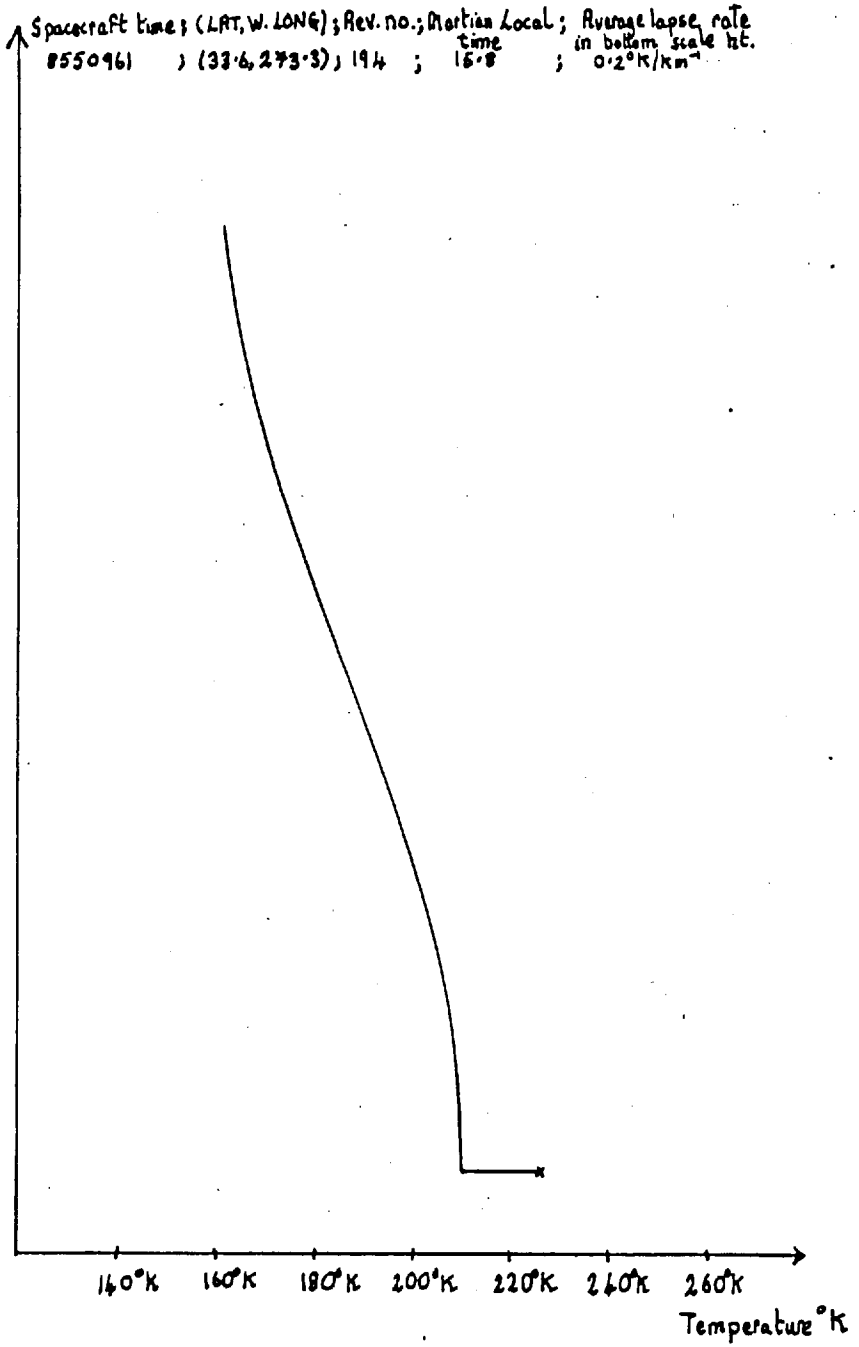
Spacecraft time; (LAT, W. LONG); Rev. no.; Martian Local time; Average lapse rate in bottom scale ht.
8550961 ; (33·6, 273·3) ; 194 ; 15·8 ; 0·2°K/Km⁻¹
140°K
160°K
180°K
200°K
220°K
240°K
260°K
Temperature °K

1.3 The atmosphere of Mars

The atmosphere, according to Hide (1976), is composed of over 70% carbon dioxide, while the remainder is probably predominantly argon. As explained in Chapter 2, Mars 3 measured that about 30% of the atmosphere is argon. With a mean surface atmospheric pressure of 6.1 mb, the dry adiabatic lapse rate is about $4.5^{\circ}C\ km^{-1}$. Mars 3 measured 60-70 precipitable micrometers of water vapour as compared with the Mariner 9 values of 10-20 micrometers (N.A.S.A. 1972). No water vapour has been found in the winter polar regions although ozone has been detected. Assuming these measurements are valid, then the water vapour content of the atmosphere must vary greatly. The polar ice caps are composed of a mixture of carbon dioxide and water ice and their size alters from winter to summer (Cutts, 1973). Soderblom (1973), using the Mariner 9 data, indicates that the south polar ice cap increases from less than 10^5 square kilometres area in summer to more than 10^6 square kilometres in early spring: with the ice sheet extending to about 70° latitude in winter and about 82° latitude in the summer. As a result there must be a mass transfer of gas every half year, from one pole to another.

Figures 12 and 13 are two typical Martian temperature profiles, one in the southern (summer) and Figure 13 in the northern (winter) hemisphere. These were produced from Mariner 9 data, by using the radiance of certain wavelengths of the 14/15 micron carbon dioxide band which, because of the transmission properties of the atmosphere, give temperatures for certain depths in the atmosphere. The results are claimed to be accurate for half a scale height and it is interesting to note that they produce a temperature discontinuity at the ground because of the inability to determine the actual temperature structure over the bottom few kilometres.

1.4 Previous work

Although it is only recently that spacecraft have provided some information regarding Mars and its atmosphere, there is already a large

amount of literature available. Thus in the following paragraphs we have mentioned some of the more important papers in order to provide a background to this study. Other relevant papers not discussed here will be mentioned in the corresponding sections.

In 1969, Leovy and Mintz produced a two level general circulation model of the Martian atmosphere. In the next few paragraphs some of their assumptions and results of their calculations are discussed. Using the hydrostatic equation, the horizontal momentum equation, thermodynamic and continuity equations but with no topographical features, they simulate the atmospheric circulation starting from rest and continuing for 25 days. They assume that the effects of clouds are negligible but include sublimation of carbon dioxide at the poles and the absorbtion of solar and infra-red radiation in the atmosphere and at the ground. Using sigma co-ordinates there is a free surface, i.e. $\frac{Dp}{Dt} = 0$ as the upper boundary condition at 0.62 mb. The lower boundary occurs at 7.5 mb and includes an order of magnitude frictional component. Two computations were made, one simulating the summer solstice and the other the equinox conditions.

In the solstice there are strong westerly winds of 70 ms^{-1} at 13 km and 30 ms^{-1} at 3 km in the winter hemisphere, and easterlies with maximums of 15 ms^{-1} and 25 ms^{-1} at lower and upper levels. In the equinox experiment there are westerlies of 25 ms^{-1} and 10 ms^{-1} at the upper and lower levels in both mid-latitude belts with weak easterlies at the equator. Calculated temperatures indicate that the lapse rate should be about 3/4 of the dry adiabatic lapse rate in summer, but almost isothermal in the winter hemisphere. At the equinox the lapse rate is half of the adiabatic between $\pm 50^{o}$ latitude. The polar ice caps extend to 55^{o} latitude in the winter and 77^{o} latitude in the summer hemisphere in the solstice experiment. These large polar ice caps are necessary to provide sufficient latent heat of sublimation for carbon dioxide, to satisfy the infra-red cooling of the polar atmosphere. These polar ice caps are much larger than observed. There could be, as Leovy and Mintz point out, an underestimation of the

poleward heat flux which would increase the requisite amount of condensation of carbon dioxide required at the winter pole. I think the poleward heat transfer could be modified by the effect of topographically (and thermally) forced long waves, which I shall discuss in Chapters 6 and 7.

The mass transport, at solstice, towards the northern winter hemisphere in the model is allowed by having a Hadley type cell across the equator, with a larger northward wind at the upper level than the southward component of the meridional wind at the lower level. Diurnal fluctuations were thought by the authors to be inaccurate because the upper boundary at 0.62 is not very high, but Pirraglia and Conrath (1974) show that the Mariner 9 results are in close agreement with the theoretical values from the model. Thus, in conclusion, this model is useful despite the major shortcomings arising from ignoring the topographical detail, and hence, the miscalculation of the meridional heat flux.

A study of the thermal and dynamical structure of the Martian lower atmosphere was made by Gierasch and Goody in 1968. By consideration of the 14 micron carbon dioxide band, a temperature profile is produced with a superadiabatic layer over the bottom kilometre. Purely vertical convection will reduce the depth of the superadiabatic layer and generally produce an almost adiabatic lapse rate in the bottom scale height. However measurements from Mariner 9 indicate that the summer lapse rate is slightly more than half the dry adiabatic, as predicted by Leovy and Mintz. Despite this since the Goody model has played an important role in our comprehension of atmospheric lapse rates, we shall discuss some of the assumptions and results.

In this problem the surface pressure is assumed to be 4.9 mb for an atmosphere consisting of carbon dioxide entirely. For a pole to equator surface temperature difference of $70^{o}K$ and a corresponding air surface temperature gradient of $50^{o}K$ there would be a mean zonal wind of about $40\ ms^{-1}$. Mariner 9 winter hemisphere photographs of lee waves indicate winds of comparable magnitude, as will be mentioned later in this chapter.

With a ground diurnal temperature variation of 70°K and a radiational damping time scale for the atmosphere of 5 days, they produce a value for the surface air temperature change of about 3°K and a tidal wind component of about 2 ms^{-1} at the ground. Hanel et.al. (1972) give values of surface air temperature variation of about 30°K with surface diurnal temperature differences of about 100°K. However if a slightly increased surface temperature change and a faster radiative damping time constant of 1 day is used then the theoretical air temperature variation is approximately the same as observed.

Pirraglia and Conrath (1974), using a tidal equation produced from the continuity and momentum equations, calculate the surface diurnal zonal winds of about 10-20 ms^{-1} . At one scale height diurnal temperature variations of 30°K were measured by Mariner 9 and used to calculate surface atmospheric amplitudes of up to 0.3 mb. This suggests that the application of Gierasch and Goody's tidal theory, although useful to a first approximation, is not very accurate. In the later sections of Gierasch and Goody's paper there is discussion of turbulent heat transfer and convection, which is not discussed here mainly because it is based on assuming slightly unstable profiles which have not been found in any of the Mariner 9 measurements.

In the final paragraphs of the paper, the authors discuss the formation of cloud. The frost point lapse rate, as deduced from the Clausius Clapeyron equation is about 1.2°K km^{-1} , assuming that the latent heat of freezing of carbon dioxide is 450 Joules kg^{-1} , and with a value for the frost point at the ground of 145°K. Thus they argue that carbon dioxide clouds could form at the surface at night. As on the earth, since the frost point lapse rate is less than the adiabatic lapse rate, then ice would not be formed in downward moving air.

Lee waves, now thought to be water ice, were not mentioned by Gierasch and Goody. Pirraglia (1975) studies the lee waves photographed

on Mars by Mariner 9. Scorer and Wilkinson's (1969) analysis is extended by Pirraglia in order to introduce horizontal dimensions of the craters. Using the wedge shape nature of the observed wave patterns, the author is able to show that lee waves at 50^{o}N give similar wind speeds to those produced in the Leovy and Mintz numerical model. We shall discuss lee waves further in the next Chapter. Gierasch and Sagan (1971) assess some of the wind regimes which could be produced by large scale topographic features since Sagan and Pollack (1969) show that these could be contributory causes of dust storms. However in this thesis we have not discussed the formation of these dust storms.

CHAPTER 2: THE VERTICAL TEMPERATURE STRUCTURE AND THE CORRESPONDING RADIATIVE EQUILIBRIUM PROFILES

2.0 Introduction

This chapter provides further background to the dynamical study of the Martian atmosphere, relating the general temperature structure to a tephigram. This tephigram is also used to discuss the composition of lee wave clouds and suggests that, from the Mariner 9 data, there should not be purely vertical convective clouds on Mars. The latter part includes a comparison of the actual profiles with theoretical radiative equilibrium profiles giving values for the atmospheric cooling rates.

2.1 Tephigram

To obtain a clearer understanding of the nature of the cloud condensates a tephigram is produced assuming that the atmosphere is composed totally of carbon dioxide with a little water vapour. Estimates from data taken by Mars 7 indicate that the argon content is probably 35 ± 10% (Ksanfomalitee, 1974). Since the molecular weights of carbon dioxide and argon are almost equal (44 and 40 respectively), the assumptions that the gas constant, R, has the carbon dioxide value is reasonably accurate. In order to draw a tephigram, knowledge of C_p, the specific heat at constant pressure, is also required. Errors are incurred by assuming that the specific heat of the atmospheric gas mixture would be the same as for carbon dioxide since C_p for argon is almost half the carbon dioxide value (National Bureau of Standards, 1955). The specific heats for these gases at low temperatures and pressures are not very accurately known and thus we argue that this short study does not warrant extra consideration of argon's influence. Hide (1976) quotes a value of C_p for the atmosphere of 850 J kg^{-1} k^{-1} which is low compared with those magnitudes for carbon dioxide given in the U.S. National Bureau of Standards. However if argon is included in the atmospheric composition

then this figure is more accurate. We shall have to wait to discover whether this one Russian measurement of argon is verified by other spacecraft arriving this year.

Thus it is possible that the values of C_p/R used in the following equation to produce isotherms of potential temperature θ, could be in error by about 20% when compared with the actual atmosphere.

$$\theta = T\left(\frac{p_o}{p}\right)^{R/c_p} \qquad (2.0)$$

where p_o is the atmospheric pressure at a surface, with temperature T and the corresponding pressure p. Figure 21 illustrates the final result with temperature and log potential temperature forming the ordinate and abscissa. The line II' is the plot of the vapour pressure of solid carbon dioxide against temperature. On and to the left of this line a parcel of carbon dioxide would solidify, providing there is no supersaturation. The pecked straight lines are isopleths of saturated mixing ratio of water r_s. Thus r_s of 10^{-3} corresponds to 1 gram of water vapour to 1 kilogram of atmosphere. The associated saturation adiabats are the curved asymptotic lines. Mariner 9 measured only small amounts of water vapour, with 10-20 precipitable micrometers over most of the surface and none at the winter (north) pole (N.A.S.A., 1972). This corresponds to a mixing ratio of $3\text{-}7\times10^{-4}$ if the water vapour is concentrated in the lowest 3 mb and half that value is equidistributed through the atmospheric depth. The Russian Mars 7 mass spectrometer measured about 3-5 times the water vapour content. It is difficult to determine where this spacecraft sampled the atmosphere, but it appears to have landed near the equator (Ksanfomalitee, 1974). If these results are correct then water vapour is much more common than previously thought, but it will still have little effect on the dynamics since the latent heat release of a parcel following a pseudo saturated adiabat for these mixing ratios is small, i.e. the temperature difference between taking a parcel of gas on a dry adiabatic compared with a pseudo-

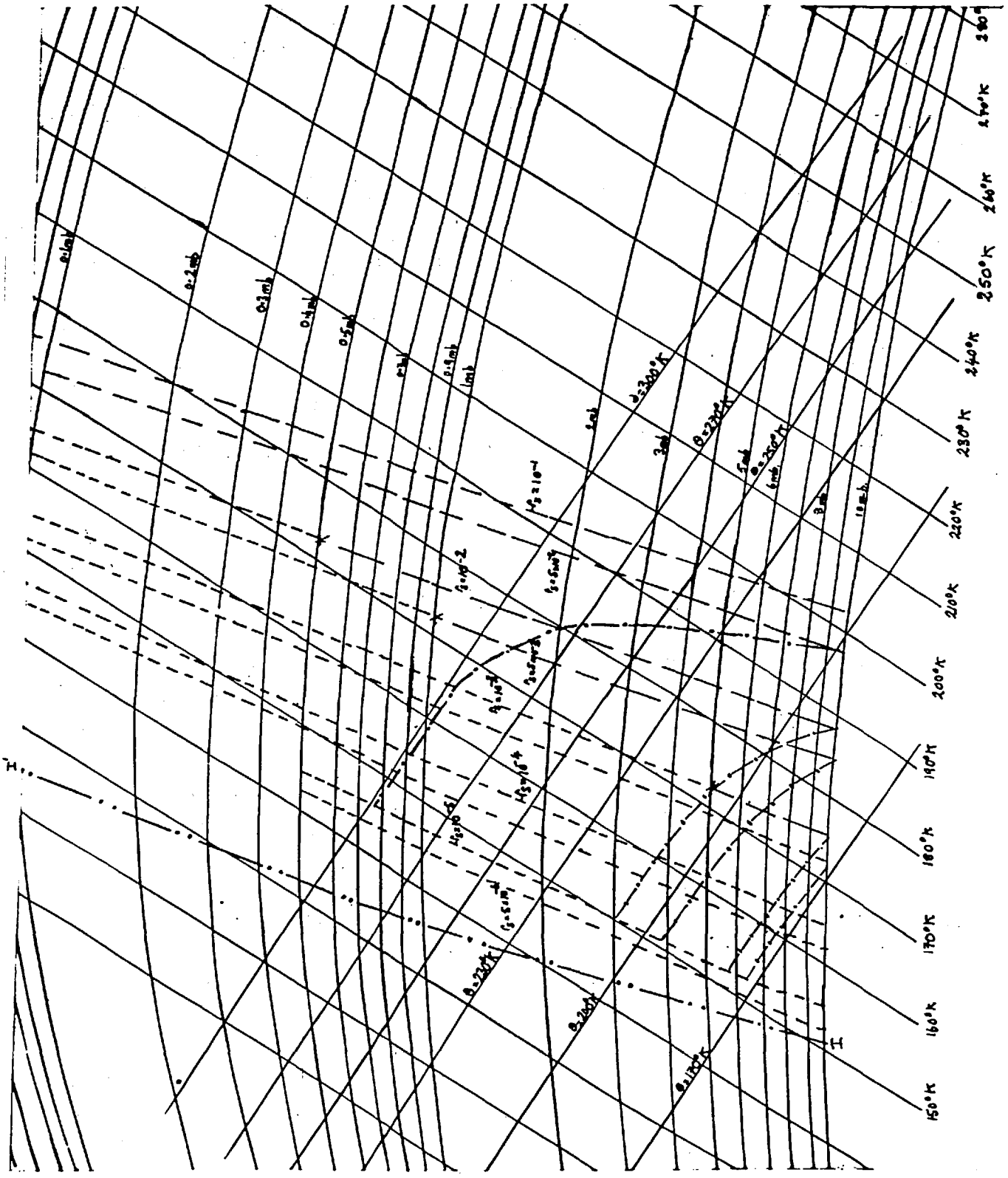

Figure 21: A tephigram for Mars, assuming a carbon dioxide atmosphere. The pecked lines correspond to saturated mixing ratios, r_s, of water vapour. The line II' is the vapour pressure curve for solid carbon dioxide. The solid perpendicular lines indicate temperate and potential temperature θ. The pseudo-saturated adiabats, and the isobaric curves are also shown.

saturated adiabat, for typical mixing ratios, is small.

2.2 Lee waves and the tephigram

The tephigram may be used to plot the temperature profiles obtained by the Mariner 9 spacecraft (see appendix). When we consider the lee waves corresponding to the photograph Figure 22, we find there is a surface brightness temperature as measured by the infra-red radiometer of 196°K and corresponding temperature profile as given on Figure 23. Although the temperature profile was measured about 40 km from the centre of the photograph, we have assumed that this profile is representative of the stability in the lee wave pattern. Figure 24 explains the notation used to describe the data obtained for the photographs. With a solar angle of 145° and a north angle of 265°, the lee wave pattern is observed at the bottom edge of the photograph. Thus the lee wave pattern indicates a westerly wind, with a wavelength of about 50-55 km.

Using the formula $\lambda^2 = gB/u^2$ (Leovy and Briggs, 1974) we have a value of u, the mean wind speed, of 75 ms^{-1} where g is the acceleration due to gravity, B is the static stability $1/\theta \cdot d\theta/dz$ and λ is $2\pi/$ wavelength. Most of the wavelengths, and hence mean wind speeds u, observed by Mariner 9 are smaller. For example, Figure 25, with the wave pattern in the centre left of the picture, gives a mean wind speed of 40 ms^{-1}. These figures are consistent with the Leovy and Mintz (1969) numerical model and were used as a guide for the wind shear used later in the baroclinic eddy model. These photographs also supply information on the amplitude of these wave clouds, since the shadows cast by crests, combined with the solar illumination angle, give amplitudes of 4 and 2 km for Figures 22 and 25 respectively. Since the shape of the crests, even on the raw photographs are accurately outlined on the following crests, then these are not shadows of clouds on the ground but clouds on clouds. In addition, if these were shadows on the ground, we should expect to see surface features, which are not observed in the centre of the patterns.

Figure 22: A Mariner 9 photograph with a large lee wave pattern in the centre bottom of the picture, with the following data parameters.

	Latitude	Longitude
U.L.	60.1°	230.5°
U.R.	57.5°	199.0°
L.L.	47.3°	227.5°
L.R.	45.70°	205.1°

Rev. 206
D.A.S. time → 8983144
Viewing angle → 16.5°
Lighting angle → 75.10°
Martian local time → 15.9 hrs
North angle → 264.6°
Subsolar latitude → -4.1°
Sun angle → 145°

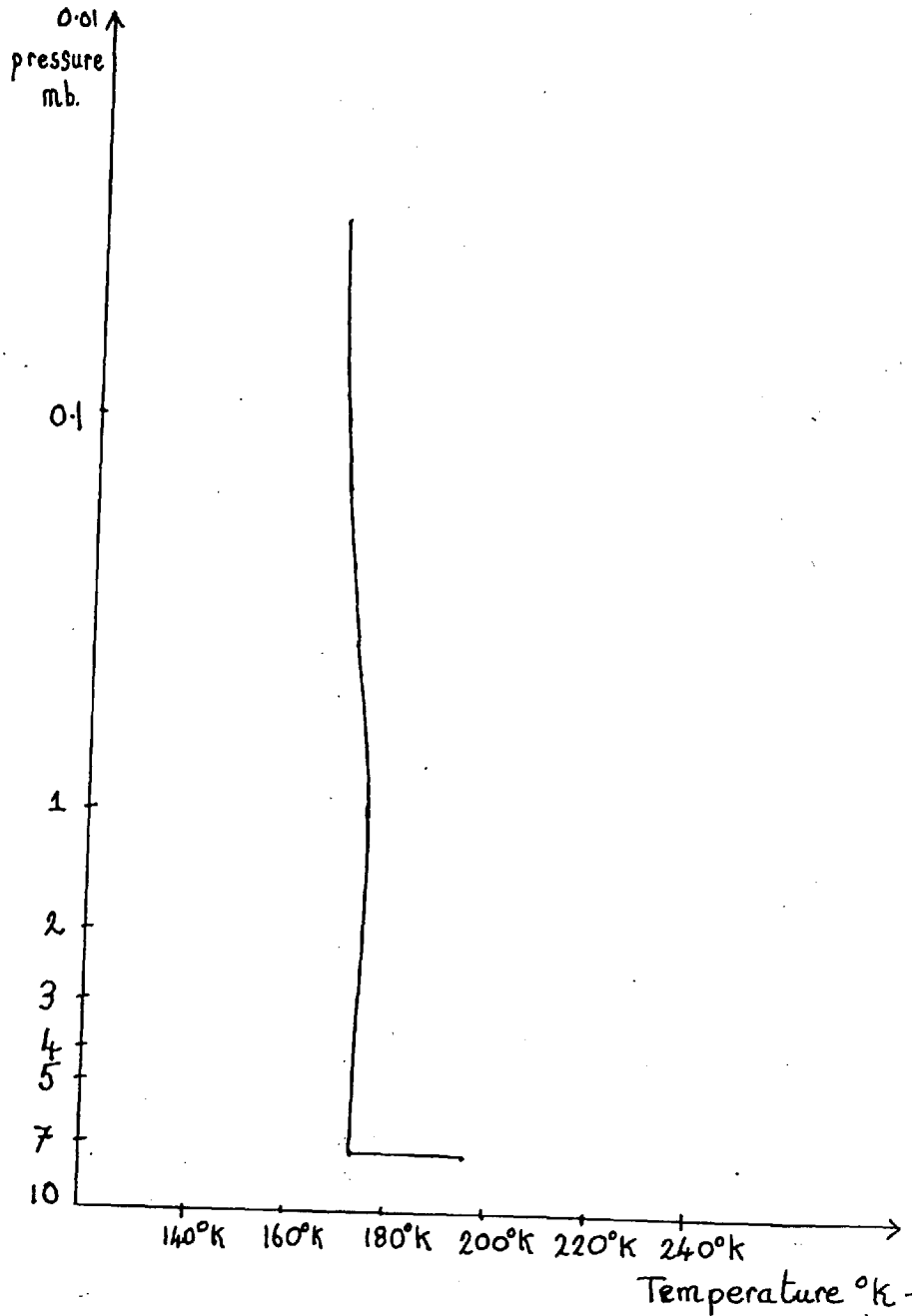

Spacecraft	(Lat, W. Long)	Rev. no.	Martian Local time	Average lapse rate in bottom scale ht.
8983140	(53·8, 214·5)	206	15·9	0·15° K km^{-1}

Figure 23. Graph of temperature against pressure, taken from Mariner 9 data.

Figure 24

PICTORIAL REPRESENTATION OF DATA PARAMETERS

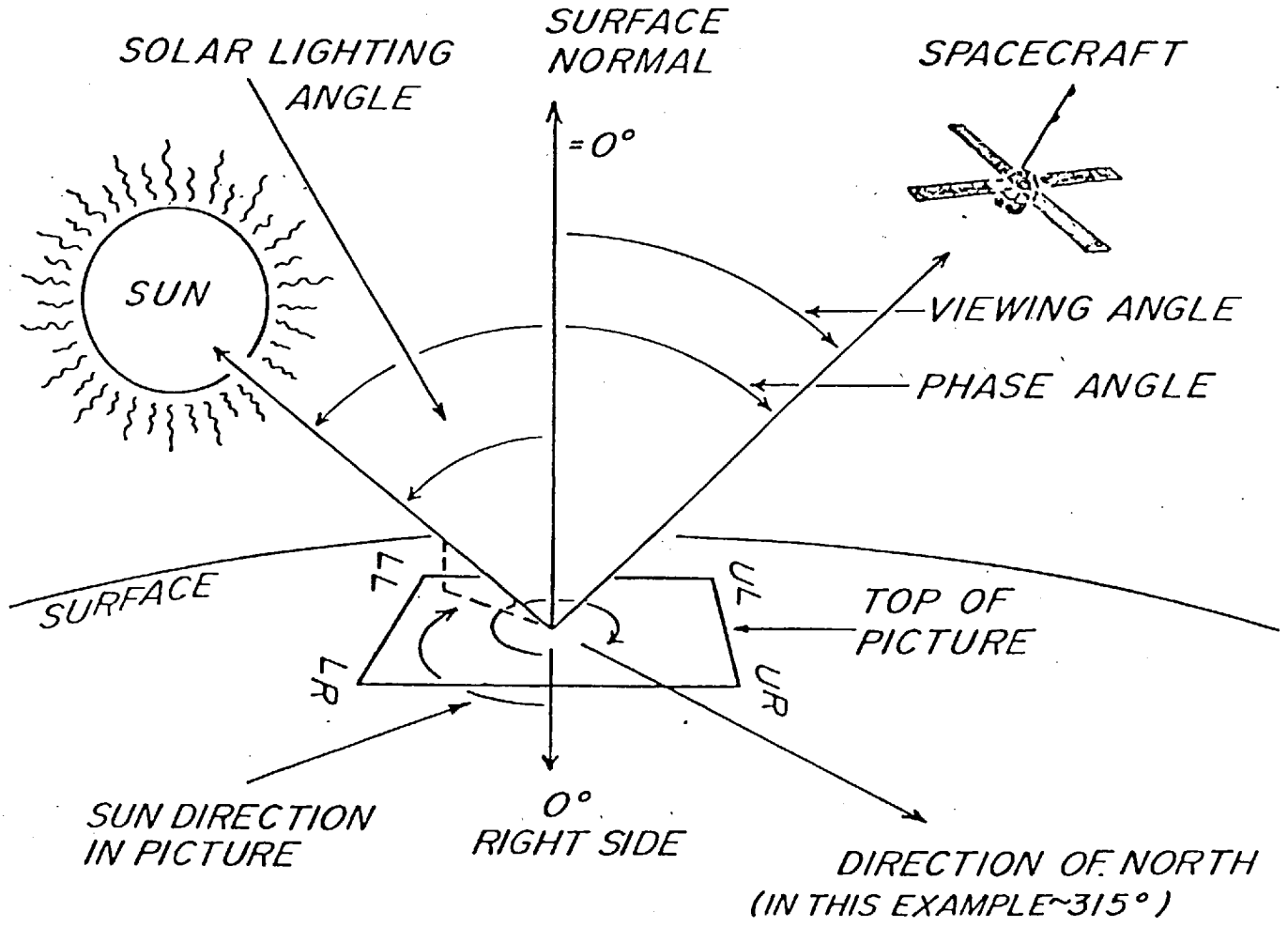

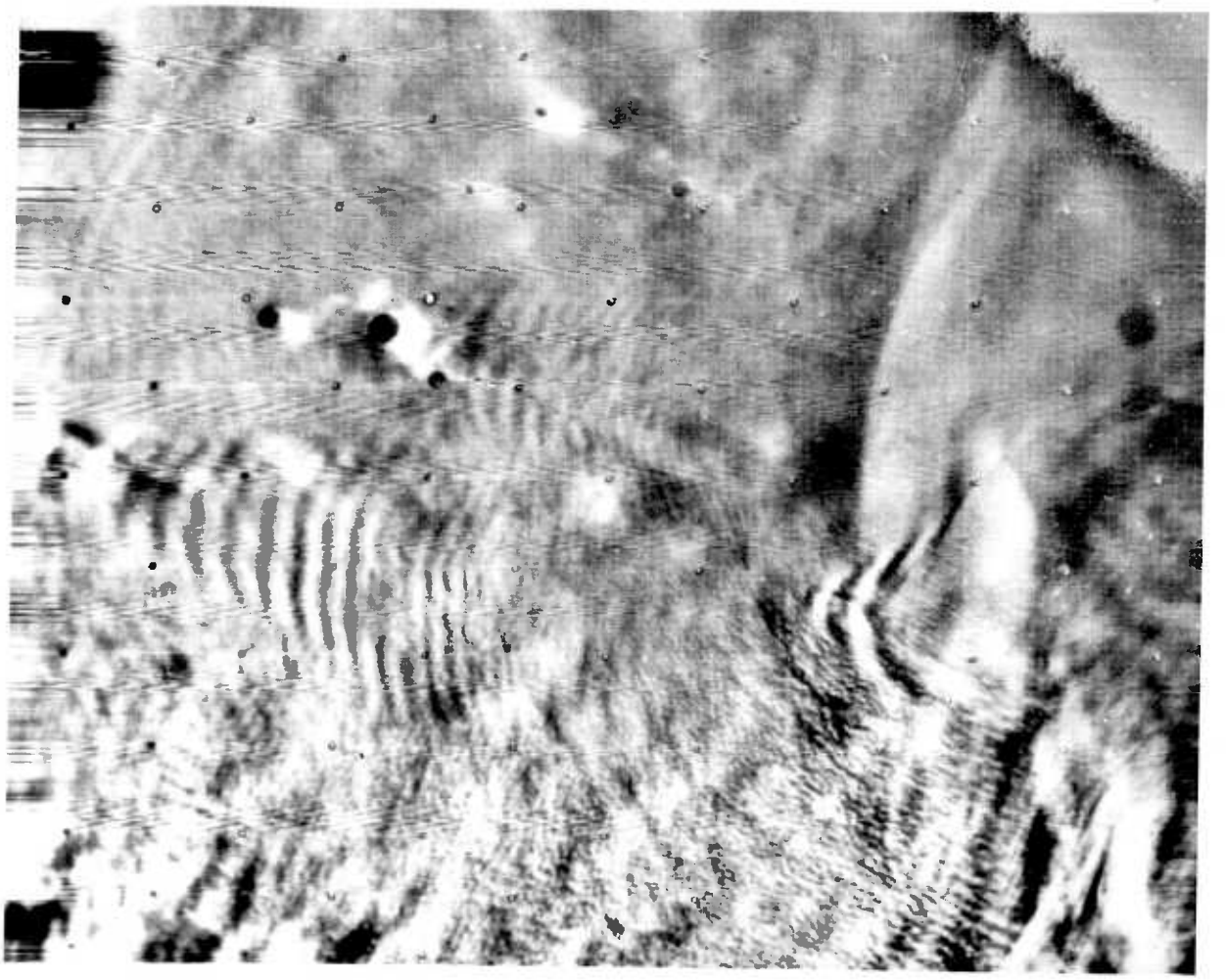

Figure 25: A Mariner 9 photograph of lee waves, centre left, observed on Mars.

	Latitude	Longitude
U.L.	66.3°	64.0°
U.R.	63.4°	21.9°
L.L.	52.3°	56.2°
L.R.	50.7°	30.2°

Rev. 205
D.A.S. time 8947234
Viewing angle → 25.1°
Lighting angle → 77.1°
Martian local time → 15.8 hrs
North angle → 266.0°
Subsolar latitude → -4.15°
Sun angle → 144°

The tephigram enables us to discuss the composition of these clouds. Assuming that the air rises adiabatically in these waves, then providing that the mixing ratio is greater than 10^{-6}, then from the tephigram these clouds will contain water ice crystals. Leovy and Briggs (1974) also reach this conclusion by arguing that carbon dioxide clouds, produced by adiabatic cooling, require surface winds in excess of 100 ms^{-1}. As mentioned in Chapter 1, Pirraglia (1975) discusses these waves in greater detail and produces similar winds to those found in the simple analysis above, and deduces that these lee waves are generally found between 10 and 15 km.

If more and accurate temperature profiles are obtained from the next Mariner spacecrafts, then the tephigram could be fruitfully used to consider if, for example, the markings on Figure 26 are vertical convection clouds. With the high measured surface temperatures of about 260°K at 10.45 a.m. local time, the lighter patches on the photograph could conceivably be cumulus type clouds, although the larger marks have a 100 km diameter. As the sublimation and boiling points of argon at Martian pressures are less than 100°K, there will be no condensation of this element on Mars. The tephigram emphasizes the stability of the temperature profiles in the appendix and this suggests that the markings on Figure 26 are not cumulus clouds. The patches could be small dust storms, but without further data, this is purely guesswork.

2.3 The radiative equilibrium temperature profile

Since carbon dioxide on Mars has a rapid radiative damping time (Goody and Belton, 1967), the temperature profiles are largely dominated by radiation. This section compares some of the actual temperatures obtained from Mariner 9, with the theoretical profiles produced assuming radiative equilibrium. The Emden approximation is used to estimate the cooling rate arising from the difference between Goody and Gierasch's (1967) radiative equilibrium profiles and those observed.

Figure 26: A Mariner 9 photograph of possible clouds, with the following data parameters:

	Latitude	Longitude
U.L.	38.9°	41.0°
U.R.	57.3°	30.5°
L.L.	35.1°	21.9°
L.R.	50.8°	8.8°

Rev. 444
D.A.S. time 12188377
Viewing angle → 22.70°
Lighting angle → 34.6°
Martian local time → 10.4 hrs
North angle → 334.7°
Subsolar latitude → 17.8°
Sun angle → 116°

Goody and Gierasch's (1967) calculation, with a 4.9 mb surface atmospheric pressure for a carbon dioxide atmosphere, uses the absorption properties of the 14/15 micron carbon dioxide band. Goody and Belton's (1967) calculations of the radiative relaxation times were used to produce the temperature profiles. Doppler broadening of the emission lines does not become important until about four density scale heights and so pressure broadening is used. At these and higher levels absorption due to ionization and dissociation of carbon dioxide are included in the calculation. With a 50% dilution of the atmosphere by adding argon or nitrogen, the temperatures are the same to within $1^{\circ}K$, although the geometric height may be incorrect due to a change in value of the density scale height. Thus we assume that if radiation is the only factor affecting the lapse rate, then there would be a good fit to the profile as given by Goody and Gierasch (1967). Different temperatures from theory and measurement will provide magnitudes for flux divergence which can be used to provide atmospheric cooling rates. Although the measured profiles are only accurate over a depth of half a scale height, about 6 km, we can obtain an order of magnitude value of fluxes.

Figures 27 and 28 are two graphs of the Planck function at 15 microns for two different surface temperatures and for two observed and theoretical profiles. The curves were approximated to straight lines in order to apply the following theory and to find the variation of heat flux with pressure.

From Schwartzchild's equation we have

$$\frac{\partial F_+}{\partial \tau} = -F_+(\nu) + b \qquad \text{and} \qquad \frac{\partial F_-}{\partial \tau} = F_-(\nu) - b$$

where $\tau(z)$ is the optical depth at height z, b is the Planck function at a given temperature. τ^* is the total optical depth of the atmosphere and b_g is the Planck function at the ground. For radiative equilibrium we have:

$$\frac{\partial (F_+ - F_-)}{\partial \tau} = 0$$

i.e. there is no change of the net flux with optical depth or height.

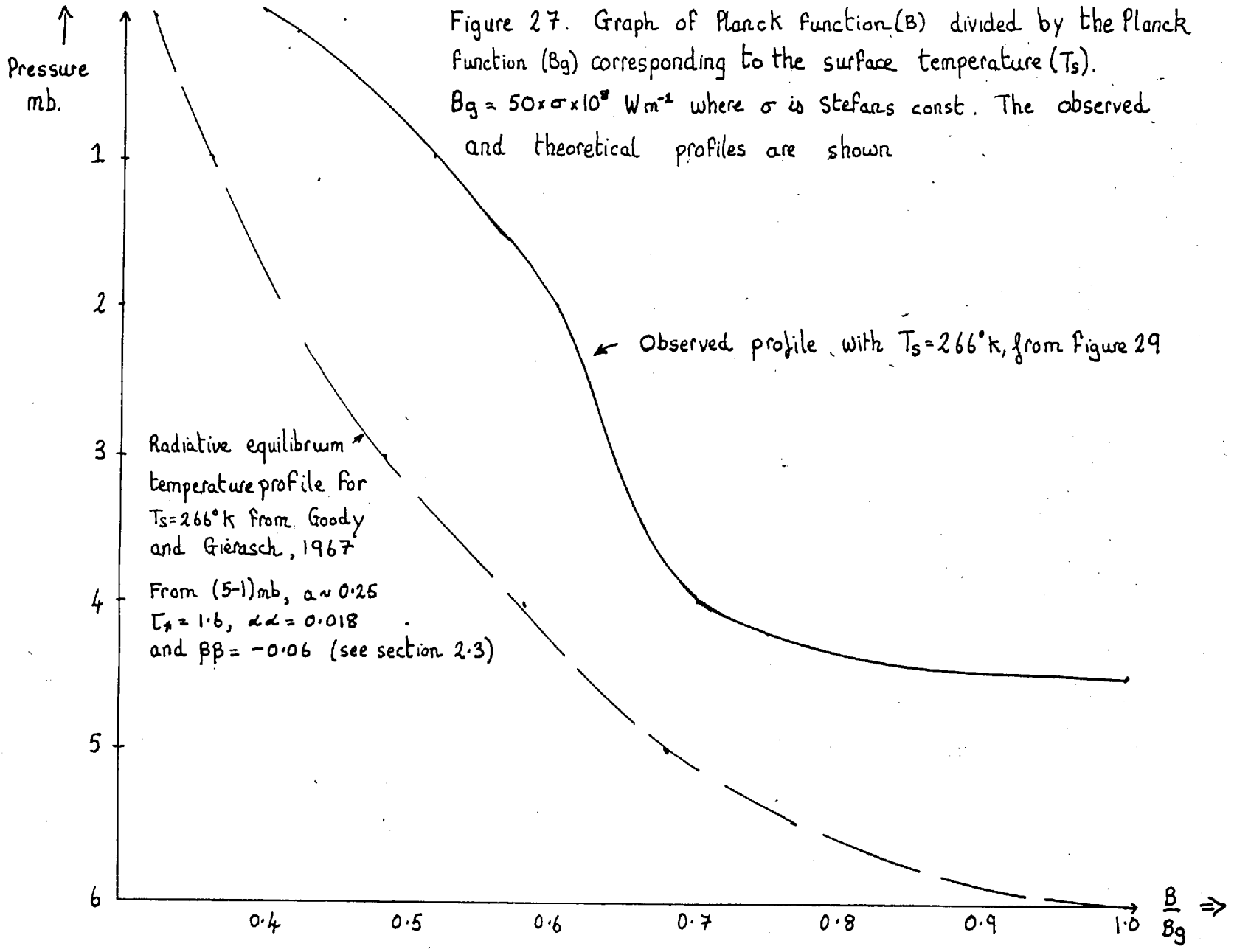

Figure 27. Graph of Planck function (B) divided by the Planck function (B_g) corresponding to the surface temperature (T_s). $B_g = 50 \times \sigma \times 10^8$ $W m^{-2}$ where σ is Stefans const. The observed and theoretical profiles are shown

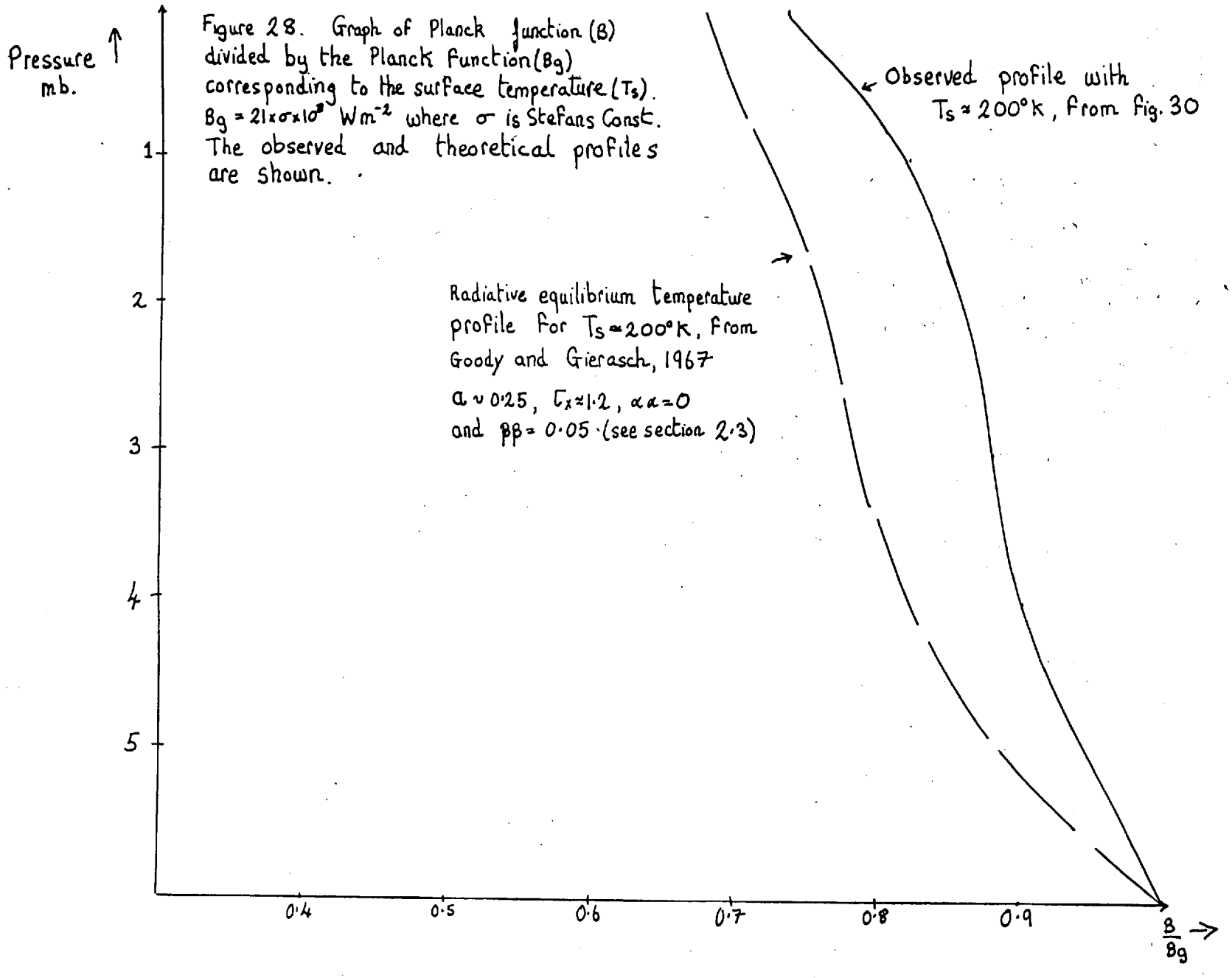

Figure 28. Graph of Planck function (B) divided by the Planck function (B_g) corresponding to the surface temperature (T_s). $B_g = 21 \times \sigma \times 10^8$ $W m^{-2}$ where σ is Stefans Const. The observed and theoretical profiles are shown.

At the top of the atmosphere we define $\tau = \tau^*$ and the downward longwave flux from infinity, F_- , to be zero. This assumes there is no absorption of solar radiation, differing from the theoretical radiative profile assumptions. At the ground, where the optical depth is zero, we assume the upward flux of radiation, F_+ , is equal to the Planck function at the ground temperature b_g . From the three equations and the two boundary conditions, we obtain:

$$b(\text{equilibrium}) = \frac{(1 + \tau^* - \tau)}{2 + \tau^*} \cdot b_g \qquad (2.1)$$

So far we have only applied Emden's method to this grey atmosphere radiation problem. Assuming $\partial\tau = \rho k \partial z$, where k is the absorption coefficient per unit mass of the gas per unit area for a grey atmosphere, ρ is the density, and assuming that the mixing ratio of carbon dioxide is constant, then the optical depth is a linear function of p, such that, say, $\tau = a(p_s - p)$ where p_s is the surface pressure and 'a' is a constant. The equation 2.1 is modified to:

$$b(\text{equilibrium}) = \frac{(1 + ap)}{2 + ap_s} \cdot b_g$$

As a first approximation for obtaining heat fluxes from Figures 27 and 28, we assume that the Planck function varies linearly with pressure, i.e.

$$b/b_g = \alpha + \beta\tau$$

Putting $b = b(\text{equilibrium})(1 + \alpha\alpha + \beta\beta\tau)$ we find that

$$\frac{1}{b_g}\frac{\partial}{\partial\tau}(F_+ - F_-) = (\alpha\alpha - \beta\beta)e^{-\tau} + (\alpha\alpha + \beta\beta + \beta\beta\tau^*)\, e^{(\tau - \tau^*)} \qquad (2.2)$$

Although Goody's radiative equilibrium temperatures are based on carbon dioxide with an atmospheric surface pressure of 4.9 mb, since there is probably about 30% of argon in the atmosphere which will have little effect on the radiative equilibrium profiles, then we find that the total

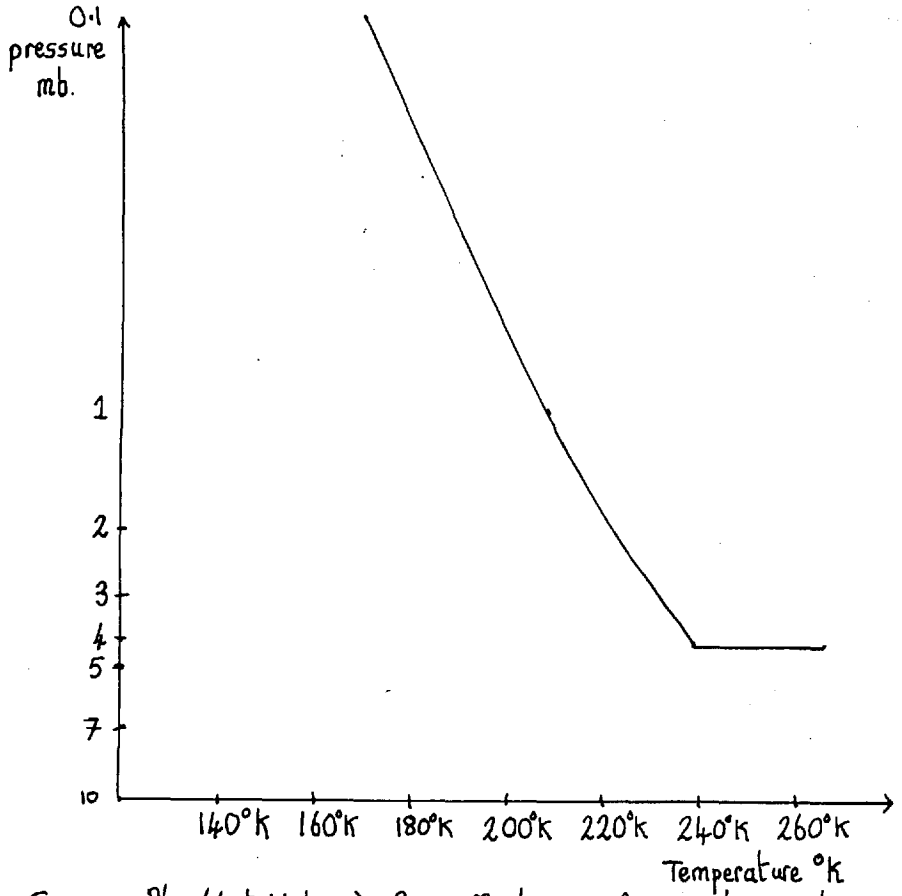

Spacecraft; (Lat, W. Long); Rev.; Martian time; Average lapse rate in bottom scale ht.
6966539 ; (-20·7, 137·8); 150; 14·7 hrs; 2·2° K km^{-1}

Figure 29

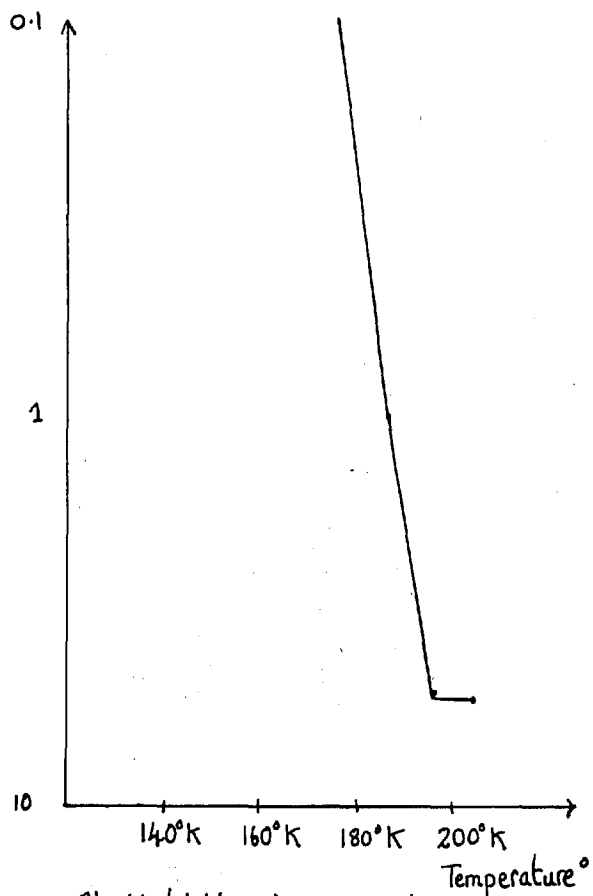

Spacecraft; (Lat, W. Long); Rev.; Martian time; Avge. lapse rate
8515173 ; (47·2, 95·6); 193; 16·0 hrs; 0·6° K km^{-1}

Figure 30

Graphs of temperature against pressure, taken from Mariner 9 data.

atmospheric pressure at the surface is about 6.3 mb; very close to the observed mean of 6.1 mb. Sagan (1968) argues that the surface temperatures of the mountains are constant since there is very little greenhouse effect due to the small optical depth of the atmosphere. The gradients of the large scale mountain slopes are generally less than 5 degrees so there is little surface illumination variation and there is little heat exchange with the air if earth type diffusivities are used, mainly because of the small surface atmospheric density. This theory also assumes that there is little spatial albedo variation of the surface. The above discussion is used to justify the comparisons of the measured and theoretical temperature profiles used in Figure 27 for different surface atmospheric pressures.

The optical depths obtained from the two Goody radiative equilibrium profiles on Figures 28 and 27 are 1.2 and 1.6 for the curves with $T_s = 200^{\circ}K$ and $266^{\circ}K$. Despite the disagreement in the optical depth calculations, we do not think this invalidates the order of magnitude calculation of fluxes. Figures 28 and 27 give the values for the constants $\alpha\alpha$ and $\beta\beta$, from which the cooling rates can be calculated.

For example for $T_s = 200^{\circ}K$, equation 2.2 becomes:

$$\frac{\partial (F_+ - F_-)}{\partial \tau} = -0.05\left(e^{-\tau} - 2.2\, e^{(\tau - 1.2)}\right)$$

We can calculate the atmospheric cooling rates using the equation

$$\frac{dT}{dt} = \frac{g}{C_p}\frac{\partial (F_+ - F_-)}{\partial p}$$

where $(F_+ - F_-)$ is the net longwave flux, with pressure p, where T is the temperature in degrees Kelvin and t is time. For the 5 mb pressure level ($\sim$ 2 km) the cooling rate is about $40^{\circ}K$/day and at 4 mb about $150^{\circ}K$/day. These figures are only accurate to about an order of magnitude because of the approximations used. The cooling rates will not be measurable since within a short length of time the mean state temperature profiles would be modified. The earth's tropospheric radiative cooling rate is about $1^{\circ}K$ per day and the above

figures do agree with Goody and Belton (1967) who argue that the radiative relaxation times (or the time for a temperature perturbation to be reduced by e^{-1}) are approximately 30-100 times faster on Mars.

Above 13 km (3 mb) for Figure 28 there is still a reasonably large difference between the Planck function profiles. We think that in the first scale height the difference in temperature profiles can partly be explained by dynamical processes, as given in later chapters. Above two millibars the temperature anomalies are possibly due to infra-red absorption, or more likely solar heating. The Goody and Gierasch (1967) model possibly does not explain solar absorption accurately. In Gierasch and Goody (1972) it is shown that by introducing dust and thus increasing the solar absorption by the atmosphere, the observed profiles can be reproduced. Although no theoretical arguments are included in this report for dust concentrations observed by Mariner 9 during the storm, the theoretical temperature profiles are within a few degrees Celsius of the observed values. However, the authors do not justify the assumption that over 10% of the solar radiation is normally absorbed by the atmosphere: this amount being required to produce the temperature profiles observed by Mariner 9 well after the dust storm.

Figure 27, the Planck functions of the observed and theoretical summer profiles, is more difficult to interpret since the topography is about four kilometres high. However with such a large surface to air temperature discontinuity, vertical convection, which we have not discussed in this thesis, is probably responsible for the upward transfer of heat.

Generally the radiative equilibrium temperatures are too low and the lapse rates in the lowest 20 km too high when we compare them with the measured profiles. Even though the Mariner temperatures are only a mean over half a density scale height, the differences between the radiative and the observed profiles are too large to be experimental errors. In the following chapters, we will consider baroclinic eddies, long waves and some of their possible contributions to these different temperature profiles.

CHAPTER 3: BAROCLINIC EDDIES: A THEORETICAL BACKGROUND

3.0 Introduction

In this chapter we shall discuss one of the dynamical processes in the Martian atmosphere that could affect the radiative equilibrium temperature profiles mentioned in the previous chapter. In the winter hemisphere baroclinic eddies transfer large poleward heat fluxes, Mariner 9 photographs, Figs. 31, 32, 33, 34, 35, indicate wavelike patterns which are observed in the clouds at approximately 50^{o} latitude in the winter hemisphere. Figure 33 is generally believed (Leovy and Briggs, 1974) to show cloud associated with a cold front, although it is difficult to be certain since this, and all the photographs in this chapter, have been contrast enhanced. However, since the probable cloud band in Figure 33 is observable on the raw photographs, this feature is not purely a figment of the enhancement. All the figures 31-35 suggest that wavenumber four is observable and photographs 32,33 and 34,35 indicate a phase speed of about 10 ms^{-1}. In the next few chapters we investigate the theory of baroclinic waves, as a possible description of such motion. We will discuss in this chapter the theory of small amplitude waves, with the following two chapters containing the results.

3.1 Small amplitude waves on a Beta plane

For a frictionless fluid with a small Rossby number and with a large positive Richardson number, the quasi-geostrophic vorticity equation is appropriate (Green, 1960).

$$\frac{D}{Dt_h}(\xi_z) + v\beta = \frac{f}{\rho}\frac{\partial}{\partial z}(\rho w) \qquad (3.0)$$

where $\frac{D}{Dt_h}$ is the horizontal derivative following the motion, ξ_z is the vertical component of relative vorticity, w is the vertical velocity, f the Coriolis parameter, β the equator to pole differential of the Coriolis parameter and z is the vertical height co-ordinate.

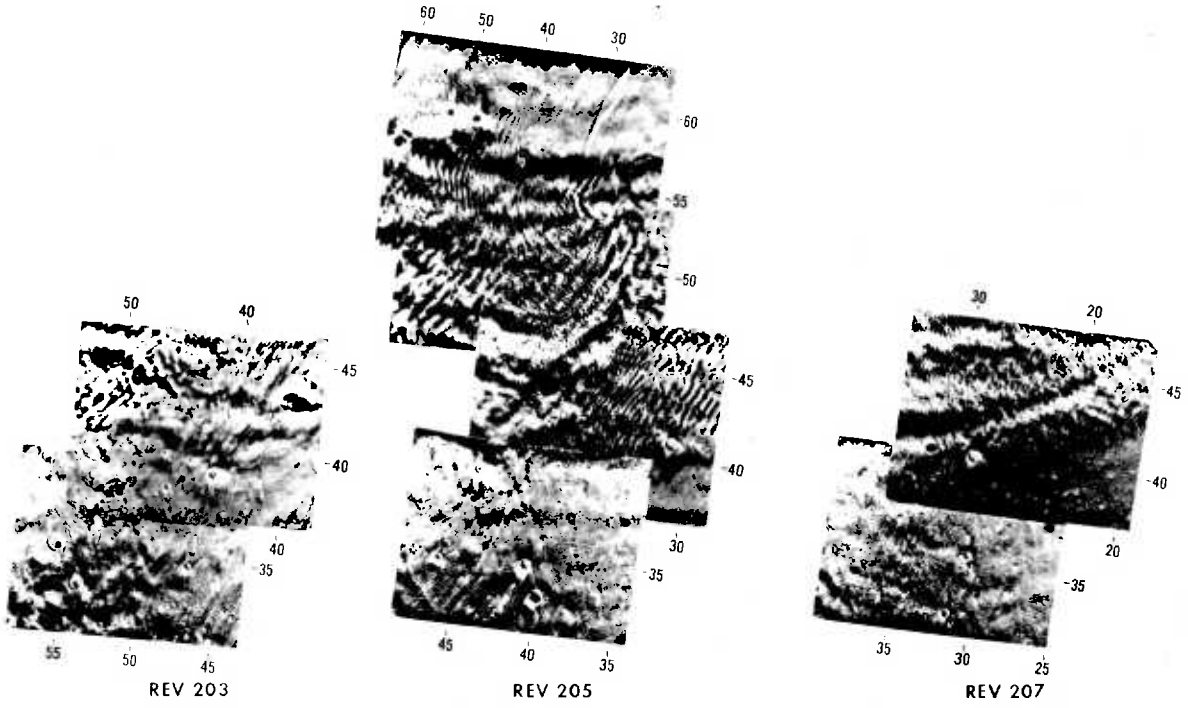

Figure 31(a): The progress of a cold front across the Martian surface for revolution 203, 205 and 207. The photographs were taken at 24 hour intervals by Mariner 9.

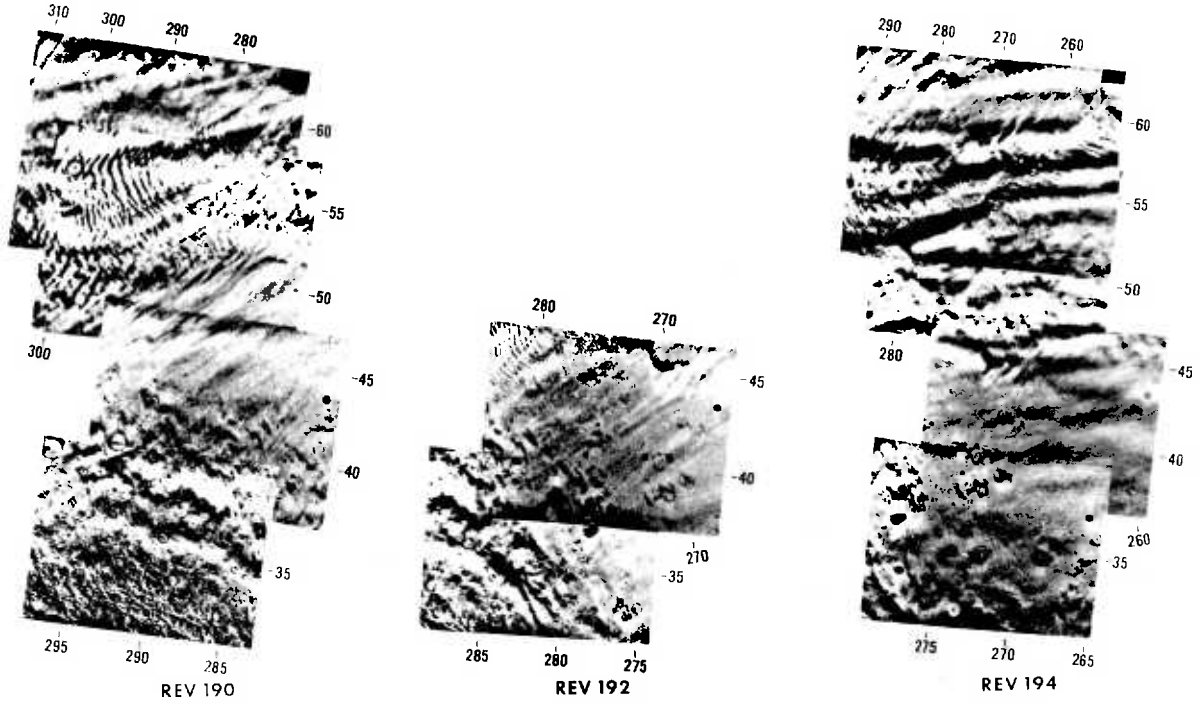

Figure 31(b): Another example of a baroclinic eddy for revolutions 190, 192, and 194. The photographs were taken at 24 hour intervals for Mariner 9.

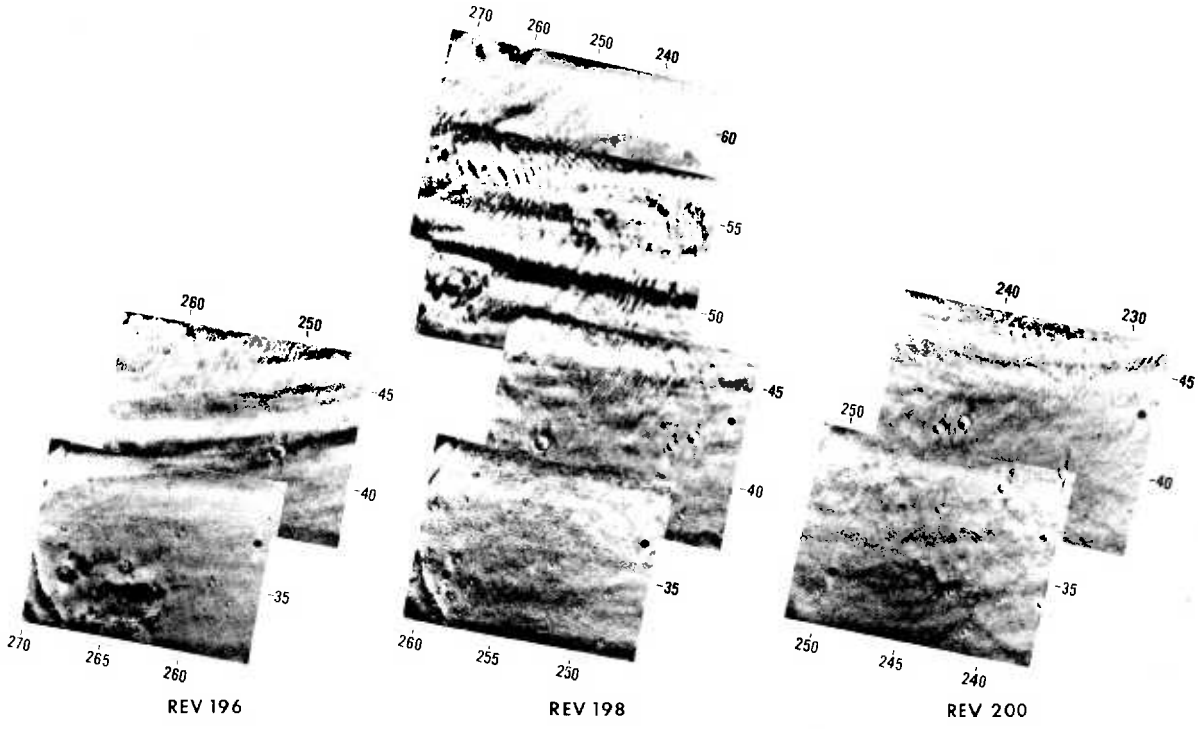

Figure 31(c): A further series of photographs of a baroclinic eddy for revolutions 196, 198 and 200.

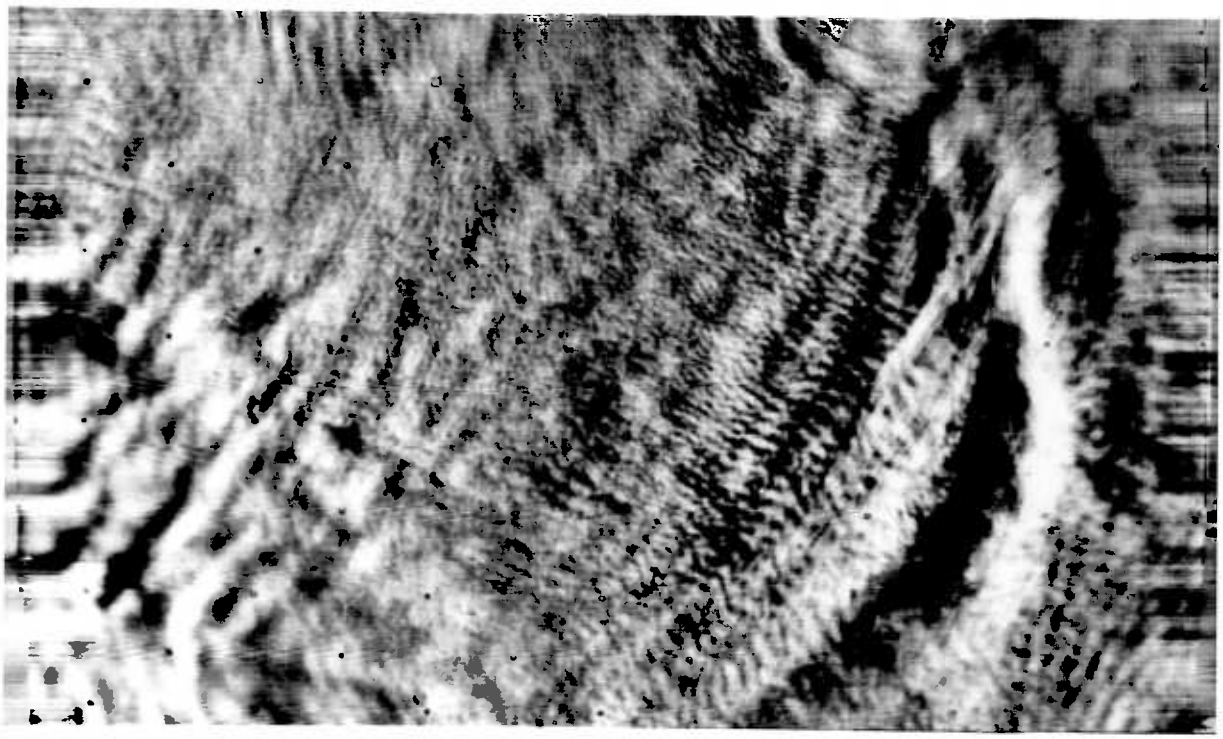

Figure 32(a): A photograph of a cold front on Mars.

	Latitude	Longitude
Centre	53.0°	39.8°
L.L.	47.4°	52.3°
L.R.	45.7°	30.4°

Rev. 205
D.A.S. 8947164
Viewing angle ∿ 17.3°
Lighting angle ∿ 75.2°
Martian local time ∿ 15.9 hrs
North angle ∿ 264.5°
Subsolar latitude ∿ -4.15°
Sun angle ∿ 174°

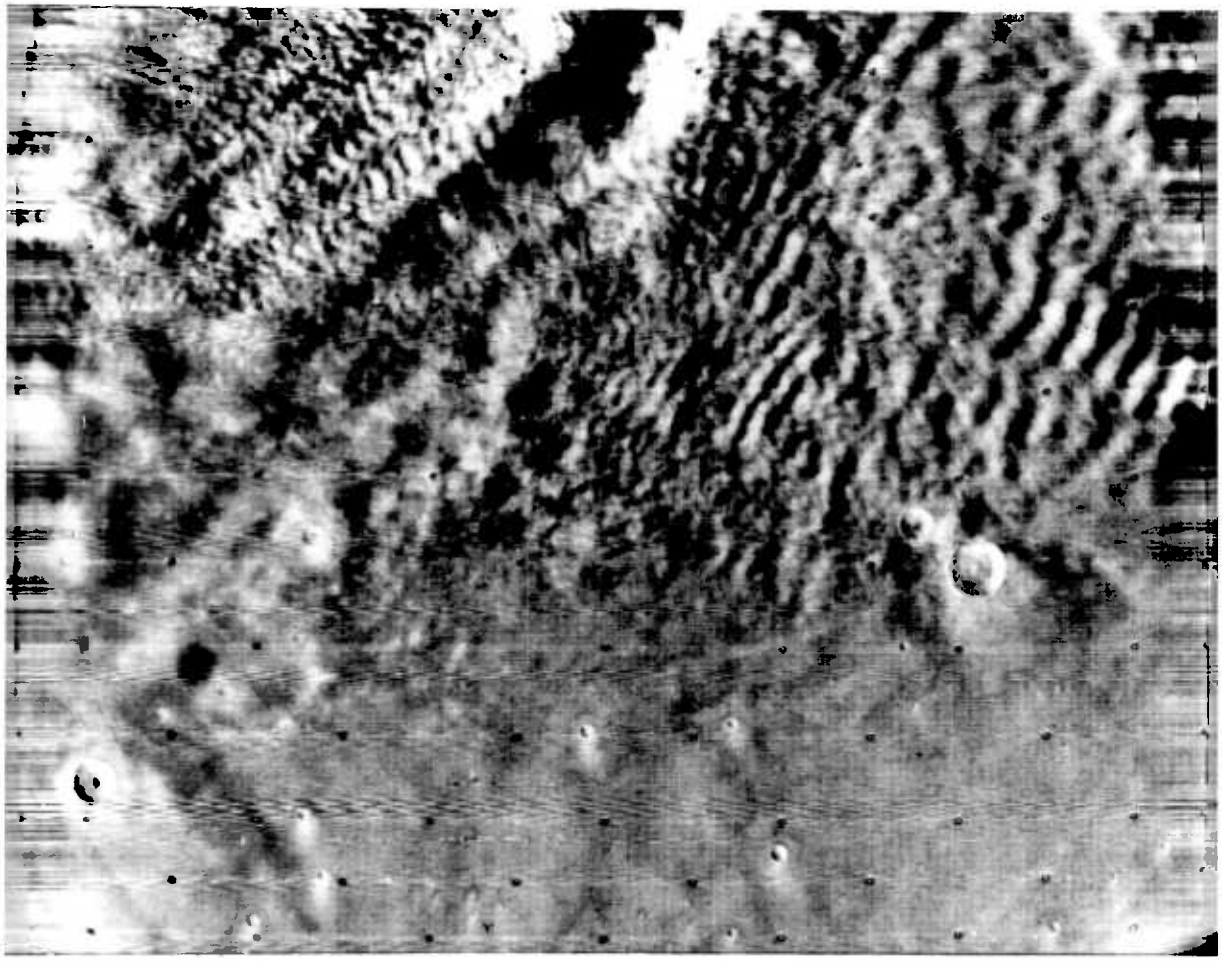

Figure 32(b): A photograph of the same cold front as on Figure 32(a).

	Latitude	Longitude
U.L.	49.3°	45.1°
U.R.	47.1°	24.0°
L.L.	38.5°	45.4°
L.R.	36.6°	28.2°

Rev. 205
D.A.S. 8946954
Viewing angle ∿ 8.5°
Lighting angle ∿ 72.7°
Martian local time ∿ 16.1°
North angle ∿ 260.8°
Subsolar latitude ∿ -4.15°
Sun angle ∿ 148°

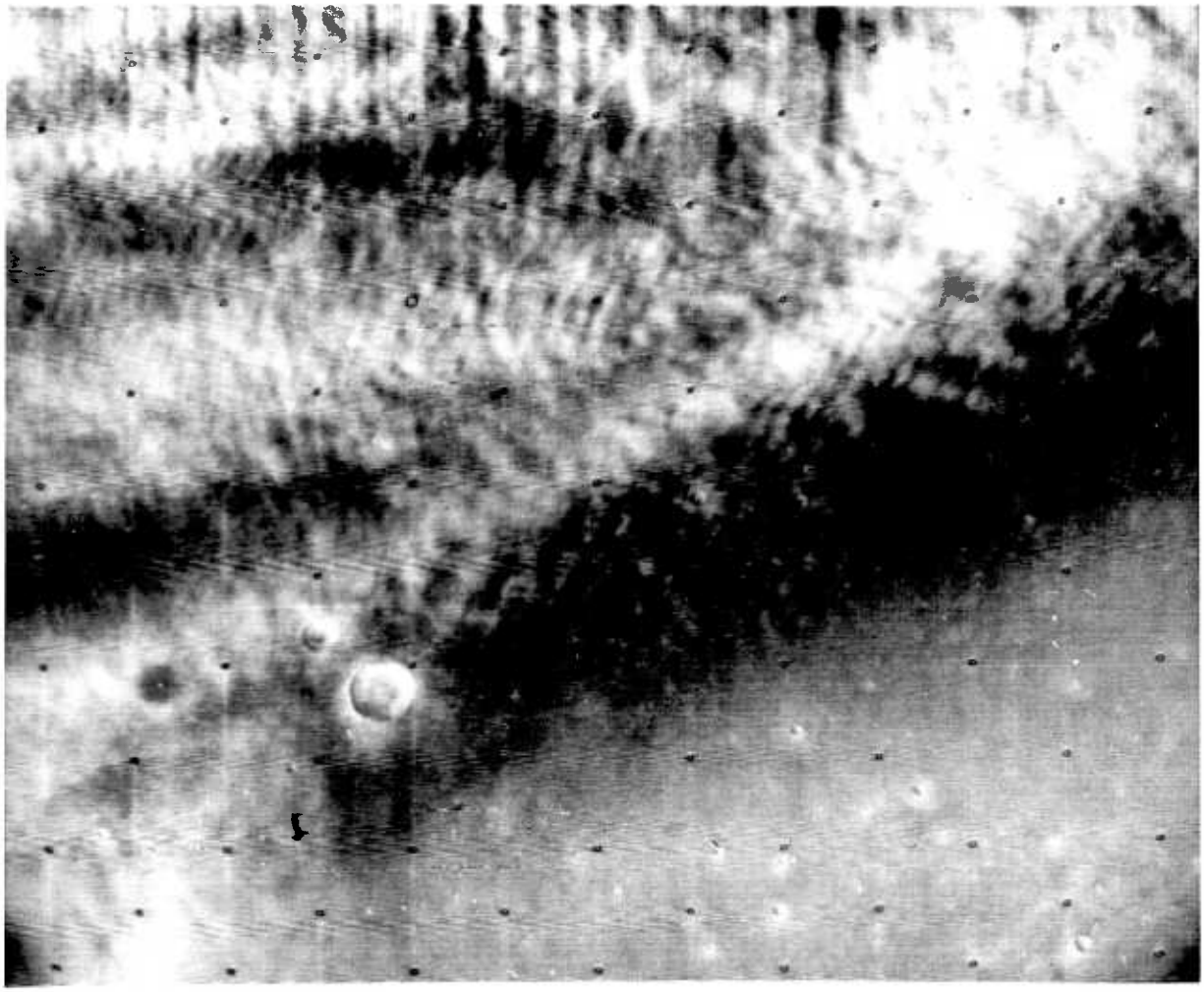

Figure 33: A photograph of the cold front on Figures 32, 24 hrs later

	Latitude	Longitude
U.L.	49.4°	35.7°
U.R.	47.3°	14.6°
L.L.	38.7°	36.0°
L.R.	36.8°	18.8°

Rev. 207
D.A.S. 9018844
Viewing angle ∿ 9.6°
Lighting angle ∿ 72.1°
Martian local time ∿ 16.05 hrs
North angle ∿ 260.9°
Subsolar latitude ∿ -3.9°
Sun angle ∿ 147°

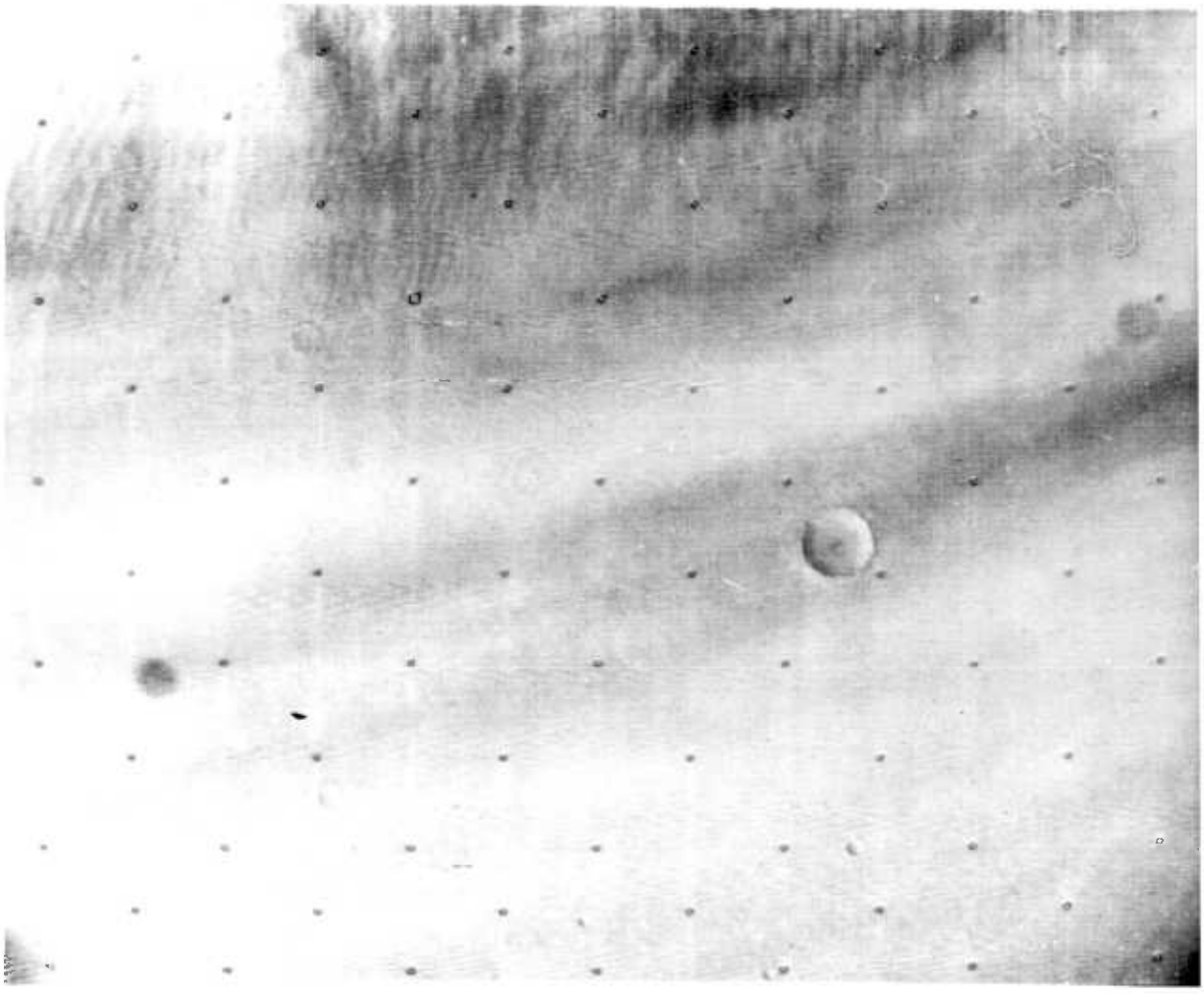

Figure 34: A photograph of a possible cold front

	Latitude	Longitude
U.L.	49.6°	265.9°
U.R.	47.0°	245.0°
L.L.	38.8°	266.7°
L.R.	36.6°	249.6°

Rev. 196
D.A.S. 8623134
Viewing angle ∿ 9.3°
Lighting angle ∿ 75.4°
Martian local time ∿ 16.3 hrs
North angle ∿ 259.2°
Subsolar latitude ∿ -5.1°
Sun angle ∿ 148°

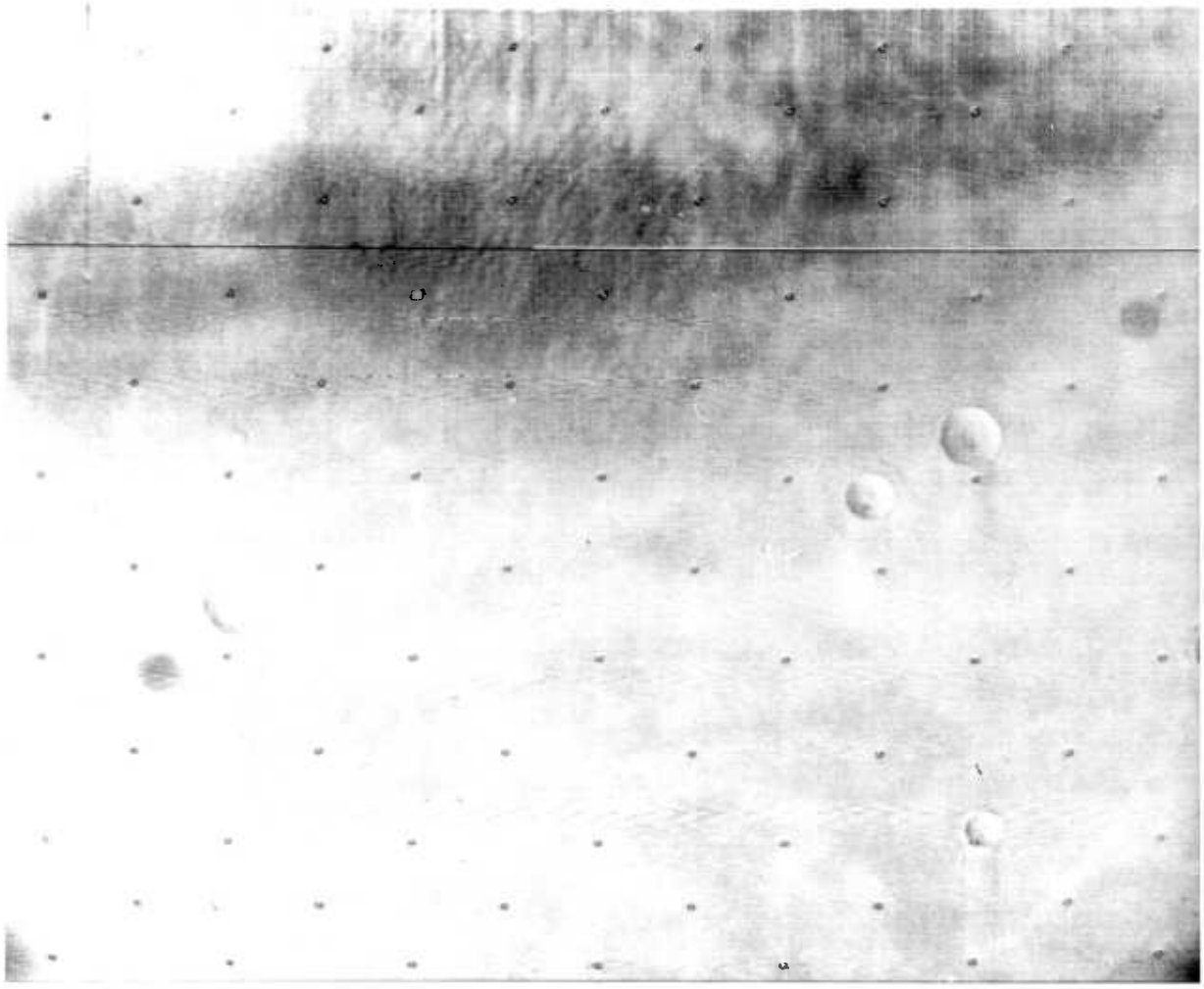

Figure 35: A photograph of the cold front on Figure 34, 24 hours later

	Latitude	Longitude
U.L.	49.0°	257.0°
U.R.	46.6°	236.0°
L.L.	38.2°	257.6°
L.R.	36.0°	240.3°

Rev. 198
D.A.S. 08695164
Viewing angle ∿ 6.7°
Lighting angle ∿ 74.8°
Martian local time ∿ 16.26 hrs
North angle ∿ 260.13°
Subsolar latitude ∿ -4.9°
Sun angle ∿ 148°

With a value of B, static stability of $1\text{-}2\times10^{5}\ m^{-1}$, the value of the Richardson number, $g\beta(\partial u/\partial z)^{-2}$, for a wind shear of 5 $ms^{-1}\ km^{-1}$ is 1.5-3, with a Rossby number of about 0.4. These numbers are near the limit at which this theory might be expected to hold, but we will assume the approximations are valid.

From the thermodynamic equation, we have

$$\frac{D}{Dt_h}(\delta\phi) + w\beta = -\alpha\delta\phi \qquad (3.1)$$

where α is the inverse of the radiative damping time constant, ϕ is the entropy divided by the specific heat at constant pressure, θ is the potential temperature as defined in Chapter 2, equation 2.0. The entropy is approximated by assuming:

$$\phi(x,y,z,t) = \phi_0(z) + \delta\phi(x,y,z,t) \qquad \text{and where}$$

$$\ln\theta = \frac{1}{\gamma}\ln p - \ln\rho \qquad (3.2)$$

with γ being the ratio of the specific heat at constant pressure to the specific heat at constant volume. We also have $\delta\phi = \delta\theta/\theta$

Normally the thermodynamic equation (3.1) is used without the damping term, which, in the equation represents Newtonian radiative cooling. The heat loss towards the mean state $\phi_0(z)$ is proportional to $C_p(T - \bar{T}^{x}_{(y,z)})$ which approximately equals $C_p(\theta(p/p_0)^{R/c_p} - \bar{\theta}^{x}(p/p_0)^{R/c_p}) \approx C_p\delta\phi$ where $\delta\theta = \theta(x,z,t) - \bar{\theta}^{x}(z,t)$ and $\delta T = T(x,y,z) - \bar{T}^{x}(y,z)$. Thus in the thermodynamic equation (3.1) we deduce that the radiative cooling is proportional to $\alpha\delta\phi$, where the values of α correspond to those given in Goody and Belton (1967).

We can use the stream function $u = -\frac{\partial\psi}{\partial y}$ and $v = \frac{\partial\psi}{\partial x}$ with $\psi = \psi' - uy$. From equation (3.2) we have $\delta\phi \propto H\frac{\partial\psi}{\partial z} - H\beta\psi \overset{x}{\approx} H\frac{\partial\psi}{\partial z}$ and also the sufficient condition that $\delta\phi = \frac{F}{g}\frac{\partial\psi}{\partial z}$. The assumption that $\beta\psi \ll \partial\psi/\partial z$ is not certain since this implies that the scale depth H of the motion is much less than 50 km. This approximation is probably satisfactory,

however, since I will show that the dynamical scale depth is approximately 10-20 kilometres. White (1976) shows that the inclusion of the ψ term only introduces itself in the boundary conditions where its effect on the Martian atmosphere is not very large. Thus we can assume that this approximation is accurate.

In the thermodynamic equation (3.1) we assume that the Newtonian damping $\alpha\,\delta\phi$ is replaced by $\alpha \frac{f}{g}\frac{\partial \psi'}{\partial z}$. The cooling is proportional to the gradient of the perturbation of the stream function ψ', thus not including the mean state term $-uy$. Writing down the perturbation equation for ψ', produced from the potential vorticity equation, we have:

$$\frac{D}{Dt_h}\left\{ \nabla^2\psi' + \beta y - \frac{\partial^2 u}{\partial y^2} + \frac{f^2}{gB}\frac{\partial^2 \psi'}{\partial z^2} - \frac{f^2}{gB}\frac{\partial^2 u}{\partial z^2}\, y - \frac{f^2}{gB}\left(\frac{1}{He} + \frac{1}{B}\frac{dB}{dz}\right)\frac{\partial \psi'}{\partial z} + \frac{f^2}{gB}\left(\frac{1}{He} + \frac{1}{B}\frac{dB}{dz}\right) y \frac{du}{\partial z} \right\}$$

$$+ \alpha \frac{f^2}{gB}\frac{\partial^2 \psi'}{\partial z^2} - \frac{\alpha f^2}{gB}\left(\frac{1}{He} + \frac{1}{B}\frac{dB}{dz}\right)\frac{\partial \psi'}{\partial z} = 0$$

We use the substitution $\psi' = \mathrm{Re}\,(F(z) \exp i\lambda(x-ct) \sin \mu y)$ where He is the density scale height and where $c = c_r + ic_i$ with c_r being the phase speed and λc_i being the exponential growth rate. Assuming that $\lambda^2 \gg \mu^2$ where λ and μ are zonal and meridional wavenumbers, and neglecting the y variation of the mean flow we obtain the linearised form:

$$(u-c)\left\{ F'' - \left(\frac{1}{He} + \frac{1}{B}\frac{dB}{dz}\right) F' - \frac{\lambda^2}{f^2} gB F \right\} + \left\{ \frac{gB\beta}{f^2} - \frac{\partial^2 u}{\partial z^2} + \frac{\partial u}{\partial z}\left(\frac{1}{He} + \frac{1}{B}\frac{dB}{dz}\right) \right\} F$$

$$+ \frac{\alpha}{i\lambda}\left\{ F'' - F'\left(\frac{1}{He} + \frac{1}{B}\frac{dB}{dz}\right) \right\} = 0 \qquad (3.3)$$

If we have constant shear, no vertical variation of density and static stability and no Beta effect we have

$$\left(u - c - \frac{i\alpha}{\lambda}\right) F'' - (u-c)\frac{\lambda^2 gB}{f^2} F = 0 \qquad (3.4)$$

For numerical solutions equation (3.3) is used with constant shear, since the windfields are not accurately known.

The boundary condition of w = 0 can be transformed using the thermodynamic equation which gives

$$(u-c)F' - u' + \frac{\alpha}{i\lambda}F' = 0$$

The rigid boundary is appropriate at the ground but is also used as the upper boundary condition in the Green type model. An alternative upper boundary condition is $F \to 0$ as $z \to \infty$ (Kuo, 1952). Demanding the finiteness of ρF^2, or energy, we can argue that when z becomes large F^2 or F must vary as a negative exponential in z in its upper limit. Newtonian radiational cooling, as envisaged on Mars, could provide the necessary damping of the wave and this boundary condition has been used to check the rigid lid w = 0.

3.2 Computation

Three point centred finite differences are used to calculate the differentials, i.e.

$$F''(N) = \frac{F(N+1) + F(N-1) - 2F(N)}{h^2} \quad \text{and} \quad F'(N) = \frac{F(N+1) - F(N-1)}{2h}$$

where F(N) is the value of the function F at the N^{th} level in the vertical. The truncation error of the first derivative is $\frac{1}{6}h^2F'''(N)$ and for the second derivative the error is $\frac{1}{12}h^2F^{iv}(N)$. Hence doubling h the steplength will increase the finite differencing errors by a factor of four. Thus we are able to obtain the equation

$$(YR + YI)\underset{\sim}{F} - cW\underset{\sim}{F} = 0 \qquad (3.5)$$

where W, YI, YR are matrices, YR and YI are the real and imaginary coefficients of the eigenvector $\underset{\sim}{F} = (F_1, \ldots, F_N)$ and where c is the complex eigenvalue which is to be calculated.

The method used to solve this equation is an I.B.M. library subroutine which involves using the Q.R. algorithm developed by Francis and found in Wilkinson (1965). There is little point in trying to give the theory behind these routines, but, basically, the matrix $W^{-1}(YR+YI)$ is factorised into an upper triangular and unitary matrix, with the eigenvalues being produced as diagonal elements of this factorised matrix. The inclusion of the radiational damping ($\alpha \neq 0$) necessitates the use of the matrix YI. This produces storage limitations, restricting the size of the matrices and hence the number of levels in the vertical. Values for the phase speed c_r and the growth rate λc_i are obtained for certain wavenumbers. The largest growth rate, λc_i, for each wavenumber is determined and the corresponding eigenfunction calculated. From the results it is found that there is at most one eigenvalue with a positive growth rate, with the others negative if there is a radiative cooling term. This is not obvious and I assume it is a consequence of the differential equation. If there is no Newtonian cooling there are two eiganvalues with non-zero growth-rates: one is positive, the other negative. Unfortunately solving the equation (3.5) only gives the eigenvalue; the eigenfunction has the correct shape but the magnitude is arbitrary. This corresponds to multiplying the solution to (3.5) by a constant which would change the eigenfunction but not the eigenvalue.

These are the main points arising from the theory and the computer program. In the next section we shall discuss the accuracy of the model and how it was tested for earth type conditions, before finally giving the results using Martian parameters.

CHAPTER 4: ACCURACY ANALYSIS OF THE COMPUTATION AND THE EFFECT OF NEWTONIAN DAMPING

4.0 Introduction

In this chapter we discuss the accuracy of this numerical method. We find that the convergence of the solutions depends only a little on the complexity of the equation, whether density effects, vertical variation of static stability or the Beta effect are included. The results for earth type parameters are checked by comparison with the analytic solutions for the Eady model, and with Green (1960) when we include Beta and density effects. The chapter concludes with an analysis of the effects of Newtonian radiative damping.

4.1 Comparison with analytic solutions for the Eady model

This comparison with analytic solutions can be done with the Eady model where the vertical velocity, w, is zero at ground and at the top of the fluid at 10 km. Neglecting the Beta effect and density stratification, with constant static stability of $1.8\times10^{-5}\ m^{-1}$ and no radiative damping, we have the results as given in Table 41.

From these results the accuracy of the five level and ten level models are about 6% and 1% respectively. There is little change in accuracy as we increase the wavenumber, although Kane (1973) suggests that for a given accuracy in this type of problem there is a direct relation between the wavenumber and the number of levels in the vertical. For wavenumbers 2-5 the analytic solutions are approached from above, whereas for wavenumbers greater than five the growth rate is approached from below. Presumably there is a non-integer wavenumber where the numerical solution is exact for a small number of levels. It is not possible to extend these accuracy results to the solutions with the density stratification, the Beta effect and variable static stability since the differential equation is modified and since the steering level no longer remains in the middle of the fluid.

TABLE 41

No. of levels	Horizontal Wavenumber			
	2	3	4	5
5	17.14	23.43	27.04	26.84
10	16.39	22.48	26.09	26.23
20	16.24	22.28	25.89	26.10
30	16.21	22.25	25.86	26.08
50	16.20	22.24	25.84	26.07
Analytic solutions	16.19	22.24	25.83	26.07

Table of growth rates multiplied by the radius of the earth (units of ms^{-1}) i.e. the imaginary part of the eigenvalue c multiplied by the horizontal wavenumber for different numbers of levels in the vertical and different horizontal wavenumbers. The analytic solutions are compared with the computational results. All the phase speeds are calculated at 15 ms^{-1} for a wind shear of 3 $ms^{-1}\,km^{-1}$ static stability of $1.8\times10^{-5}\,m^{-1}$ with the other parameters having values typical for the earth.

TABLE 42

No. of levels	Horizontal Wavenumber				
	2	3	4	5	6
10	14.1 *6.1*	22.1 *11.9*	16.9 *11.7*	14.3 *10.2*	11.5 *9.2*
20	14.2 *6.9*	21.8 *12.4*	16.6 *12.2*	13.0 *10.6*	10.9 *9.3*
40	14.3 *7.3*	21.7 *12.7*	16.5 *12.4*	12.9 *10.8*	10.8 *9.4*

Values of growth rates ($\lambda\times c_i$) multiplied by the radius of Mars and values of phase speeds, c_r, in italics with typical values for Beta, the density scale height, a wind shear of 5 $ms^{-1}\,km^{-1}$, a static stability of $1.5\times10^{-5}\,m^{-1}$ and with an upper lid at 10 km for the Green model. All the results are in ms^{-1}.

4.2 Convergence of solutions when the density and Beta effects are included

Table 42 gives the corresponding growth rates and phase speeds for the Eady model on Mars, but includes the Beta effect and density stratification. From now onwards the Green model corresponds to the solutions to the differential equation with zero vertical velocity at the upper and lower boundaries. Although there are no analytic solutions with which we can compare the results from the 10, 20 and 40 level models, using the parameters in Green (1960) with a 40 level model the agreement is better than 5% As we increase the number of levels it can be seen from Table 42 that the growth rates converge marginally faster for small wavenumbers, thus agreeing with Kane (1973) whereas the phase speeds converge more rapidly for the shorter waves.

4.3 The effect of the vertical variation of the static stability

We can compare the convergence of the results obtained from Table 42 for a constant static stability, and those obtained for Table 43, for a vertically varying static stability. Both tables indicate reasonably good convergence. However we have not given a quantitative estimate of the convergence and Richardson's deferred approach to the limit is a method which can be used.

If we assume the errors are of the order of n^2, where n is the number of levels then we have

$$C_n = C + \epsilon/n^2 \qquad (4.0)$$

where c_n is the value of the solution using n levels, ϵ/n^2 is the error and c is the convergent solution. The finite difference truncations in the previous chapter give errors of $(h^2/12.0) \times F'''(z)$ and $(h^2/6.0) \times F^{IV}(z)$ for the first and second derivatives. Since the height of the lid divided by the number of levels n, is equal to h, the vertical step length, we have the basis for the use of this crude convergence test. For example, for wavenumber 3, Table 42, c in equation 4.0 has a value of 21.67 ms^{-1} for the growth rate

TABLE 43

No. of levels	Horizontal Wavenumber	
	3	3.5
10	9.05 *13.0*	7.8 *13.6*
20	9.10 *13.4*	7.95 *14.0*
40	9.15 *13.6*	8.0 *14.25*

Growth rates, multiplied by the radius of Mars, and phase speeds for different numbers of levels with typical Martian values for the density scale height and the Beta parameter, and with an upper lid at 10 km. for the Green model. The static stability B is equal to 10^{-5} (1+z/4 km) m^{-1}. All the results are in ms^{-1}. The phase speeds are in italics.

TABLE 44

No. of levels	Horizontal Wavenumber			
	3		4	
10	27.0 *15.7*	20.6 *15.8*	20.7 *13.2*	14.11 *16.6*
20	26.7 *16.0*	20.5 *16.2*	20.5 *15.5*	14.0 *16.9*
40	26.6 *16.2*	20.4 *16.3*	20.4 *15.6*	14.0 *17.0*
	$\alpha = 0$	$\alpha=(1\ \text{day})^{-1}$	$\alpha = 0$	$\alpha=(1\ \text{day})^{-1}$

Table of growth rates, multiplied by the radius of Mars and phase speeds for wavenumbers 3 and 4 for the Green model. A vertically constant static stability of $10^{-5}\ m^{-1}$ with the upper lid at 12 km, for typical Martian values of the density scale height and the Beta parameter, was used, both with no Newtonian damping (α=0) and with a damping time scale of 1 day. The units of phase speed and growth rates are in ms^{-1}. The phase speeds are in italics.

TABLE 45

No. of levels	Horizontal Wavenumber	
	3	3.5
10	6.51 *12.72*	5.65 *14.04*
20	6.54 *13.06*	5.80 *14.40*
40	6.56 *13.22*	5.90 *14.57*

Table of growth rates and phase speeds as in Table 43, but with a radiative Newtonian damping time scale of 1 day. The phase speeds are in italics.

TABLE 46

No. of levels	Horizontal Wavenumber			
	3	4	5	6
10	5.16 *15.3*	5.29 *13.2*	3.98 *11.5*	2.73 *10.0*
20	4.97 *15.7*	5.16 *13.6*	3.92 *11.8*	2.51 *10.4*
40	4.86 *16.0*	5.09 *13.8*	3.88 *11.98*	2.48 *10.5*
70	4.82 *16.1*	5.06 *13.8*	3.86 *12.0*	2.47 *10.6*

Table of growth rates multiplied by the radius of Mars, and phase speeds with an upper lid F=0 at 10 km including typical density scale height and Beta parameters, with a radiative damping time of one day and a static stability of $1.5\times10^{-5}\,m^{-1}$. All the results are in ms^{-1}. The phase speeds are in italics.

if both the 10 and 20 and 20 and 40 level results are used to eliminate ϵ Similarly for the corresponding phase speeds we have values of c of 12.57 ms^{-1} and 12.8 ms^{-1} using the 10/20 and 20/40 level results. Thus for wavenumber 3, the growth rate's error is proportional to n^{-2}, whereas the phase speeds, although convergent are not as accurate. The results from Table 43, with vertically variable static stability, can also be checked in this way and give very similar conclusions.

The vertical variation of static stability effectively increases the size of the coefficient of the first derivative of the function This coefficient is increased from 1/12 km, the inverse of the density scale height by adding the term $1/\beta \, d\beta/dz$ which has a value of about 1/4 km in the results given in Table 43. With the larger truncation error from the first derivative one might expect the error term $(c_n - c)$ to be larger, although still proportional to $1/n^2$. However convergence is as good as the constant vertical static stability models. Further details of the accuracy of these solutions would only be gained after further numerical analysis studies which are beyond the scope of this thesis.

4.4 Convergence of solutions with Newtonian damping

The inclusion of the Newtonian damping term does not affect the convergence of the numerical solutions. With a constant static stability the phase speeds and growth rates, as in Table 44, are modified but converge as rapidly as those solutions calculated with no damping. Similarly Table 45 gives the corresponding damped solutions to those results in Table 43 which have a vertically varying static stability. Again there is good convergence. Radiational damping is always used with the F=0 upper boundary condition and as mentioned in the following paragraph, the solutions converge as rapidly as with the Green model.

4.5 Accuracy and convergence of the model with F=0 as an upper lid

A similar analysis has been applied to the model with F=0 as an upper boundary condition. Since this model has not been used much and since the con-

vergence of solutions is much like the results from the Green model, an example only of the results is given below in Table 46. The varying static stability results, with $B=10^{-5}\times(1+z/4\ \text{km})$, although not tabulated give very similar good convergence.

In conclusion therefore we find that for both the Green model and the model with F=0 as the upper boundary, the solutions converge rapidly and the 20 level results are within at most 10% and probably 5% of the correct values. This is a conservative estimate from all the results and cannot be exact since we have no analytic solutions with which to compare.

In the following chapter we have considered mainly the solutions for the Green model with constant static stability. The Mariner 9 temperature profiles are not very accurate and thus although a static stability (B) given by $B=10^{-5}\times(1+z/4\ \text{km})$ may seem more appropriate from some of the mid-latitude winter profiles given in the appendix, we have only briefly considered these results.

4.6 Effect of radiation on the Eady wave

With no density and Beta terms in the differential equation 3.3 the phase speed of the wave is not affected by Newtonian damping. This is not an obvious result since the complex function F in equation 4.1 would be expected to lose its symmetry about the mid-level of the fluid, thus changing the eigenvalue c. From equation 3.4 we have:

$$(u-c-i\lambda')F'' - p^2(u-c)F = 0 \qquad (4.1)$$

where $\lambda'=\alpha/\lambda$ and $p^2=\lambda^2 gB/f^2 \sim 5\times10^{-9}$ for wavenumber 4. With the boundary conditions the vertical velocity, w=0 at u=0 and z=0 and w=0 at $u=u_T$ and z=H, from the thermodynamic equation 3.1 we have:

$$(u-c-i\lambda')F' - u'F = 0 \qquad (4.2)$$

A Taylor expansion about z=0 gives:

$$F(z) = F(0) + zF'(0) + z^2/2\,F''(0) + z^3/3!\,F'''(0) + z^4/4!\,F^{iv}(0) + \ldots\ldots$$

and about z=H

$$F(H-z) = F(H) - zF'(H) + z^2/2 F''(H) - z^3/3! F'''(H) + z^4/4! F^{iv}(H) + ...$$

From equations 4.1 and 4.2, from the Taylor's expansion and by differentiating 4.1 for higher orders of the function F we are able to show:

$$F(z) = F(0)\left(1 - \frac{zu'}{(c+i\lambda)} + \frac{z^2}{2}\frac{cp^2}{(c+i\lambda)} - \frac{z^3}{3!}\frac{u'p^2}{(c+i\lambda)} + \frac{z^4}{4!}\frac{(cp^2)^2}{(c+i\lambda)^2} + ...\right) \qquad (4.3)$$

and

$$F(H-z) = F(H)\left(1 - \frac{zu'}{(u_T-c-i\lambda)} + \frac{z^2(u_T-c)p^2}{2!(u_T-c-i\lambda)} - \frac{z^3p^2u'}{3!(u_T-c-i\lambda)} + \frac{z^4}{4!}\frac{((u_T-c)p^2)^2}{(u_T-c-i\lambda)} + ...\right) \qquad (4.4)$$

Differentiating the two above equations in order to find F'(z) and F'(H-z), we can substitute them in 4.5 which is correct at z=H/2.

$$\frac{F'(z)}{F(z)} = \frac{F'(H-z)}{F(H-z)} \qquad (4.5)$$

F(0) and F(H) can thus be eliminated. The term $p^2z^2/(n-2)(n-1)$ is the approximate multiplication factor between odd and even orders of F(z): hence the fifth order term in the Taylor expansion is about 10% of the third order term and the fourth order term is about 10% of the second order term. This Taylor expansion can be extended to give more accurate approximations with higher orders of F(z). However the answer will be the same as the third order approximation illustrated below. From 4.5 we have:

$$\frac{F(0)\left(-\frac{u'}{c+i\lambda} + \frac{zcp^2}{c+i\lambda} + \frac{z^2}{2!}\frac{u'p^2}{-(c+i\lambda)}\right)}{F(0)\left(1 + \frac{u'z}{-(c+i\lambda)} + \frac{z^2}{2!}\frac{cp^2}{(c+i\lambda)} - \frac{z^3}{3!}\frac{u'p^2}{(c+i\lambda)}\right)} = \frac{F(H)\left(-\frac{u'}{(u_T-c-i\lambda)} + \frac{z(u_T-c)p^2}{(u_T-c-i\lambda)} + \frac{z^2}{2!}\frac{p^2u'}{-(u_T-c-i\lambda)}\right)}{F(H)\left(1 - \frac{u'z}{(u_T-c-i\lambda)} + \frac{z^2}{2!}\frac{(u_T-c)p^2}{(u_T-c-i\lambda)} - \frac{z^3}{3!}\frac{p^2u'}{(u_T-c-i\lambda)}\right)}$$

Cross multiplying and ignoring terms of a higher power than three we have, from the real part of the equation

$$2u'C_r = u'U_T \quad \text{and so} \quad C_r = \frac{U_T}{2} \qquad \text{— (4.6)}$$

This result was verified, to an accuracy of one part in a million, on all the programs run with no Beta and density effects and with constant static stability.

Using equations (4.3) and (4.4), their two first differentials with respect to z and the condition (4.6), we can deduce that F(0) is equal to the complex conjugate of F(H), and as a consequence F(z) is a complex conjugate of F(H-z). Thus not only does the phase speed remain constant with radiational damping as defined in Chapter 3, but also the eigenfunction remains symmetrical.

4.7 General effects on the phase speed and growth rate by Newtonian damping

Pedlosky (1964) calculated the upper and lower limits on the phase speed and growth rates as given in the Green model. I have extended this theory to include Newtonian cooling in order to gain more insight into the phase speeds and growth rates of these eddies.

In equation (3.3) we substitute for F by $\phi_*(u-c-i\dot{\lambda})$. The upper and lower boundary condition of zero vertical velocity corresponds to

$$\frac{d\phi}{dz}=0.$$

Multiplying by $\phi^*\varrho/B$ in the differential equation and integrating between 0,H we obtain:

$$\int_0^H \left(-\frac{\varrho}{B}(u-c-i\dot{\lambda})^2\left|\frac{d\phi}{dz}\right|^2+\left(\frac{g\beta\beta}{f^2}-\rho^2(u-c)\right)|\phi|(u-c-i\dot{\lambda})\right)dz = 0 \qquad \text{— (4.7)}$$

where $\rho^2=\lambda^2 g\beta/f^2$ and ϕ^* is the complex conjugate of ϕ . The algebraic manipulations to deduce (4.7) are basically found in Pedlosky (1964). Considering the imaginary part of equation (4.7) we have

$$\int_0^H \left\{\left|\frac{d\phi}{dz}\right|^2\cdot\left(\frac{2\varrho}{B}(u-c_r)(c_i+\dot{\lambda})\right)+|\phi|^2\left(\rho^2(u-c_r)(c_i+\dot{\lambda})\right)\right.$$
$$\left.-|\phi|^2\cdot\frac{g\beta\beta}{f^2}(c_i+\dot{\lambda})+(u-c_r)c_i\rho^2|\phi|^2\right\}dz = 0 \qquad (4.8)$$

By putting $\lambda = 0$, $\rho/B = 1$ and $\beta = 0$ we are able to remove the effects of radiational damping, the effect of variable static stability and the density, and the variation of the Coriolis parameter with latitude.

More generally, if $C_r \geq \max(u)$, then the equation (4.8) cannot be satisfied providing $(c_i + \lambda)$ is positive. Without the Beta effect it is possible that the phase speed could equal max(u). There must also be one value of u such that

$$(u - c_r)\{p^2(c_i+\lambda) + c_i p^2\} \leq g\frac{B}{f^2}\beta\,(c_i+\lambda)$$

since $\left|\frac{d\phi}{dz}\right|$ cannot be zero everywhere. For a solution of the integral (4.8) this equation must be true if $u = u_{min}$ and thus

$$C_r \geq u_{min} - g\frac{B}{f^2}\beta\,\frac{(c_i+\lambda)}{(c_i+\lambda)p^2 + c_i p^2} \qquad - (4.9)$$

The inclusion of a non-zero radiation term λ has the effect of decreasing the size of the right hand side of equation (4.9).

A similar analysis can be used to find bounds on the growth rates. Substituting for F by $(u-c-i\lambda)^{\frac{1}{2}}\phi$ and for the boundary conditions corresponding to w = 0 we have $\frac{d}{dz}\left(\phi(u-c-i\lambda)^{-1/2}\right) = 0$

For the main integral we obtain:

$$\int_0^H -\frac{\rho}{B}\left|\frac{d\phi}{dz}\right|^2 + \left\{p^2(u-c) - g\frac{B}{f^2}\beta + \frac{(u')^2(u-c-i\lambda)^*}{4\,|u-c-i\lambda|^2}\right\}|\phi|^2\,dz = 0 \qquad (4.91)$$

From the imaginary part of (4.91) we have

$$\frac{(u')^2}{4}(c_i+\lambda) \geq c_i p^2 |u-c-i\lambda|^2$$

Since $|u-c-i\lambda|^2 \geq (c_i+\lambda)^2$ we have $\frac{(u')^2}{4} \geq c_i(c_i+\lambda)p^2$. Hence by increasing the damping term we can reduce the maximum value of the growth rate.

However if $|u-c_r| \geq |c_i+\lambda|$ which occurs at wavenumbers with small growth rates, except at the steering level, then we have:

$$\left\{ (u-c_r)^2 \rho^2 - \frac{(u')^2}{4} \right\} c_i \leq \lambda \frac{(u')^2}{4}$$

Thus for positive values of the coefficient c_i, which is generally true for large wavenumbers, then it is possible that the upper bound for the growth rate can be increased by supplying more radiative damping.

This and other points previously mentioned will be referred to in the results in the following chapter. The importance of radiation with long stationary waves is studied in Chapter 6, where its relative effect can be given by a non-dimensional number.

CHAPTER 5: RESULTS OBTAINED FROM THE BAROCLINIC EDDY MODEL

5.0 Introduction

This chapter summarizes the results from the model: first as applied to the earth to check that the program is working accurately and secondly using Martian parameters. First we shall consider the earth's atmosphere varying some important parameters such as the density scale height, the Beta parameter and the static stability, before discussing the atmosphere of Mars.

5.1 The effect of the density scale height and Beta parameter on the earth

The computer program solves the vorticity equation and thermodynamic equation, as given in Chapter 3. Using a 25 level Green model, we can compare on Graph 51 the growth rates for the earth's atmosphere with and without the density and Beta terms, with Green's (1960) results and the analytic solutions. These growth rate curves agree well with Green's solutions, indicating a decrease of wavelength of the fastest growing wave as we include the density and Beta terms. With no Beta or density effects, the stretching term $f\frac{dw}{dz}$ alone generates the vorticity and results in a growth rate curve with a single peak. The density and Beta effects are additional factors generating vorticity and this results in the increase in wavenumber of the most unstable wave and decreasing the height of the steering level.

5.2 Newtonian damping on the earth's baroclinic eddies

Graph 52 demonstrates the effect of ~~plausible~~ radiational damping times of 5 days and 30 days on the growth rate curve. The shape of the curves remains the same, although the longer the wavelength the greater the reduction in growth rate. The radiation damping time constant α, in equation (3.3), is divided by the wavenumber: this physically corresponding to a particle remaining longer in a large wavelength perturbation. 30 days

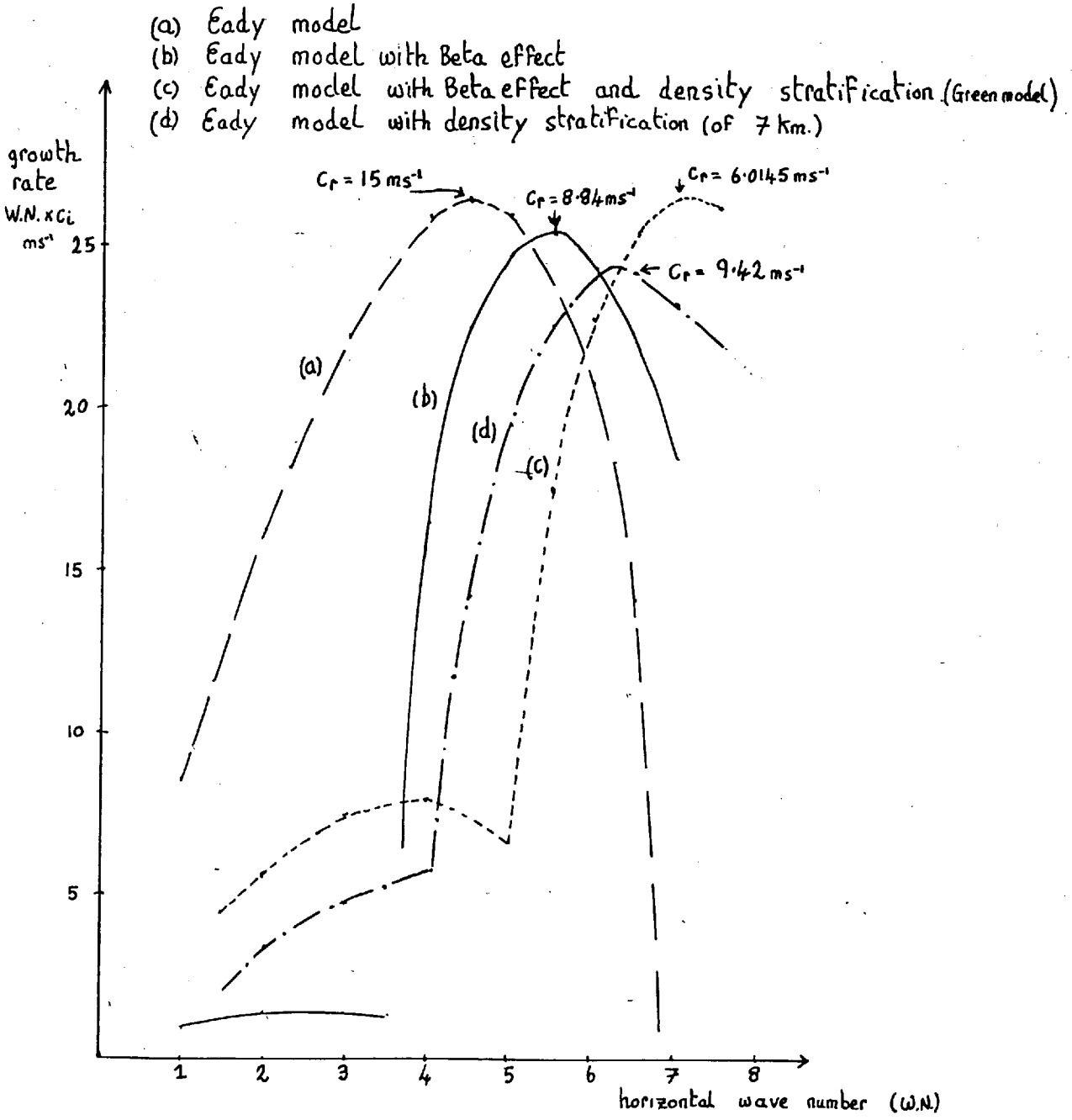

Figure 51. Graph of growth rate (W.N. x c_i) against horizontal wave number (W.N.) for a 25 level model, with an upper lid at 10 km. and with the phase speed of the most unstable wave given. This is for earth type conditions, with a wind shear of $3 m s^{-1} km^{-1}$ and static stability of $1{\cdot}8 \times 10^{-5} m^{-1}$.

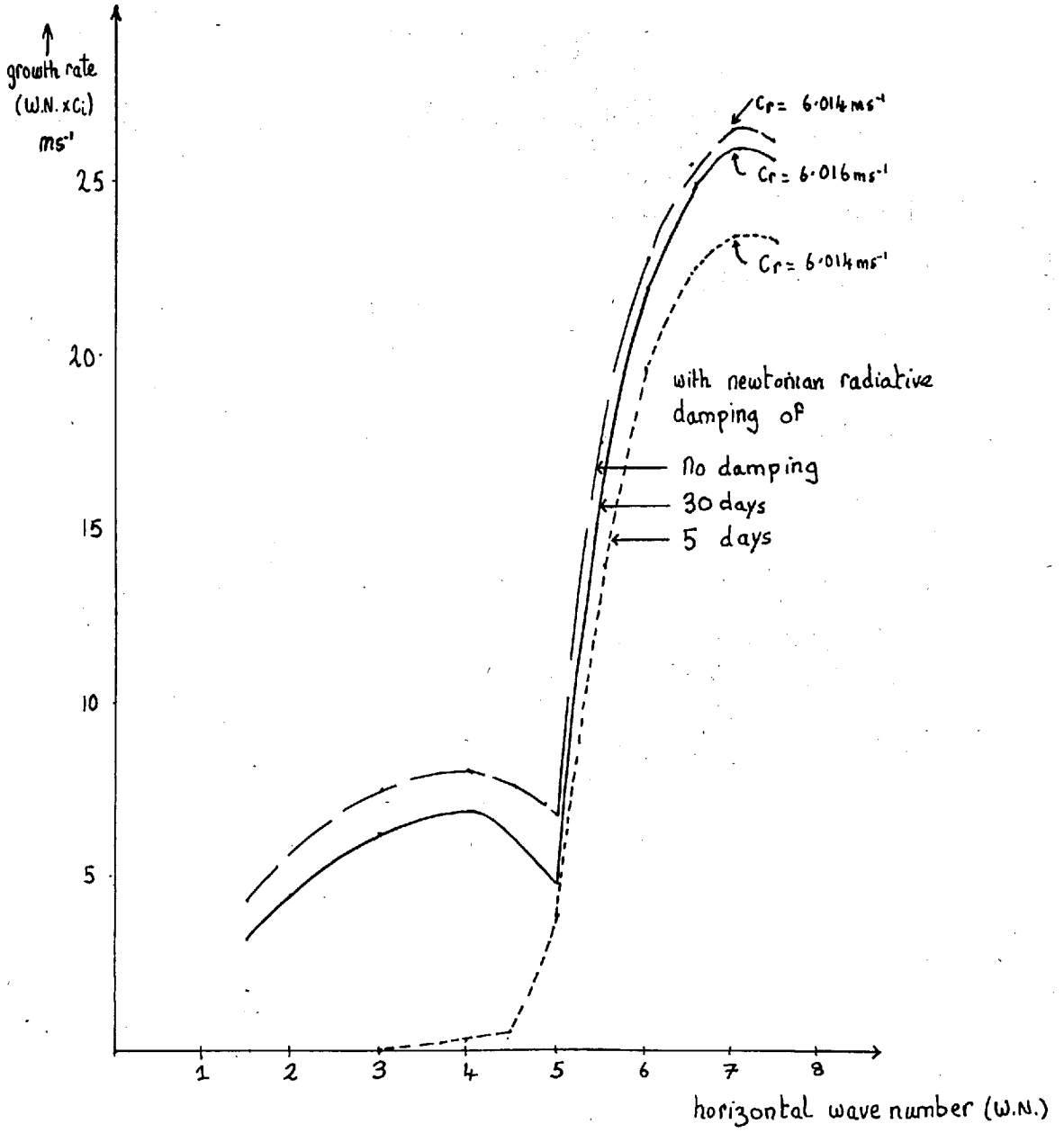

Figure 52. Graph of growth rate (W.N. x c_i) against horizontal wavenumber (W.N.) for a 25 level Green model (Eady model with density and Beta effects), with an upper lid at 10 km and with the phase speed of the most unstable wave given. This is for earth type conditions, with a wind shear of $3 ms^{-1} km^{-1}$ and static stability of $1·8 \times 10^{-5} m^{-1}$

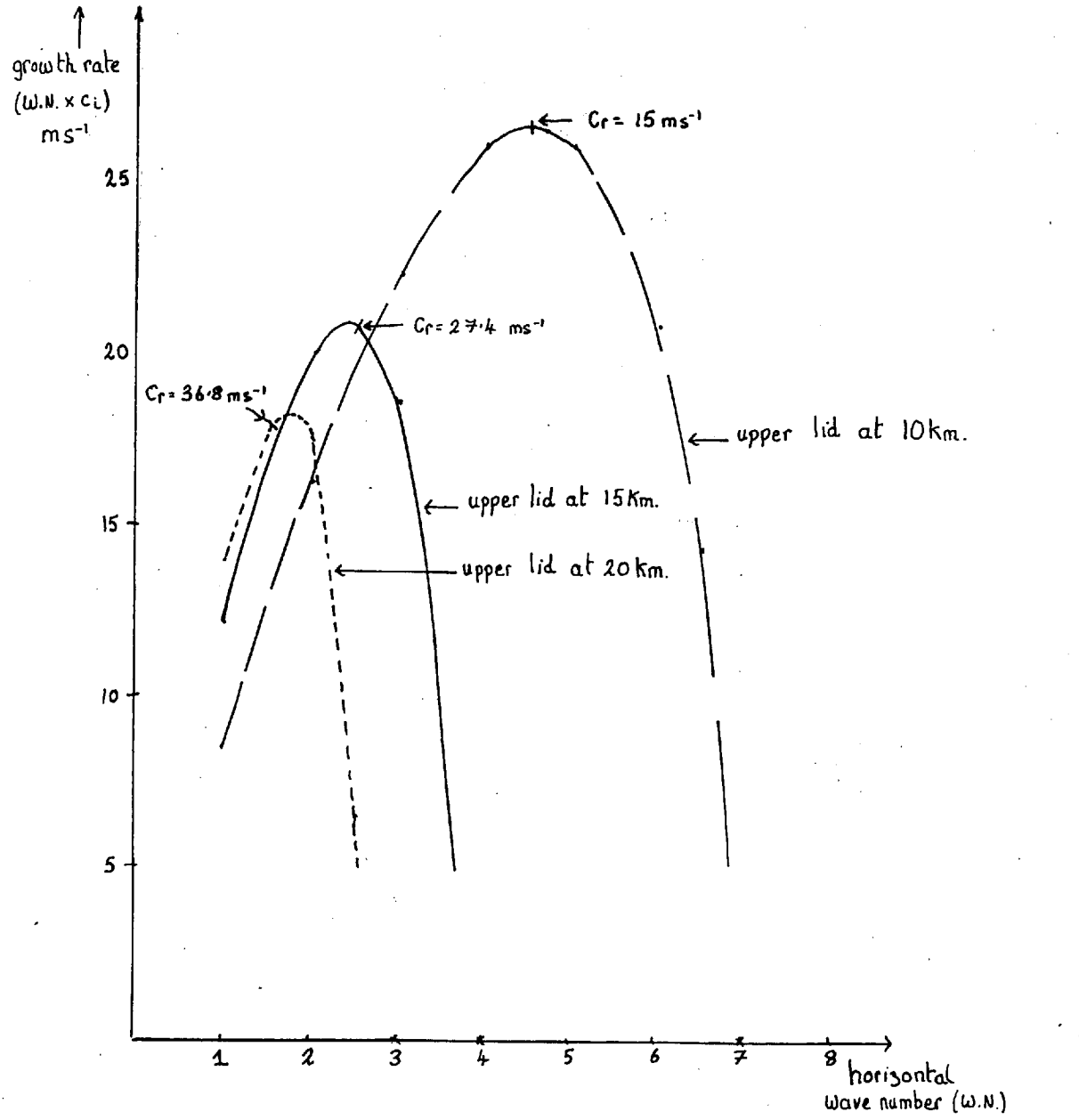

Figure 53. Graph of growth rate (W.N. × c_i) against horizontal wavenumber (W.N.) for a 25 level Eady model on the Earth, with a wind shear of 3 ms^{-1} km^{-1}, with static stability, $B = 1{\cdot}8 \times 10^{-5}$ m^{-1}, $z < 10$ km and $B = 5{\cdot}4 \times 10^{-5}$ m^{-1}, $z \geq 10$km, and with the phase speeds of the most unstable waves given.

is a reasonable value for the radiative damping time constant on the earth, but even a figure of 5 days produces little change in the maximum growth rates, and negligible effect on the phase speed. For the Eady model, the phase speed remains constant with and without radiation, as demonstrated theoretically in the previous chapter. With only the Beta effect, the radiation damping slightly reduces the phase speed, and with only the density variation there is a small increase in the phase speed. Overall therefore, realistic Newtonian cooling on the earth does not alter the phase speeds and maximum growth rates.

5.3 The effect of static stability, B, on the earth

It is interesting to determine the effect of increasing the static stability above a certain height, and also to discover the results obtained by raising the level of the upper boundary. Graph 53 illustrates the Eady model for upper boundaries at ten, fifteen and twenty kilometres, with a static stability three times greater above ten kilometres than below. Calculating analytically the growth rate for the Eady model with a lid at 20 km and a static stability which is an average of the tropospheric and stratospheric values given in Graph 53, then the most unstable wave has a growth rate of 18.7 ms^{-1} for wavenumber 1.6. These analytical results are very similar to the result obtained on Graph 53 with the lid at 20 km, although the phase speeds are different: 36.8 ms^{-1} as compared with the analytic solution of 30 ms^{-1}. Including the density and Beta effects as given in Graph 54 with upper lids at 10,15 and 20 km and with the static stability the same as in Graph 53, there is now little difference in the growth rates and phase speeds with the lids at the two higher positions. Thus the density and Beta effects have reduced the importance of the upper boundary condition, its height and the increase in static stability. The wave with its steering level at about two kilometres mainly appreciates the lower atmosphere. All the curves on Graph 54 agree reasonably well with observations in the troposphere: phase speeds of about 5-10 ms^{-1} with a

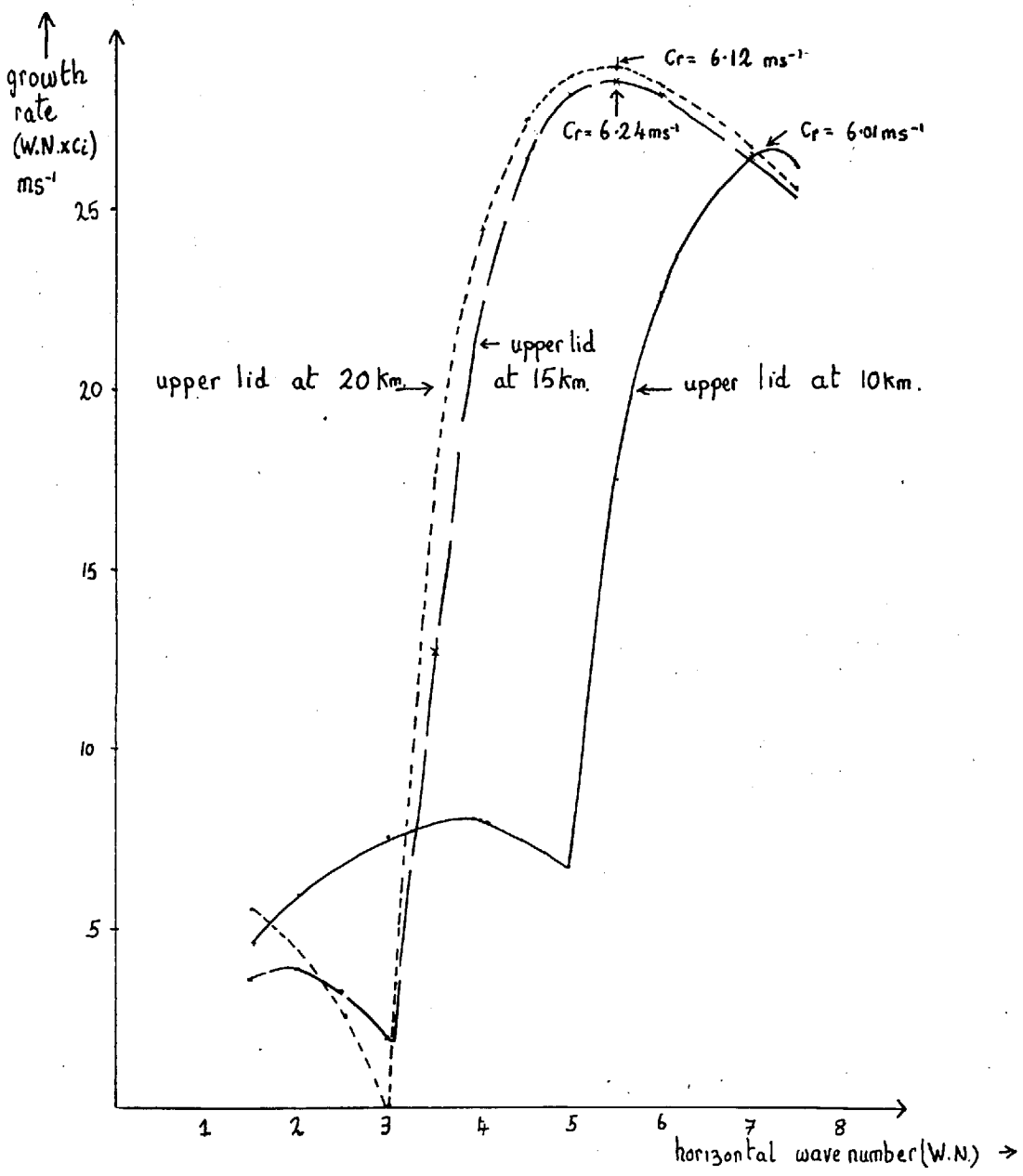

Figure 54. Graph of growth rate ($W.N. \times c_i$) against horizontal wavenumber (W.N.) for a 25 level Green model on the Earth, with a wind shear of $3 ms^{-1}$, with static stability, $\beta = 1{\cdot}8 \times 10^{-5} m^{-1}$ for $z < 10$km and $\beta = 5{\cdot}4 \times 10^{-5} m^{-1}$ for $z \gtrsim 10$km and with the phase speeds of the most unstable waves given.

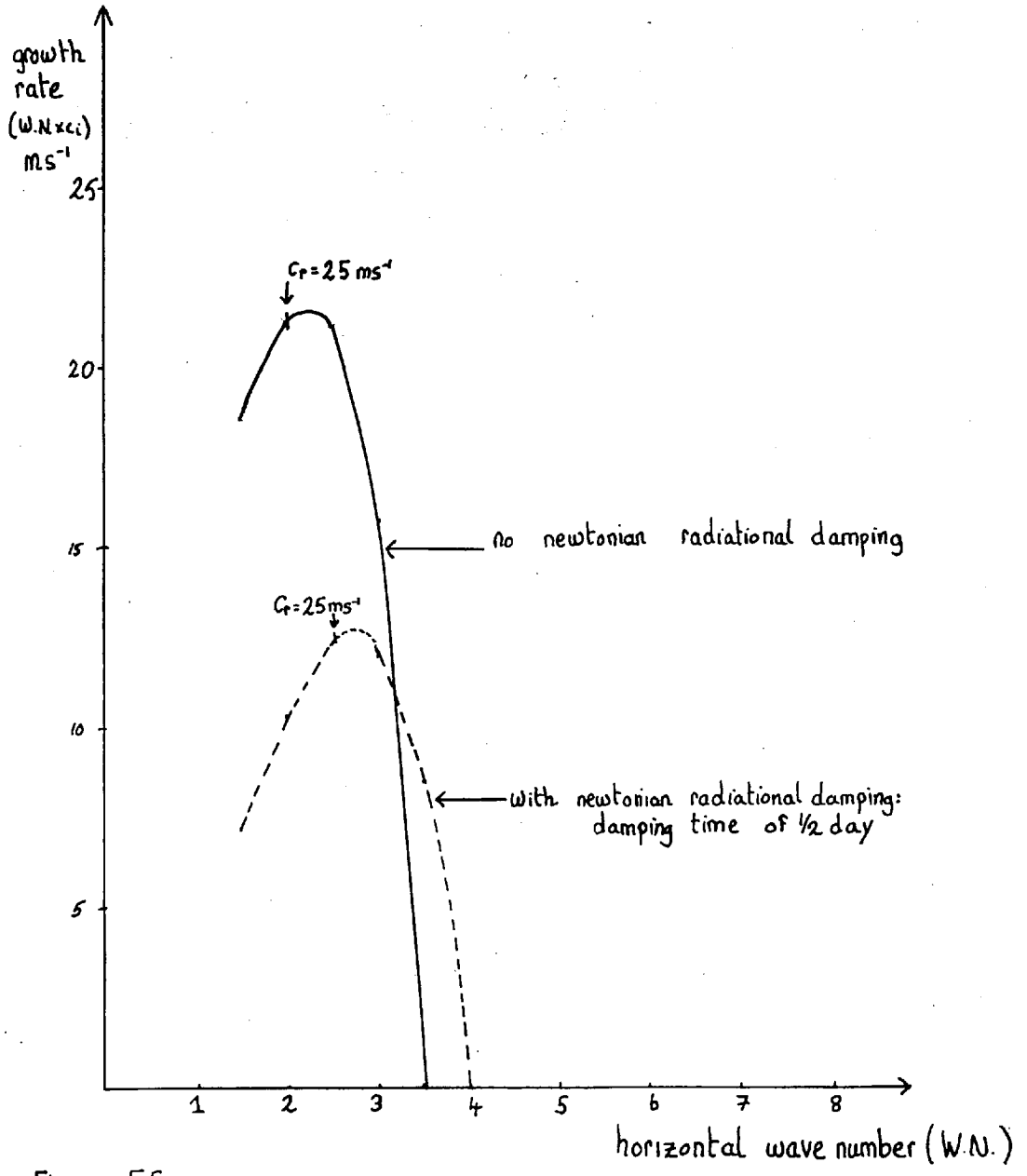

Figure 55. Graph of growth rate (W.N. x c_i) against horizontal wave number (W.N.) for a 20 level Eady model on Mars, with the phase speeds of the most unstable waves given. Results are evaluated with and without newtonian damping, with a static stability B of 1.5×10^{-5} m^{-1} and with a windshear of 5 ms^{-1} km^{-1}. The upper lid is at 10km.

horizontal wavenumber of about six. In the Eady model with constant value of static stability, the height derivative of the amplitude of the pressure disturbance vanishes at the steering level, but, with the addition of density and Beta, the amplitude is no longer symmetrical. When the static stability is discontinuous, this produces a non-differentiable point which must present errors in the finite differencing procedure. However since the convergence of eigenvalues is as good as the constant static stability computations, the results are valid.

Although this section was primarily designed to test the program, in doing so it clearly verifies that the density stratification, the Beta effect and the increased static stability reduces the importance of the upper boundary condition with westerly shear.

5.4 Radiational damping used in the computation for Mars

Most of the atmospheric mass is composed of carbon dioxide and the radiative relaxation time on Mars is much more rapid than on the earth (Goody and Belton, 1967). For a wave of vertical wavelength of 10 km, the radiative relaxation time is of the order of 1 day - $\frac{1}{2}$ day. Using Goody and Belton's (1967) results, with a lid at thirty kilometres or above, the radiative damping times will be less than 1/6 day. From solving the equations, we find that there are no growing waves for both the Green model and the model with F=0 as the upper boundary condition and this is the reason why we have only considered models with an upper boundary generally lower than thirty kilometres. In the rest of this chapter we will mainly consider the Green model, but graph 55 demonstrates the Eady model on Mars with the upper boundary at 10 kilometres. The static stability of $1.5 \times 10^5 m^{-1}$ is possibly a little too large when compared with the winter temperature profiles in the appendix, but these results demonstrate that the phase speed remains unaltered when Newtonian damping is included. The last section of Chapter Four shows that for large wavenumbers with small growth rates, the radiational damping increases a certain upper bound

on the growth rate. This implies that it is possible for the shape of the growth rate curve to change and consequently the wavelength of the most unstable wave. With density and Beta effects included, there is no short wave cut off and this effect is less noticeable. The upper lid in Graph 55 may appear to have been arbitrarily chosen at $10\frac{1}{2}$ kilometres but the results and analysis shown in the following paragraphs provides some justification.

5.5 The static stability, B, and discussion of the Green model on Mars

To interpret the solutions the values of various parameters must be inserted. Some information on some of these has been supplied by the Mariner 9 data. The temperature profiles give some values of the static stability and several computations were made to ascertain its effect and change of it on the growth rates. In the mid-latitude winter the cloud cover reduces the diurnal temperature change, but this variation remains and has been considered when producing values for the static stability B. A value for the shear is deduced by applying the thermal wind equation to the general mid-latitude winter temperature structure obtained from Mariner 9. As mentioned in Chapter three, this mid-latitude belt is where the baroclinic eddies are believed to be observed on the Mariner 9 photographs and with which the results of this model have been compared.

Graph 56 gives values of growth rates against wavenumber for three different static stabilities. In the Martian winter the static stability is about $1.0\times10^{-5}\ m^{-1}$. The most unstable wave increases its wavelength as we increase the static stability. Graph 57 is the same as 56 except that the lid height is reduced from twelve to eight kilometres. This merely scales the equations: reducing the lid height lowers the steering level and increases (in this example) by one the wavenumber of the most unstable wave. Both graphs show how the growth rates and phase speeds depend on the static stability; the growth rates and phase speeds being reduced by almost a factor of two for a three-fold increase in static stability from

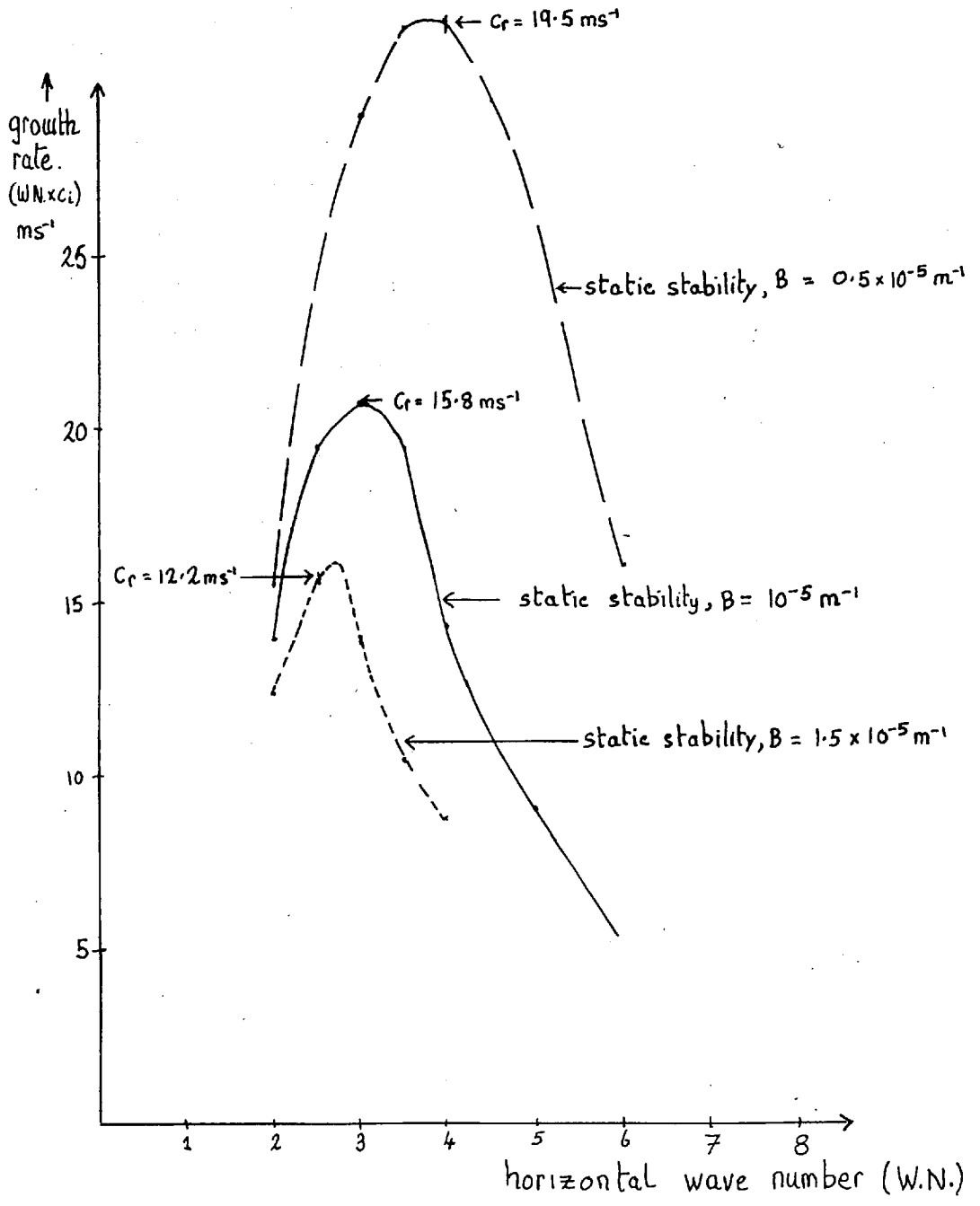

Figure 56. Graph of growth rate (W.N. xc_i) against horizontal wave number (W.N.) for a 20 level Green model on Mars, with phase speeds of the most unstable waves given. The results are calculated with a newtonian damping time constant of 1 day, with a wind shear of 5 ms^{-1} km^{-1} and with different values of static stability. The upper lid is at 12 km.

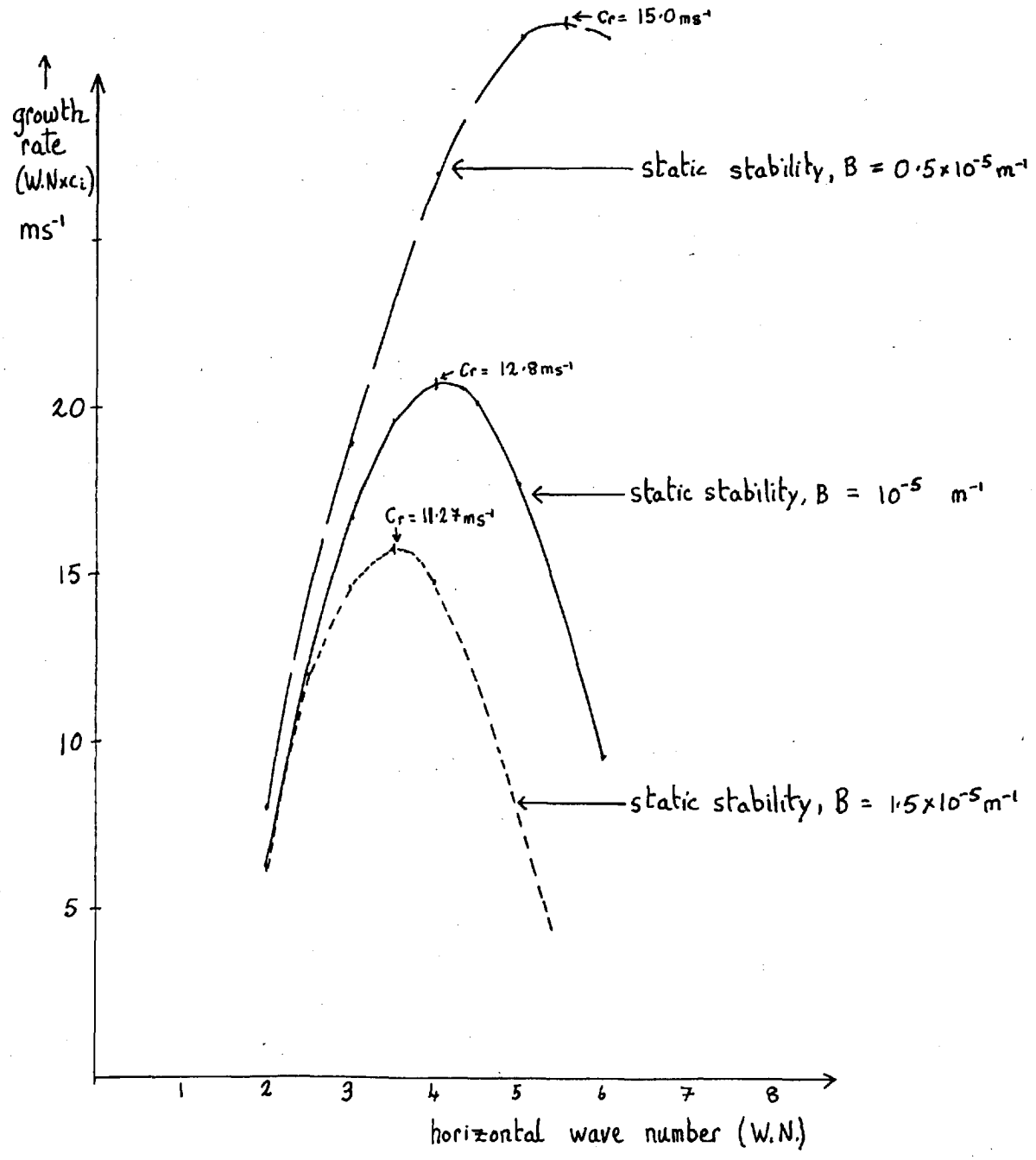

Figure 57. Graph of growth rate (W.N. x c_i) against horizontal wave number (W.N.) for a 20 level Green model on Mars, with phase speeds of the most unstable waves given. The results are calculated with a newtonian damping time constant of 1 day, with a wind shear of 5 ms^{-1} km^{-1} and with different values of static stability. The upper lid is at 8 km.

$0.5 \times 10^{-5}\ m^{-1}$. Thus it is important that we use in the computation the correct description of the static stability, but does imply that the diurnal temperature variation could induce eddies with phase speeds that vary throughout the day.

Graphs 58 and 59 give the results using a static stability that varies linearly with height. With the lid at 10 km, the maximum unstable wave has wavenumber 3 or 4 with a phase speed of about 14 ms^{-1}, whereas with a lid at 20 km the wavenumber is reduced to 2 or 3. The phase speeds are very close for both models and, in fact, as in Graph 54, the density and Beta effects reduce the importance of the height of the upper lid above about 15 kilometres. The radiational damping on Graphs 58 and 59 reduce the growth rates by about one half, but in fact do not affect the phase speeds by a large amount.

Graphs 510 and 511 indicate growth rate curves when the static stability is increased threefold from $10^{-5}\ m^{-1}$ above 10 km. From graph 510 we can deduce that placing the lid above 20 km in this model has very little effect on the phase speeds and growth rates. The addition of radiational damping (511) again only principally alters the growth rates. It is interesting to note that these results are similar to those given in Graphs 58 and 59 and thus generally we can argue that on Mars, the use of static stabilities which vary linearly with height do not give vastly different answers from the constant static stability solutions. Comparing the solutions on Graphs 510 and 511 for the upper lid at 10 km, with the results on Graph 58, we find that the constant static stability profiles are consistent with the more accurate profiles used in Graph 58.

Graphs 512 and 513 illustrate eigenfunctions corresponding to Graphs 59 and 511, which give results for the Green model, with a lid at 20 km, with a vertically varying static stability (Graph 59) and for the discontinuous static stability profile (Graph 511). The phase change with height to the west, is similar for both curves, although there is an abrupt change in the slope of the eigenfunction for curve 513 at the level where

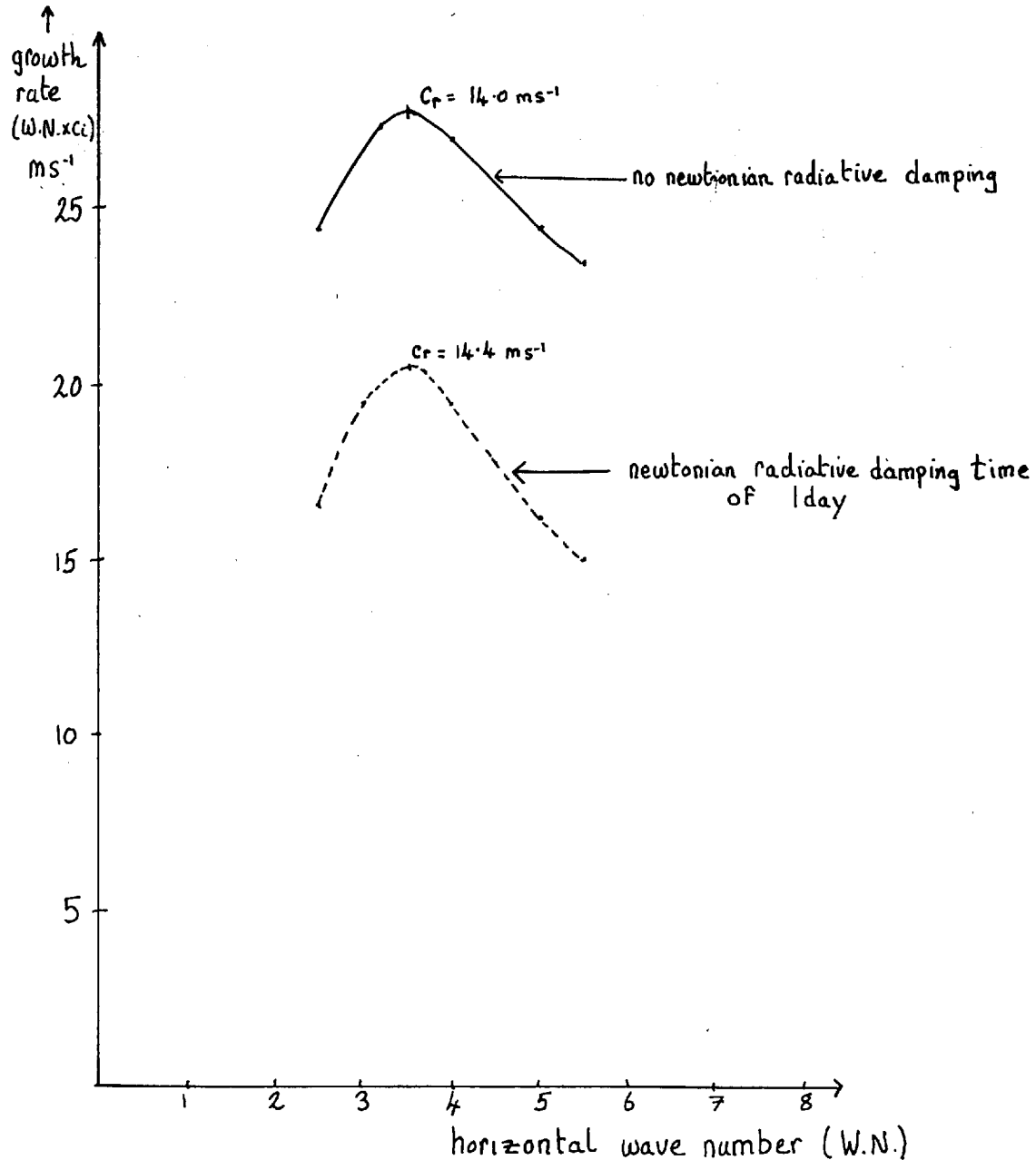

Figure 58, Graph of growth rate (W.N. x ci) against horizontal wave number (W.N.) for a 20 level Green model on Mars, with the upper lid at 10km. and with the phase speeds of the most unstable waves given. The results are calculated with a wind shear of $5ms^{-1}km^{-1}$, with and without newtonian damping and with static stability, B s.t. $B = \frac{10^{-5}}{2}(1 + z/4km.)\ m^{-1}$

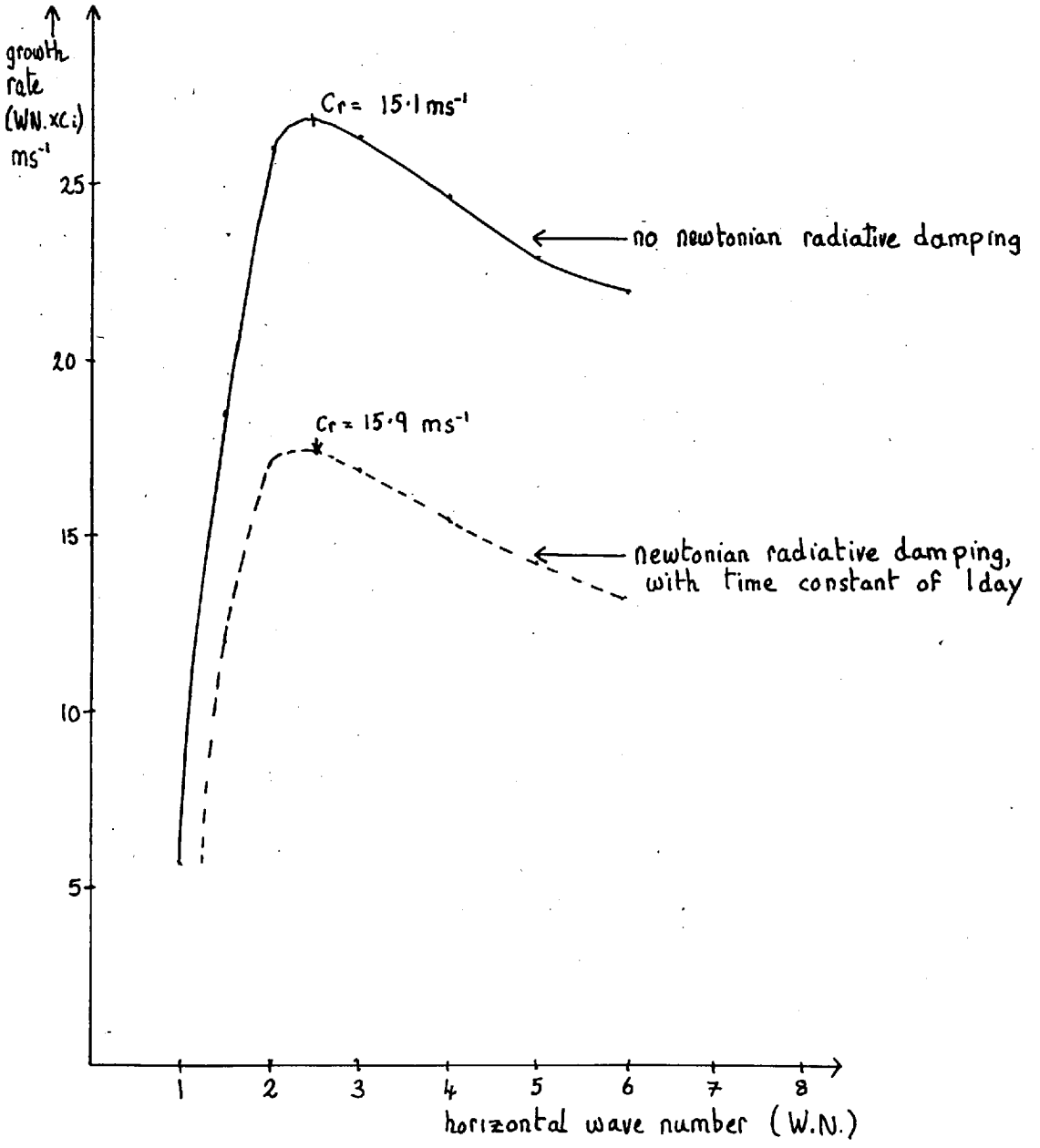

Figure 59. The same as for Figure 58 except with the upper lid at 20km.

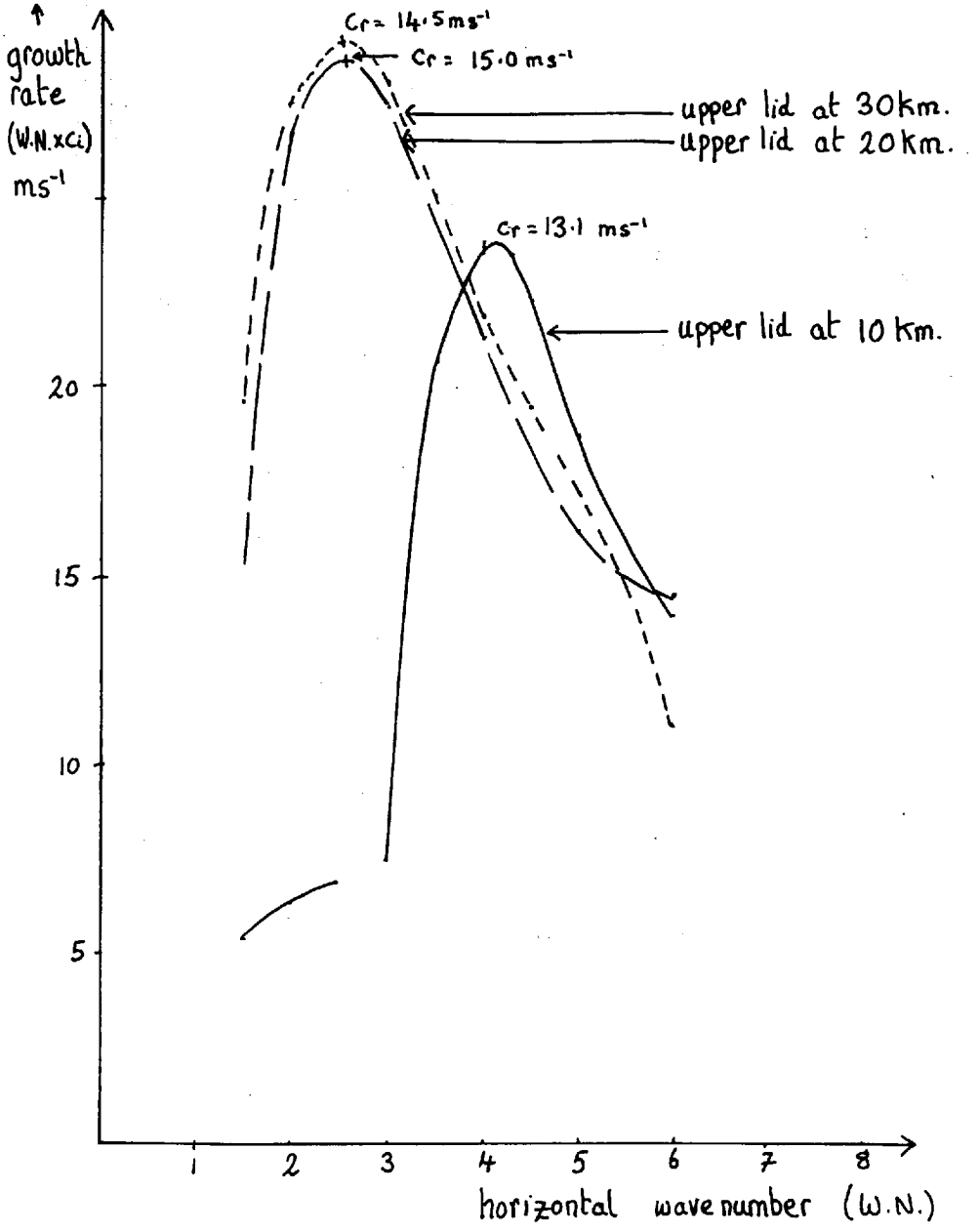

Figure 510. Graph of growth rate against horizontal wavenumber (W.N.) for a 20 level Green model on Mars, with the phase speeds of the most unstable waves given. The results are calculated with a wind shear of $5 ms^{-1} km^{-1}$, no newtonian damping, and with a static stability B, s.t. $B = 10^{-5} m^{-1}$ for $z < 10$ km and $B = 3 \times 10^{-5} m^{-1}$ for $z \geq 10$ km.

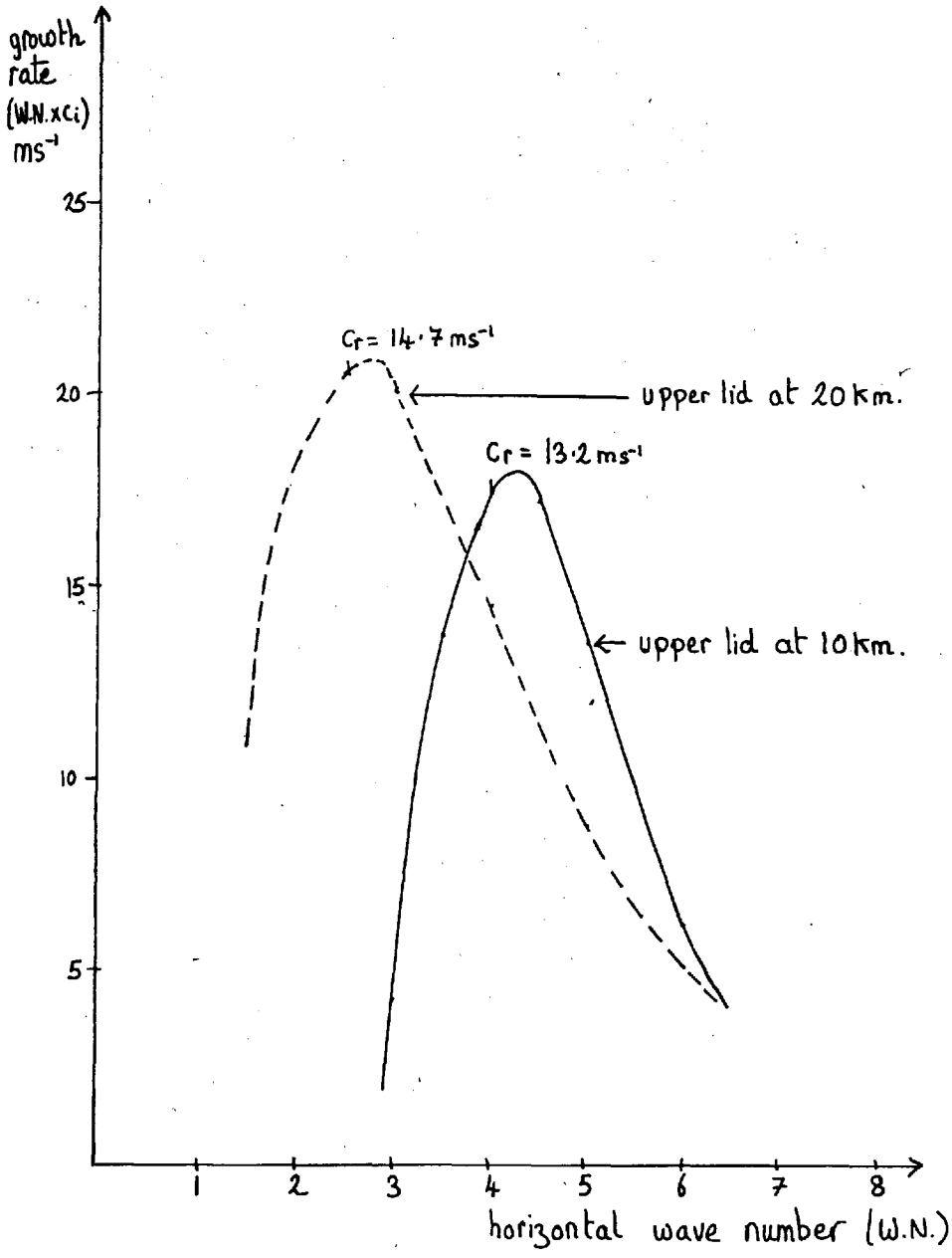

Figure 511. The same as Figure 510, but with lids at 10 km. and 20 km only and with a newtonian radiational damping time constant of 1 day

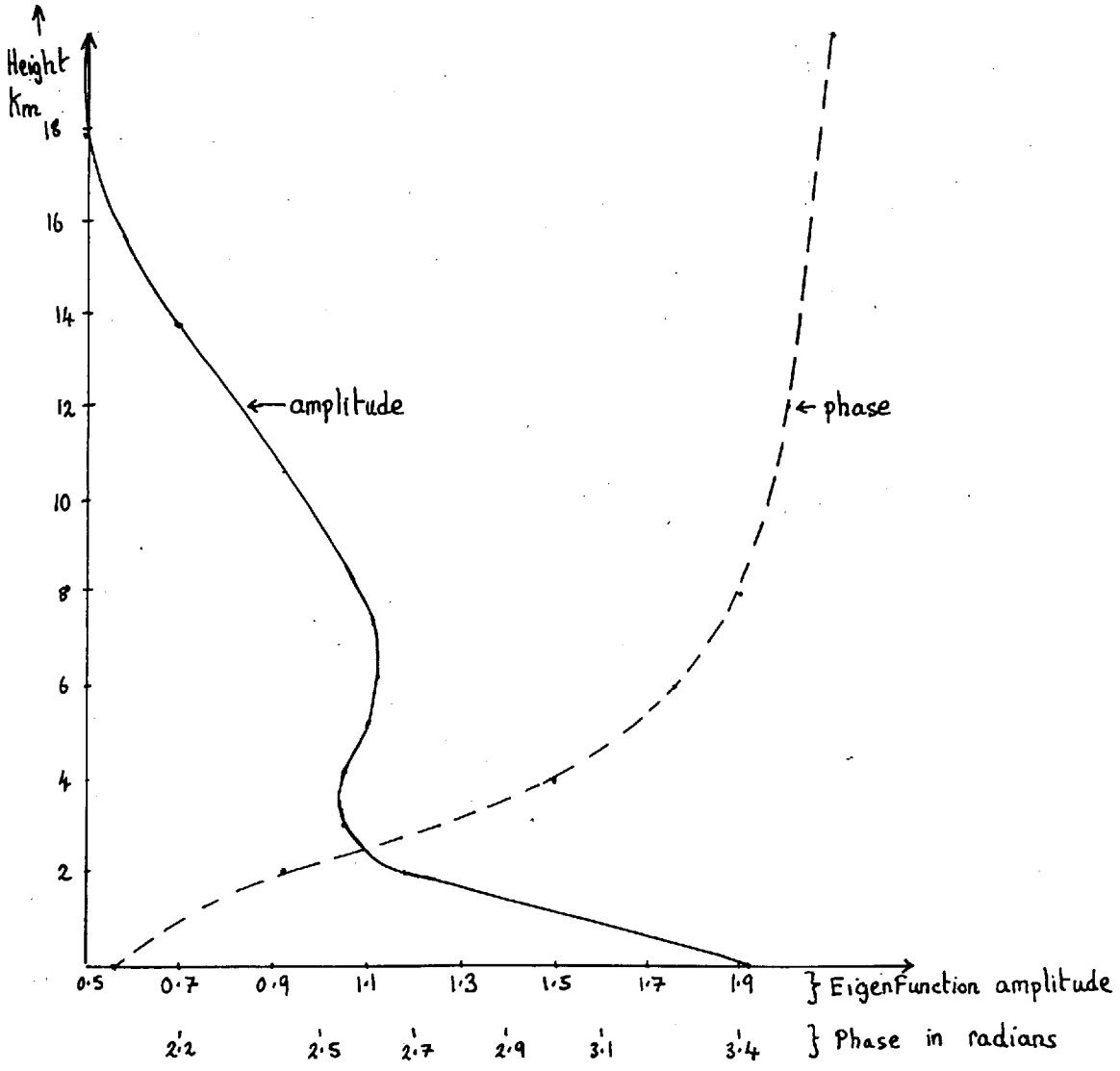

Figure 512. Graph of amplitude and phase of the eigenFunction $F(z)$, as a Function of height, as given by the most unstable wave on the no radiational damping curve on figure 59.

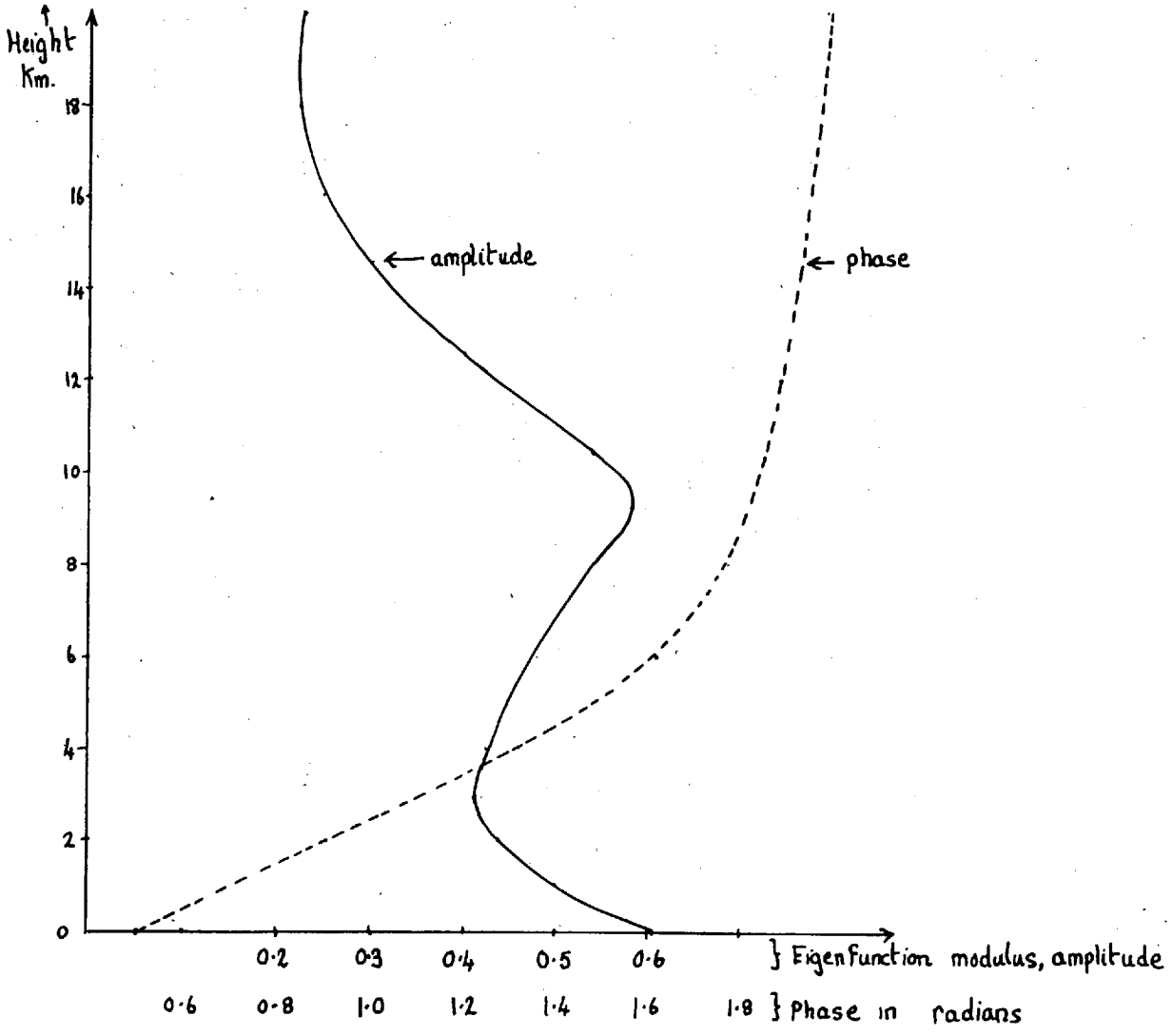

Figure 513. Graph of amplitude and phase of the eigenfunction $F(z)$, as a function of height, as given by the most unstable wave on the curve on Figure 511 with the upper lid at 20 Km.

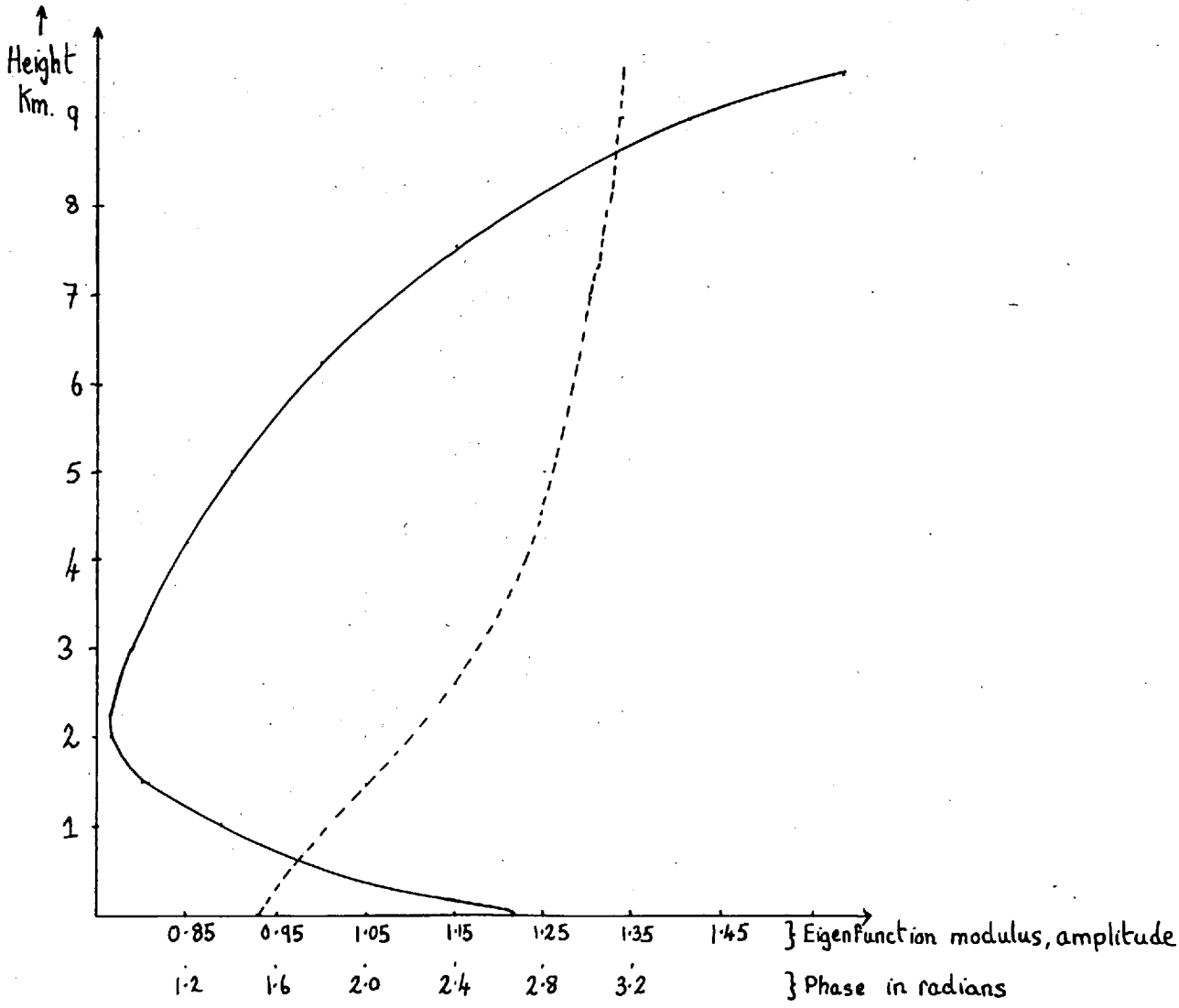

Figure 514. Graph of amplitude and phase of the eigenfunction $F(z)$, as a function of height, as given by the most unstable wave on the curve with no newtonian damping on figure 52.

the static stability is discontinuous. Despite the fact that the results on Graph 516 are calculated with radiational damping, the shape of the eigenfunction and the phase remains almost the same with or without any Newtonian damping and so the comparison of eigenfunctions on Graph 516 with Graph 515 is valid. It is only in the Eady model that we find that the level where the amplitude of the wave is minimum (or where the slope of the modulus of the eigenfunction is zero) corresponds to the steering level of the wave. However from all the solutions of the differential equation the steering level is within one or two kilometres of this level. Graph 514 is the eigenfunction corresponding to the no-radiation damping curve for the Green model on Graph 52. These curves for phase and amplitude are typical of those obtained for the Green model with constant static stability.

5.6 Solutions for F=0 as the upper boundary condition

This boundary condition is used because we think that the large radiative damping would drastically reduce the perturbation of the stream function with height. Although this is not as physically clear as putting the vertical velocity to zero, this is a useful approximation in heavily damped atmospheres like Mars and would be valuable to compare the results with the Green type solutions. Graphs 515 and 516 indicate solutions obtained with different static stabilities. These compare with Graphs 58, 59 and 511, but it must be remembered that we have neglected lids over 30 km and radiational of less than 1/6h day. Graph 515 demonstrates that with F=0 at 10 kilometres, a phase speed of 16.6 ms^{-1} with a maximum unstable wave at wavenumber four is produced. The results are dissimilar to those obtained with a lid at 10 kilometres on Graph 511; with lids at 20 km, the results on Graph 515 are similar to those on Graph 511. This is consistent with the previous section where it was demonstrated that the height of the upper lid in the Green model is unimportant above 20 kilometres. The results on Graph 516, are to be compared with Graphs 58 and 59. With the lids at 10 and 20 km, there seems to be little connection between these graphs of

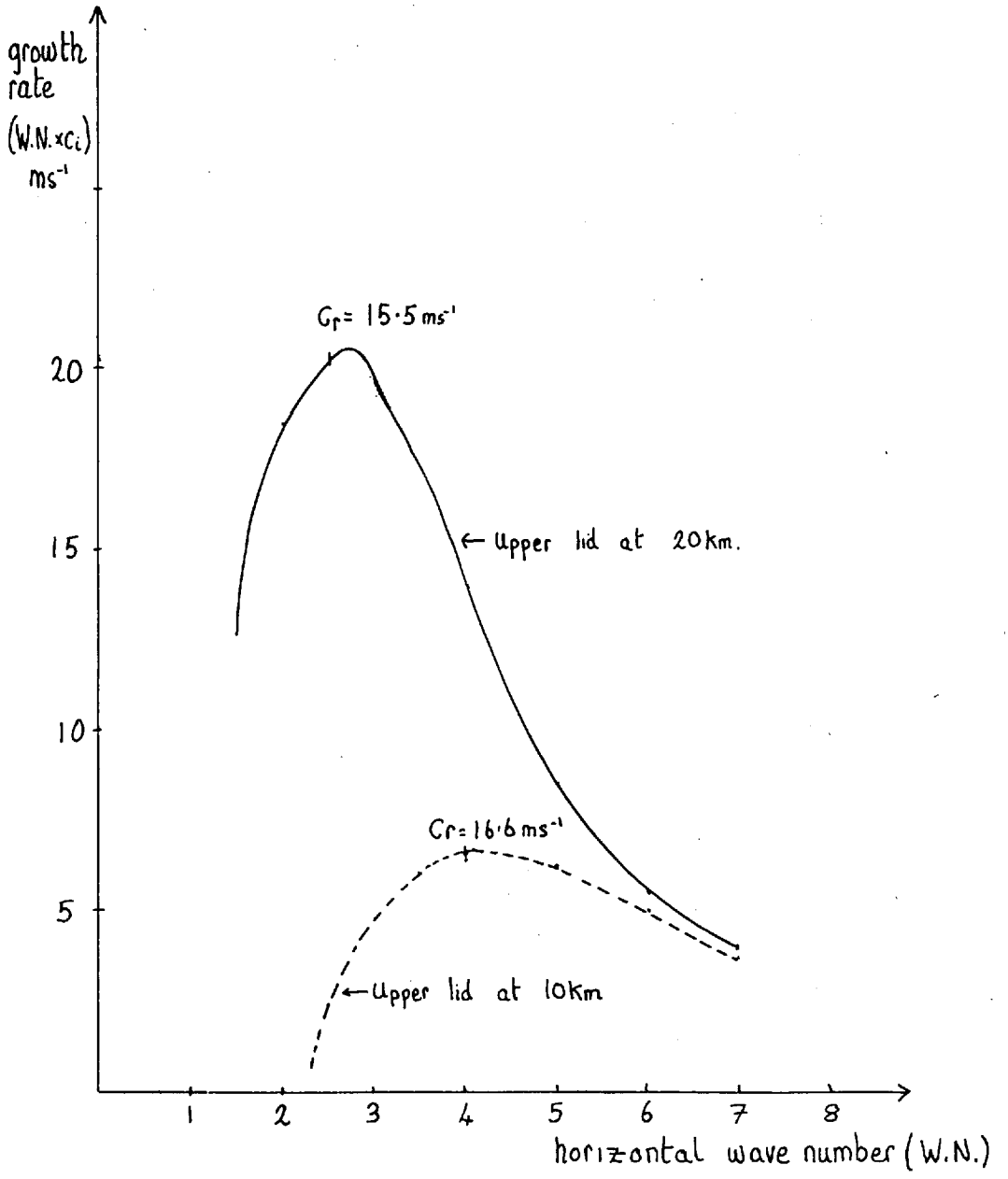

Figure 515. Graph of growth rate against horizontal wavenumber for a 20 level 'F=0' model on Mars, with upper lids at 10km. and 20km. and with the phase speeds of the most unstable waves given. The results are calculated with density and Beta effects, with a wind shear of 5 ms^{-1} km^{-1}, a newtonian radiative damping time constant of 1/day, and with a static stability B s.t. $B = 10^{-5}$ for $z < 10$km and $B = 3 \times 10^{-5}$ for $z \geq 10$km.

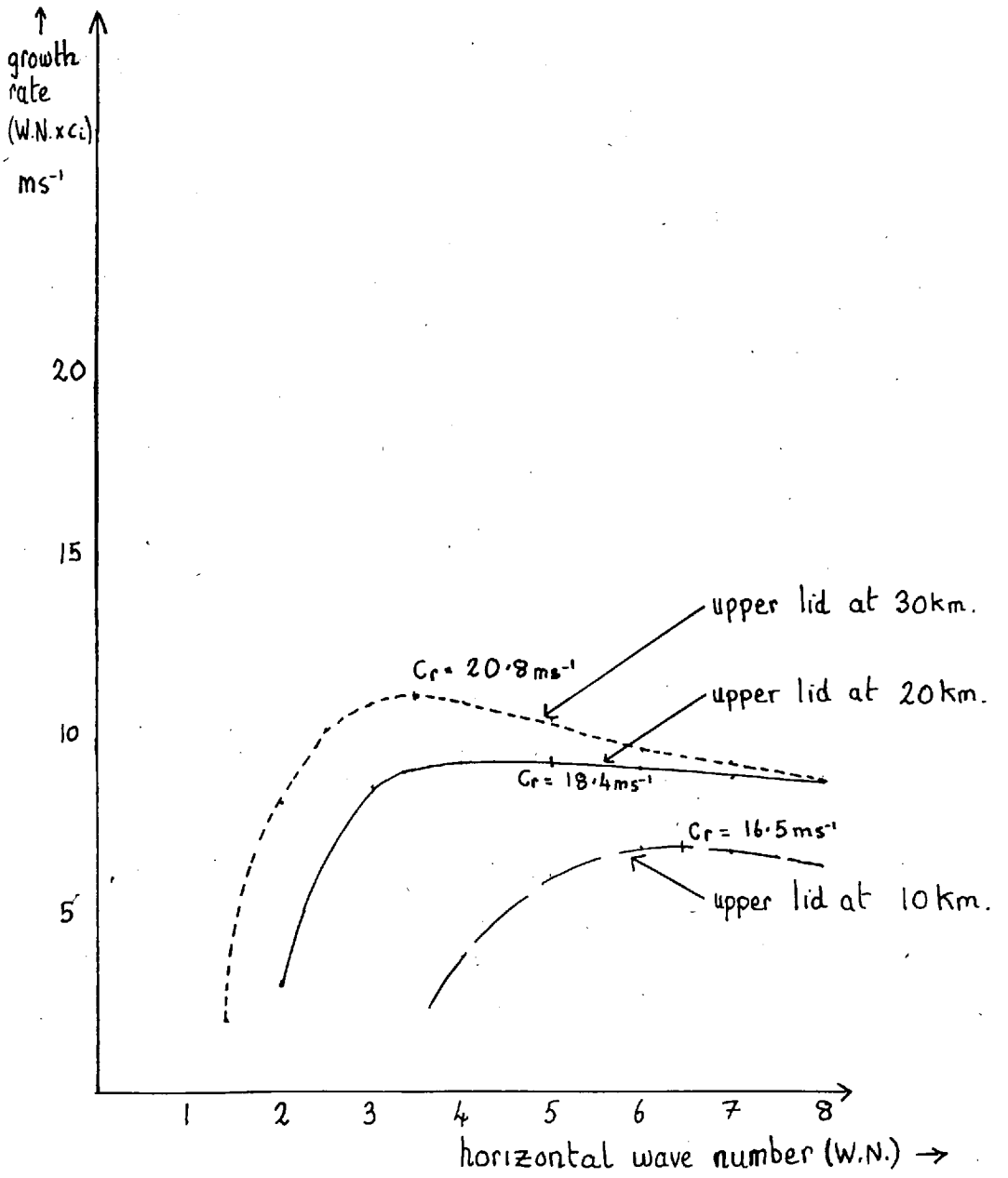

Figure 516. Graph of growth rate against horizontal wavenumber for a 30 level "F=0" model on Mars, with the upper lids at 10km, 20km and 30km and with the phase speeds of the most unstable waves given. The results are calculated with density and Beta effects, with a wind shear of 5ms^{-1} km^{-1}, a newtonian radiative damping time of 1 day, and with a static stability B s.t.

$B = 10^{-5}/2\ (1 + z/4km)\ m^{-1}$

the Green and F=0 model, although with the lids at 20 km the most unstable wave has a wavenumber of about three.

The constructive comment coming from this model is that the growth rate curves have almost the same wavenumber for the most unstable wave and a similar general shape, although different magnitudes when compared with the Green type model. The F=0 boundary condition, as mentioned before, is more arbitrary than using zero vertical velocity as the upper lid and therefore less emphasis has been placed on these results.

5.7 General comments

With constant static stabilities, and large radiational damping time of 1 or $\frac{1}{2}$ day for the Green model with upper lids at 8 and 10 km, the phase speeds of the very long waves of wavenumber 1.5 or 2 are negative. Without Newtonian damping and when the upper lid is at 12 kilometres or above, this result is not apparent. With the upper boundary at 8 km, wavenumbers 1.5 and 2 have negative phase speeds, whereas with the lid at 10 km, this effect is only noticed with wavenumber 1.5. The reason for these waves having a steering level below the ground is unclear, but the reduction of the lower bound on the phase speed, when Newtonian damping is included, is mentioned in the previous chapter. In addition these waves are not very unstable when compared with the growth rate of the most rapidly growing waves and thus are not likely to be observed on Mars. These results are not features of the numerical computations since, as shown in Graph 54, there is good treatment of the critical wavelength regions where the growth rates are very small.

This analysis has not been applied to the summer hemisphere. The equator pole temperature gradients are generally less than $20^{\circ}K$ and in mid-summer the pole is believed to be warmer than the equator. Since there are no clouds visible in the southern hemisphere on the Mariner 9 photographs, it is impossible to say whether these baroclinic eddies exist. The winter hemisphere photographs imply there are eddies. Photographs 31 and 32, from Chapter 3, are thought to show evidence of cold fronts. Estimation

of the motion of these fronts and the waves found in Figures 32 and 33 suggest phase speeds of 10-15 ms^{-1}. Analysis of the cloud patterns observed in these photographs and in figures 34 and 35 suggest wavenumber four. The results from the numerical model agree with this computation from the photographs: with graphs 511 and 58 being a reasonable representation of the static stability, and with the upper lid at ten kilometres. Some of the temperature profiles in this region suggest isothermal temperatures, in which static stabilities of $1.5\times10^{5}\,m^{-1}$ or more are suitable; graphs 56 and 57 show solutions to these equations. There is no evidence to suggest that these waves are surface features, since the background cloud forms part of the north polar carbon dioxide ice cloud canopy. and the surface is not visible. Alternatively these waves could be topographically forced, but I shall consider this possibility in the following two chapters. In the next section we shall discuss the computation of poleward baroclinic eddy heat fluxes on Mars using Green's (1970) transfer coefficient theory.

5.8 Baroclinic heat fluxes

Since the amplitudes are assumed to be infinitesimally small, the eigenvectors cannot be used to calculate the magnitude of the heat fluxes, only their general height structure. Several techniques have been used to calculate baroclinic heat fluxes and in this thesis I will modify Green's (1970) theory and compare it with Stone's (1972) similar principle.

Green produces a northward flux of entropy defined by

$$\overline{v\phi}^{xtp} = \alpha^{*}(g/B)^{1/2}(\Delta\phi)^{2} \qquad -(5.0)$$

where $\Delta\phi$ is the change in entropy with latitude and where α^{*} is the ratio of the growth rate to the frictional damping time scales. This heat flux occurs during the active phase of the generation of baroclinic eddies when here is a positive correlation between the poleward velocity v and the entropy ϕ and this affects the value of α^{*}. No values for large scale frictional damping are known for Mars, since even if the proportionate

difference in mountain size is quantifiable, it is not known if the flow manages to pass over the taller ranges and mountains. If we compare the amplification time scale and the Newtonian damping time of about 1 day, then α^* could have a value of at most 0.01, compared with an earth value of 0.0055. Thus Newtonian cooling could be more important on Mars than frictional dissipation is on the earth, and thus possibly on Mars. Substitution of typical Martian parameters, with $B \simeq 10^{-5}\,m^{-1}$ and $\Delta\phi \sim 0.3$, produces a value for $\overline{v\phi}^{xtp}$ of 0.1 to 0.2 ms^{-1}, although this solution is probably too large. The Beta effect lowers the steering level, where the maximum poleward heat transfer occurs, to within a few kilometres of the ground. Saltzman (1968) does a similar analysis. By considering the amplification of the perturbation solutions of the quasigeostrophic formulation of the potential vorticity equation with dissipation due to frictional damping, he is able to calculate the poleward heat flux. Since this method requires observational values for the drag coefficient, I have not applied this study to Mars.

Stone (1972), using the longitudinal variation of incoming solar radiation with no albedo differences, calculates the pole equator surface temperature gradient and corresponding air temperature gradients. The radiative fluxes are balanced by the fluxes of sensible heat and potential energy from the large scale eddy motions. He uses a type of cooling which has a similar formulation to that used in my quasigeostrophic solutions. By assuming that the perturbation meridional velocity is the same as the vertically averaged amplitude of the baroclinic component of the mean zonal velocity he obtains

$$\overline{v\theta}^{xtp} = k\,u\,\frac{d\theta}{dz}\cdot\frac{18}{25\sqrt{30}}\cdot\frac{(1+R_i)^{5/2}}{R_i}$$

k is the amplitude factor equal to $1.09\,(1+R_i)^{-2}$ and Ri is the Richardson number such that

$$R_i = F^2 T_0 \frac{d\theta}{dz} \Big/ g\left(\frac{d\theta}{dy}\right)^2$$

H is the depth of the fluid between the boundaries in the Green model and

more generally the depth of the Boussinesq atmosphere or scale height of the real atmosphere. Although Stone does not explain this, these heights are roughly comparable on Mars. The velocity u is the magnitude of the unperturbed zonal wind resulting from the poleward temperature gradient, and where T_o is the characteristic temperature. Thus for large Richardson numbers we obtain:

$$\overline{v\theta}^{xtp} = 0.216 \frac{gH^2}{T_o f^2} \left(\frac{d\theta}{dy}\right)^2 \left(\frac{g}{T_o}\frac{d\theta}{dz}\right)^{1/2} \qquad (5.1)$$

This gives a value of α^* in equation (5.0) on the earth of 5.5×10^{3}, the same as Green's calculation. This is amazing, not only because of the uncertainty in the parameter representing the depth of the fluid but also because Stone shows that in his determination of the heat fluxes, Green's dimensionless constant α^* depends on B. Thus Green's poleward heat flux depends on $B^{-\frac{1}{2}}$ and Stone's heat flux depends on $B^{\frac{1}{2}}$. However, using Stone's equation we obtain a poleward heat flux $\overline{v\theta}^{xtp}$ of about 45 $ms^{-1}\,{}^{o}K$, which is almost the same as that obtained from equation (5.0). The difference between the two heat fluxes is consistent with the fact that, despite Stone's claim, there is a difference of about 20% in the actual value of α^*.

5.9 Concluding comments

In later chapters we will compare these results with the heat fluxes produced by stationary long waves in the Martian atmosphere. There is apparent agreement with Mariner 9 photographs and the theoretical calculations of the phase speeds of the eddies. The vertical fluxes of heat associated with baroclinic eddies are not sufficient to modify substantially the theoretical temperature profiles in Chapter 2. Stone (1972) using Green's (1970) transfer theory, calculated that the temperature profile was modified by, at most $1^{o}K/km^{+1}$, by these vertical heat fluxes. I have not repeated the calculation here, but this figure is not large enough to explain the difference between the radiative and the observed profiles.

However, as mentioned in Chapter 2, combined with a larger atmospheric dust content, the observed temperature profiles could be more fully understood.

CHAPTER 6: THE THEORY OF LONG TOPOGRAPHICALLY FORCED WAVES ON MARS

6.0 Introduction

As we noted in Chapter 2 the topography is large when compared with the density scale depth of the atmosphere. Thus we inferred that it would be important to consider long waves forced by these mountain ranges. In this and the following chapter we shall consider waves which have no growth rate and are stationary with respect to the surface. Solutions of the vorticity equation are obtained in spherical polars, since we shall consider wavenumbers one or two, where the Beta plane approximations are not very good. I have only considered parameters typical of the winter hemisphere, since this thesis is mainly concerned with the winter hemisphere and also since a mean wind shear is not very well defined as the pole equator temperature gradient changes sign in midsummer. If weak easterlies are found, then necessarily these waves would be very quickly damped in the vertical. In addition, the whole topic of vertical convection in the summer hemisphere has been neglected since in itself it would fill a thesis.

6.1 The equation

Charney and Drazin (1961) studied this problem of heat transfer by long waves. We shall discuss the main points from this theory and suggest where my model differs from Charney's. From the quasi-geostrophic potential vorticity equation we have

$$\frac{D}{Dt_h}\left\{\nabla_h^2(\psi) + 2\Omega\cos\theta + \frac{f^2}{gB}\left(\frac{\partial^2\psi}{\partial z^2} + \frac{B}{\rho}\frac{\partial}{\partial z}\left(\frac{\rho}{B}\right)\frac{\partial\psi}{\partial z}\right)\right\} + \frac{\alpha f^2}{g\rho}\frac{\partial}{\partial z}\left(\frac{\rho}{B}\frac{\partial\psi'}{\partial z}\right) = 0 \qquad - (6.0)$$

where Ω is the angular velocity of the planet, θ is colatitude, ψ is the streamfunction and with ξ_z the vertical component of vorticity such that

$$\xi_z = \nabla_h^2\,\psi = \frac{1}{R\sin\theta}\frac{\partial}{\partial\theta}\left(\frac{1}{R}\frac{\partial\psi}{\partial\theta}\sin\theta\right) + \frac{1}{R\sin\theta}\frac{\partial}{\partial\phi}\left(\frac{1}{R\sin\theta}\frac{\partial\psi}{\partial\phi}\right)$$

$\frac{D}{Dt_h}$ is the horizontal derivative following the motion and in spherical polars is defined by:

$$\frac{D}{Dt_h} = \frac{\partial}{\partial t} + \frac{1}{R^2}\frac{\partial \psi}{\partial \theta}\sin\theta\frac{\partial}{\partial \bar{\phi}} - \frac{1}{R^2}\frac{\partial \psi}{\partial \bar{\phi}}\frac{\partial}{\partial \theta}$$

α is the inverse radiative damping time as given for baroclinic eddies.

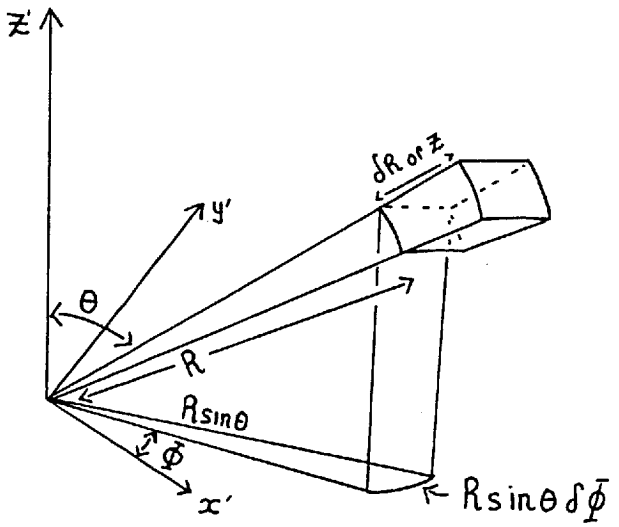

Figure 60: Spherical polar Coordinates $(R, \theta, \bar{\phi})$

$$\psi = -\cos\theta\,\bar{\psi}^{\bar{\phi}}(z) + \psi'(\theta, \bar{\phi}, z, t)$$

Ignoring all the second order terms, for stationary waves and with

$$\psi' = \mathrm{Re}\left\{F(z).\,H(\theta).\,e^{im\bar{\phi}}\right\}$$

where m is the horizontal wavenumber, we obtain

$$\frac{1}{H(\theta)\sin\theta}\cdot\frac{d}{d\theta}\left(\sin\theta.\frac{d}{d\theta}(H(\theta))\right) + 2 - \frac{m^2}{\sin^2\theta} + \frac{R^2}{\bar{\psi}^{\bar{\phi}}}\left\{\frac{f^2}{gB}\left(-\frac{\partial^2\bar{\psi}^{\bar{\phi}}}{\partial z^2}\right.\right.$$

$$\left.\left. + \frac{\bar{\psi}^{\bar{\phi}}F''}{F} - \frac{B}{\rho}\frac{d}{dz}\left(\frac{\rho}{B}\right).\left(\frac{\partial\bar{\psi}^{\bar{\phi}}}{\partial z} - \frac{\bar{\psi}^{\bar{\phi}}F'}{F}\right)\right) - \frac{Ria f^2}{mg\rho F}\frac{d}{dz}\left(\frac{\rho F'}{B}\right) + 2\Omega\right\} = 0$$

We assume that the perturbation stream function ψ' can be separated into functions of z, θ and $\bar{\phi}$. In addition we make the standard assumption that there is a constant Coriolis parameter.

Extracting only the θ terms from the above equation, then $H(\cos\theta) = P_n^m(\cos\theta)$ is a solution, where m is the horizontal wavenumber, $P_n^m(\cos\theta)$ is the associated legendre polynomial and where

$$\frac{d}{dp}\left\{(1-p^2)\cdot\frac{d\,H(\cos\theta)}{dp}\right\} - \frac{m^2}{1-p^2}\cdot H(\cos\theta) = -n.(n+1)$$

p is $\cos\theta$ and n is a new quantum number which determines some aspects of the meridional structure. n must be mathematically greater than m, and we shall choose n-m equal to one since this puts the function to zero at the equator and pole, with one or n-m meridional peaks. This is only a very brief summary of the associated legendre polynomials used here, but it is sufficient to use in this longwave theory.

Thus from the differential equation we can obtain

$$\frac{B}{\rho}\frac{d}{dz}\left(\frac{\rho}{B}\cdot\frac{dF}{dz}\right)\left\{1-\frac{R^2 i\alpha}{m\,\bar{\psi}^{\bar{\phi}}}\right\} + F\left\{\frac{gB}{f^2}\left(\frac{2\Omega}{\bar{\psi}^{\bar{\phi}}} + \frac{2-n.(n+1)}{R^2}\right)\right.$$

$$\left. -\frac{B}{\rho\,\bar{\psi}^{\bar{\phi}}}\frac{d}{dz}\left(\frac{\rho}{B}\frac{d\bar{\psi}^{\bar{\phi}}}{dz}\right)\right\} = 0 \qquad - (6.1)$$

Define $G = \frac{\alpha R^2}{m\,\bar{\psi}^{\bar{\phi}}}$. This is a non-dimensional radiational damping term: with no damping α and G are zero and the smaller the time constant the greater the Newtonian damping and the constant G. This number can be considered as a ratio of the damping time to the horizontal wavenumber multiplied by the mean angular velocity of the solid body rotation of the atmosphere. The smaller the value of the horizontal wavenumber m, the longer a parcel of air will stay in a perturbed part of the wave and thus the greater the radiational damping. This has been shown also in the results obtained from the baroclinic eddy model on Mars, where the long-waves are damped more than shorter waves, decreasing the wavelength of the most unstable wave. Expressing the wind speed u, we have

$$\bar{u}^{\bar{\phi}}(\theta,z) = \frac{1}{R}\frac{\partial}{\partial\theta}\left(\psi\right) = \frac{1}{R}\sin\theta\;\bar{\psi}^{\bar{\phi}}(z)$$

which comes from $V_H = K_n \nabla_h \psi$

This is consistent with the mean zonal wind $\overline{U}^{\phi}$ going to zero at the pole.

6.2 Boundary conditions

At the ground $\frac{D}{Dt_h}(z-z_o) = 0$ where z_o is the height of the surface defined by $z_o = a P_m^n(\cos\theta)\, e^{im\phi}$, where 'a' is the amplitude of the ground topography. Thus we have the vertical velocity at the ground defined by:

$$w(z=o) = \frac{\overline{\psi}^{\phi}(o)}{R^2}\, im\, a\, P_m^n(\cos\theta)\, e^{im\phi}$$

This gives the ground topographic forcing and we have to supply the amplitude 'a' of the forcing function for the horizontal wavenumber m. From the thermodynamic equation (3.1) and the above equation we obtain:

$$\frac{dF}{dz}\left(\overline{\psi}^{\phi}(o) - \frac{i\alpha R^2}{m}\right) - \frac{d\overline{\psi}^{\phi}}{dz} F + \frac{gBa}{f}\,\overline{\psi}^{\phi}(o) = 0$$

which is used in the computer as the lower boundary condition.

One of the upper boundary conditions I have used is F=0, which implies that at this height, the perturbation of the stream function is zero. The radiational damping reduces the amplitude of the forced waves above about 20 km, when we compare them with the ground values and this is consistent with the F=0 upper boundary which means that the wave has no vertical variation at this height. Although this does not explain the meaning of the boundary condition it does demonstrate how it is, in general terms, consistent with Newtonian damping.

An alternative upper boundary is the radiation condition used by Lindzen and Kuo (1969). The equation to be solved is:

$$\frac{B}{e}\frac{d}{dz}\left(\frac{e}{B}\frac{dF}{dz}\right)(1-iG) + \frac{gBF}{f^2}\left(\frac{2\Omega}{\overline{\psi}^{\phi}} + \frac{2-n(n+1)}{R^2}\right) - \frac{B}{e\,\overline{\psi}^{\phi}}\frac{d}{dz}\left(\frac{e}{B}\frac{d\overline{\psi}^{\phi}}{dz}\right)F = 0$$

which reduces to $F'' - \nu^2 F = 0$, when we have no shear, no static stability and density stratification and no radiational damping. Since u is usually reasonably large on Mars, ν^2 is positive for n greater than or equal to 2. Thus we have the solution which satisfies $F' + \nu F = 0$ or $F = e^{-\nu z}$. If ν, the vertical wavenumber, is complex (for cases when ν^2 is negative) then $F = e^{-i\nu z}$. At this boundary one is effectively choosing the decaying solution in the model. This upper boundary condition is used to check the numerical solutions obtained for the constant wind and constant static stability, since these solutions can be determined analytically. The comparison of the accuracy of the results in given in the next section.

In regions where ν is real, the vertical propagation of energy is restricted, the amplitude decreases exponentially with height and the phase lines are vertical. With an imaginary ν, energy is propagated upwards and the phase lines tilt with height. There is some analogy between this theory and wave mechanics and a fuller discussion is given in Charney and Drazin's paper. Charney and Pedlosky (1963) discuss further the trapping of unstable planetary waves, and show that if there is a stable layer which traps the energy, above an unstable layer, there will be no vertical energy propagation in the upper layer. However in this Martian case we have a sheared wind profile which, as can be seen in equation (6.1), can produce an imaginary value for ν in the lowest few kilometres. In addition the Newtonian damping term G always produces a complex value for ν^2 and thus enables some energy to be transmitted vertically.

6.3 Comparison of numerical results with analytic solutions

Considering equation 61 with no radiational camping, no shear and no static stability stratification, we obtain the following equation:

$$\frac{1}{\rho}\frac{d}{dz}\left(\rho\frac{dF}{dz}\right) + \frac{g\beta}{f^2}\left(\frac{2\Omega}{\psi\phi} + \frac{2-n.(n+1)}{R^2}\right)F = 0$$

Solving for the decaying solution with the upper boundary conditions $\frac{dF}{dz} + i\nu F = 0$ or, with real ν $\frac{dF}{dz} + \nu F = 0$ we can compare the theoretical and numerical results. The numerical computations use the method described in Lindzen and Kuo (1969). I will give values of the amplitude F(z) at about 135 metres above the ground since these results are typical of the comparison between the two forms of the calculation. With density stratification the analytic magnitude of F(z) is 0.234, compared with 0.231 from the numerical solution of 1620 levels: without density stratification the analytic magnitude is 0.124 compared with a numerical value of 0.122. This indicates an accuracy of greater than 3% which is easily good enough for the later results.

We can also consider the convergence of the results obtained by solving the full equation. We have no analytic solutions with which to compare the numerical values but there does appear to be a good degree of convergence between the solutions as shown in the following tables. I have chosen the value of F at about 135 metres as this seemed a fairly typical result. The amplitude and phases are given for the two upper boundary conditions F=0 and the radiation condition as defined by Charney and Drazin (1961).

The amplitude results appear to be assymptotic and we have assumed that, because of the convergence to the analytic solutions, the results of the full equation are within 10% of the correct value. From 880 to 1620 levels, there is less than 5% discrepancy, and although we shall assume the results are 10% in error for the 1620 level model an error of 2 or 3% is probably a more accurate assessment.

These accuracy computations relate to a lid at thirty kilometres, with a Newtonian damping time constant of 1/5 $days^{-1}$, constant static stability and a wind profile as described in the next chapter. Increasing the Newtonian damping has very little effect on the accuracy. Similarly, as shown in Table 62, increasing the lid height from 30 to 40 km has no

TABLE 61

	No. of levels							
	220		440		880		1620	
Boundary condition F=0	0.158×10^7	*-7.91°*	0.144×10^7	*-8.36°*	0.137×10^7	*-8.5°*	0.133×10^7	*-8.65°*
Boundary condition - Radiation	0.174×10^7	*.727°*	0.158×10^7	*0.374°*	0.151×10^7	*0.21°*	0.146×10^7	*0.18°*

Values of amplitude and phase in italics of F for different numbers of levels in order to demonstrate the convergence of the numerical solutions. The amplitude has units of m^2s^{-1} and the phase is in degrees. These values correspond to an upper lid at 30 km with Newtonian damping time constant of 1/5 day^{-1} and a static stability of 1.5×10^{-5} m^{-1}

TABLE 62

	No. of levels							
	220		440		810		1620	
Boundary condition F=0	0.139×10^7	*-15.22°*	0.123×10^7	*-16.0°*	0.116×10^7	*-16.25°*	0.112×10^7	*-16.47°*
Boundary condition - Radiation	0.144×10^7	*-11.09°*	0.128×10^7	*-11.8°*	0.120×10^7	*-12.01°*	0.116×10^7	*-12.21°*

Values of amplitude and phase in italics of F, as for Table 61, but with the upper lid at 40 km and a static stability of 1.5×10^{-5} m^{-1}

effect on the convergence of the results as seen in Table 61.

6.4 Derivation of heat fluxes

Calculation of the temperature field, poleward heat fluxes and vertical energy fluxes can now be obtained directly from the knowledge of the amplitude and phase of the function F. This compares with the baroclinic model where, although we knew the vertical structure of the wave, we did not know the magnitude and hence could not calculate any fluxes.

We substituted $$\psi' = \mathrm{Re}\left\{ F(z) * H(\theta) \times e^{im\phi} \right\}$$

where $H(\theta) = P_n^m(\cos\theta)$ and can be obtained from tables. Thus using the thermal wind equation we have $$\delta\phi = \frac{f}{g}\frac{d\psi}{dz}$$

Hence

$$\delta\phi = \frac{f}{g}\,\mathrm{Re}\left\{ F'(z).H(\theta).e^{im\phi} - \cos\theta \frac{d\overline{\psi}^{\phi}}{dz} \right\} \qquad - (6.3)$$

From complex algebra we have the equation

$$\overline{\mathrm{Re}(a) \times \mathrm{Re}(b)}^{\phi} = \tfrac{1}{2}\,\overline{\mathrm{Re}\,(a \times b^*)}^{\phi}$$ where

a and b are complex functions of the perturbation of the stream function ψ'.

Thus $$\overline{v\delta\phi}^{\phi} = \tfrac{1}{2}\,\mathrm{Re}(v\delta\phi^*)$$

Since

$$v = \frac{1}{R\sin\theta}\left(\frac{\partial\overline{\psi}^{\phi}}{\partial\phi} + \frac{\partial\psi'}{\partial\phi} \right)$$

we obtain the result for the poleward heat flux, $\overline{v\delta\phi}^{\phi}$

$$\overline{v\delta\phi}^{\phi} = -\frac{1}{2}\,\mathrm{Im}\left\{ F(z).H(\theta).\frac{m}{R\sin\theta}.\delta\phi^* \right\}$$

where $(\delta\phi)^*$ is the complex conjugate of the entropy perturbation $\delta\phi$ in equation 6.3. Similarly, we can obtain a value for $\overline{w\delta\phi}^{\phi}$ which is the vertical heat flux and can be shown to be:

$$\overline{w\delta\phi}^{\phi} = \frac{1}{2}\frac{f^2}{g^2 B}\,\mathrm{Re}\left\{\left\{\frac{im\,H(\theta).F(z)}{R^2}\frac{d\bar{\psi}^{\phi}}{dz} - \frac{\bar{\psi}^{\phi}}{R^2}im\,H(\theta).F'(z) - \alpha F'(z).H(\theta)\right\}\frac{\delta\phi}{f}g^{*}\right\}$$

The vertical energy flux, $\overline{w\frac{\delta p}{\bar{\rho}}}^{\phi}$ can be calculated using $\psi' = \frac{\delta p}{\bar{\rho}\bar{F}}$ and from the thermodynamic equation

$$\overline{w\frac{\delta p}{\bar{p}}}^{\phi} = \frac{1}{2B}\,\mathrm{Re}\left\{\left\{\frac{F(z).H(\theta).f.i.m}{R^2 g}\frac{d\bar{\psi}^{\phi}}{dz} - \frac{f}{R^2 g}\bar{\psi}^{\phi}im.H(\theta).F'(z) - \frac{\alpha f}{g}F'(z).H(\theta)\right\}F^{*}(z).H(\theta)\right\}$$

Equation (6.3) produces values for the vertical entropy structure, but it is also useful to know something about the form of the temperature field. With the first law of thermodynamics we have

$$\delta\phi = \frac{\delta T}{\bar{T}} - \frac{R}{c_p}\frac{\delta p}{p_0}$$

We also have

$$g\delta\phi = \left(\frac{\partial}{\partial z} - B\right)\frac{\delta p}{\rho_0}$$

Normally the term $B\frac{\delta p}{\rho_0}$ is neglected in the Boussinesq set of equations. White (1976) has shown that in this stationary motion, the assumption that $B\,H_\rho \ll 1$, (Green 1960), does not have to be made since the vorticity equation and the lower boundary equation is the same, irrelevant of this assumption.

With $\psi = \frac{\delta p}{\rho_0}$ we have $\delta T = \frac{\bar{T}}{g}\left\{\bar{T}\frac{\partial\psi}{\partial z} + \left(\frac{g}{c_p} - \bar{T}B\right)\psi\right\}$

Thus

$$\delta T = \frac{\bar{T}}{g}\left\{T\frac{d\psi}{dz} - \frac{dT}{dz}\psi\right\} \qquad (6.4)$$

These fields will be used in the next chapter where we shall discuss the application of the theory to Mars and the information used to discuss the heat balance on the planet and the dynamics involved.

CHAPTER 7: THE RESULTS OF THE LONG-WAVE THEORY

7.0 Introduction

In this chapter, we shall consider the application of the linear theory, given in the previous chapter, to topographically forced long waves on Mars. The fourier components of the Mariner 9 topographic data, which is given in Chapter 1, are used in the lower boundary condition. Values for the static stability, Newtonian radiative damping times and the height of the upper lid have to be added in order to obtain solutions. Here we shall discuss the input parameters, the results and their implication for the Martian atmospheric circulation. The magnitudes of such parameters as static stability and wind shear are not exactly known, so the aim of this approach is only to provide fluxes and temperatures to a factor of two. In addition calculations for one latitude are assumed to be representative of the hemisphere.

7.1 An analysis of the topography

Taking the data points every 10° longitude from Figure 10, Chapter 1, and applying a standard fourier fit, we can obtain amplitudes and phases for different latitudes. These results, given in Table 71, can be seen to be consistent with the 8×8 harmonic analysis given in Chapter 1, Figure 11. Thus, as an approximation, we have generally used a value of 1 km for the amplitude (a) of the lower boundary forcing function as given in Section 6.2, Chapter 6. In addition, we have chosen a value for the horizontal wave-number m of 2 and a value of n of 3. N-m defines the number of nodes in the meridional wave, and thus for n-m of 1 the wave peaks in mid-latitudes. In most of the results we have shown, the horizontal wavenumber m of two has been used, not because we think there is any preference for this wave, but because this wave, with a forcing function amplitude of about one kilometre, could be regarded in some way typical. We have considered the latitude of about 60°N for the study since this is the region where we are also considering the heat fluxes from baroclinic eddies. This can be

TABLE 71

Latitude	Horizontal Wavenumber				
	1	2	3	4	5
60°N	0.6 km *187°*	0.6 km *151°*	0.1 km *128°*	0.3 km *190°*	0.2 km *336°*
45°N	0.4 km *234°*	1.4 km *147°*	1.0 km *152°*	0.1 km *12°*	0.4 km *348°*
30°N	1.6 km *272°*	1.9 km *110°*	1.8 km *108°*	1.2 km *267°*	0.9 km *34°*
Equator	1.3 km *311°*	3.1 km *147°*	1.5 km *68°*	0.5 km *267°*	0.7 km *165°*
30°S	2.2 km *259°*	0.4 km *284°*	2.1 km *48°*	1.1 km *69°*	0.5 km *192°*
60°S	0.5 km *236°*	0.3 km *45°*	0.4 km *32°*	0.2 km *126°*	0.3 km *225°*

Table of amplitude and phases of the fourier components for different horizontal wavenumbers and latitudes. The original data is taken at 10° longitude intervals from Figure 10, Chapter 1, which is the topographic map produced after the Mariner 9 exploration of Mars.

further justified by arguing that we only want the fluxes to a factor of two. For different latitudes, in the mid-latitude region, we find that both $\bar{\psi}^{\phi}$ and $H(\theta)$ are altered, but in fact this does not produce a factor of two variation of either the input parameters or the results. The amplitude of one kilometre for 60° North is large compared with 0.6 km found in Table 71 for wavenumber two, but hopefully this will be representative of, for example, 45° North. The phases of the topography in Table 71 are given to indicate whether the mountain ranges interfere: for example, to determine whether wavenumbers 2 and 4 at 60°N coincide.

7.2 Static stability, the wind field and the radiational damping parameters

A realistic wind shear is required for equation 61, Chapter 6. We have used the profile given below, where H_w we shall call the wind scale height. With a value of the wind scale

$$u(z) = 5.0 + 95.0\left(1 - e^{(-z/H_w)}\right) \quad ms^{-1} \qquad -(7.0)$$

height of about 10 kilometres we obtain a wind field consistent with Leovy and Briggs (1974) which was deduced from the temperature profiles using the thermal wind equation for 50° North. This produces a wind shear of about 6 $ms^{-1}\,km^{-1}$ in the first density scale height. Two further wind profiles are also used to consider, very roughly, different seasons; one uses an easterly wind, with a wind scale height of about 30 km, which is typical of the summer hemisphere, and the other using a wind scale height of 20 km, which effectively reduces the wind shear in the first density scale height to about 3 $ms^{-1}\,km^{-1}$, more typical of the spring conditions. An exponential type profile was used, not only because it is a more realistic expression of Leovy and Brigg's results, but also since equation 6.1 has a wind curvature term $\partial^2\bar{\psi}^{\phi}/\partial z^2$ which would present errors if we use a constant wind above a linear shear.

Static stabilities of 1.0 and $1.5\times10^{-5}\,m^{-1}$ are predominantly used. These values are consistent with the temperature profiles given in the

TABLE 72

	Height of the upper lid	Static Stability B	α, the inverse of the Newtonian cooling damping time	Wind Scale Height	Amplitude of the forcing function
Figure 73	20 km	$1.5 \times 10^{-5}\ m^{-1}$	$6.5 \times 10^{-5}\ s^{-1}$	10 km	1 km
Figure 74	30 km	$1.5 \times 10^{-5}\ m^{-1}$	$6.5 \times 10^{-5}\ s^{-1}$	10 km	1 km
Figure 75	40 km	$1.5 \times 10^{-5}\ m^{-1}$	$6.5 \times 10^{-5}\ s^{-1}$	10 km	1 km
Figure 76	30 km	$1.0 \times 10^{-5}\ m^{-1}$	$6.5 \times 10^{-5}\ s^{-1}$	10 km	1 km
Figure 77	40 km	$1.5 \times 10^{-5}\ m^{-1}$	$9.9 \times 10^{-5}\ s^{-1}$	10 km	1 km
Figure 78 (poleward heat flux only)	30 km	$1.5 \times 10^{-5}\ m^{-1}$	$6.5 \times 10^{-5}\ s^{-1}$	20 km	1 km
Figure 79	30 km	$1.5 \times 10^{5}\ m^{1}$	$6.5 \times 10^{5}\ s^{1}$	10 km	3 km

A list of the input parameters used for Graphs 73 to 79.

appendix, but, for greater accuracy, we shall wait until the vertical resolution of the profiles is improved. For the radiational damping term, figures consistent with Goody and Belton (1967) are used. For example, with an upper lid at 10 km, a damping time of ($\frac{1}{2}$-1) days or 0.83 or 0.42×10^5 seconds is used, and for a lid at 30 kilometres, we have a corresponding relaxation time of about 0.15×10^5 seconds.

7.3 Effect of the modified Boussinesq set of equations on the results

Equation 6.4 demonstrates that the term $T\, d\psi/dz$ is added to $-dT/dz\,\psi$ in order to calculate the temperature structure of the wave. For an isothermal atmosphere, therefore $\delta T/T = \delta\phi$. With a value of the lapse rate of $10^{\circ}K\ km^{-1}$, which is approximately five to ten times the correct value, the temperature perturbation divided by the mean atmospheric temperature $\overline{T}$, is within a factor of 3 of $\delta\phi$. A realistic temperature gradient of $1.5^{\circ}K\ km^{-1}$ produces a change in amplitude of less than 25% from the perturbation entropy field, with the phase of both fields remaining similar. Thus in the tables of results, we have generally indicated only the entropy field. The temperature perturbation δT is about $200\times\delta\phi$, where we assume $200^{\circ}K$ is the approximate value for $\overline{T}$. From the first and second laws of thermodynamics we have:

$$\frac{\delta T}{\overline{T}} = \delta\phi + \frac{R}{C_p}\frac{\delta p}{p}$$

For the unmodified set $\frac{R}{C_p}\frac{\delta p}{p}$ is often assumed to be small (Simmons 1974) compared with $\delta\phi$. However this approximation becomes even more erroneous on Mars when we have small values of p, the atmospheric pressure, and so throughout this work we have used the modified set of equations.

7.4 Results

In this section we shall consider some of the results obtained from this numerical model using typical Martian parameters. Table 72 contains a list of the input parameters used in Figures 73 to 79. These results give insight into the fluxes of heat that are associated with the

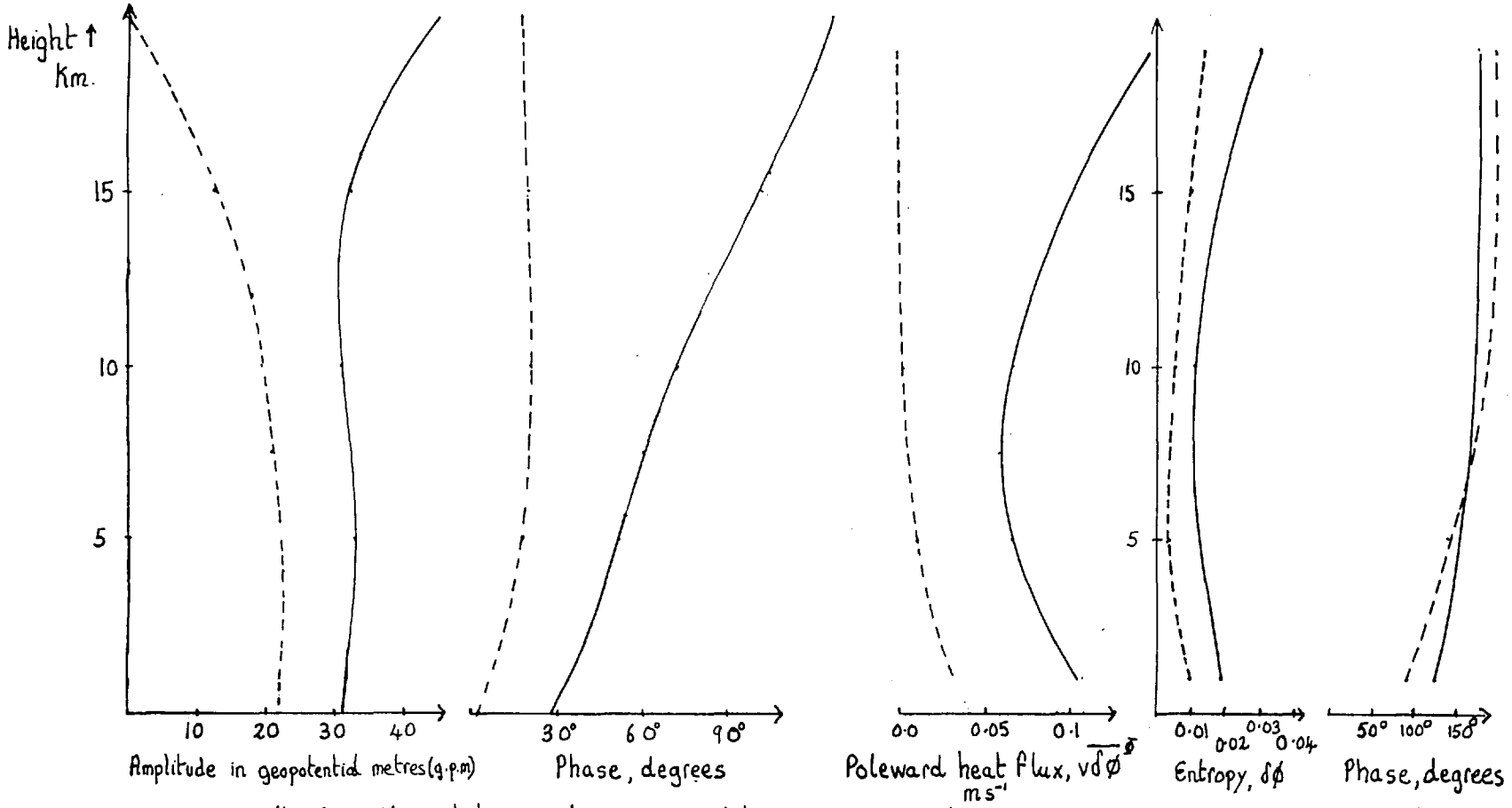

Figure 73. Results from the stationary longwave model with wavenumbers N=3, M=2, the inverse of the newtonian radiative damping time constant of $6{\cdot}5\times10^{-5}s^{-1}$, with a static stability of $1{\cdot}5\times10^{-5}m^{-1}$ and with an upper lid at 20km. The ground forcing function has an amplitude of 1km. The pecked and bold curves correspond to results with 'F=0' as the upper lid and to the radiational upper bdy. condition model (respectively)

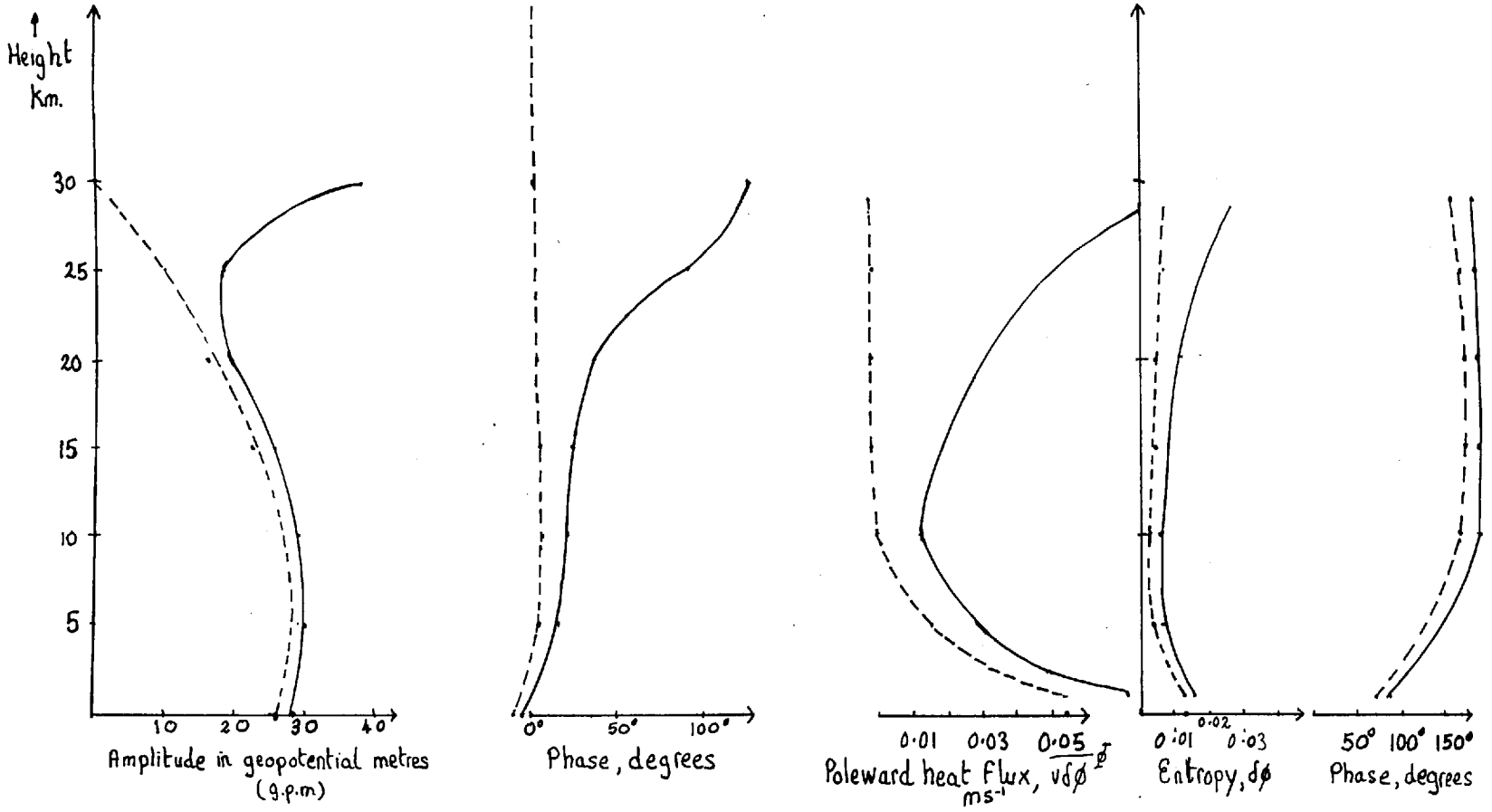

Figure 74. Same as Figure 73, except with the upper lids at 30Km.

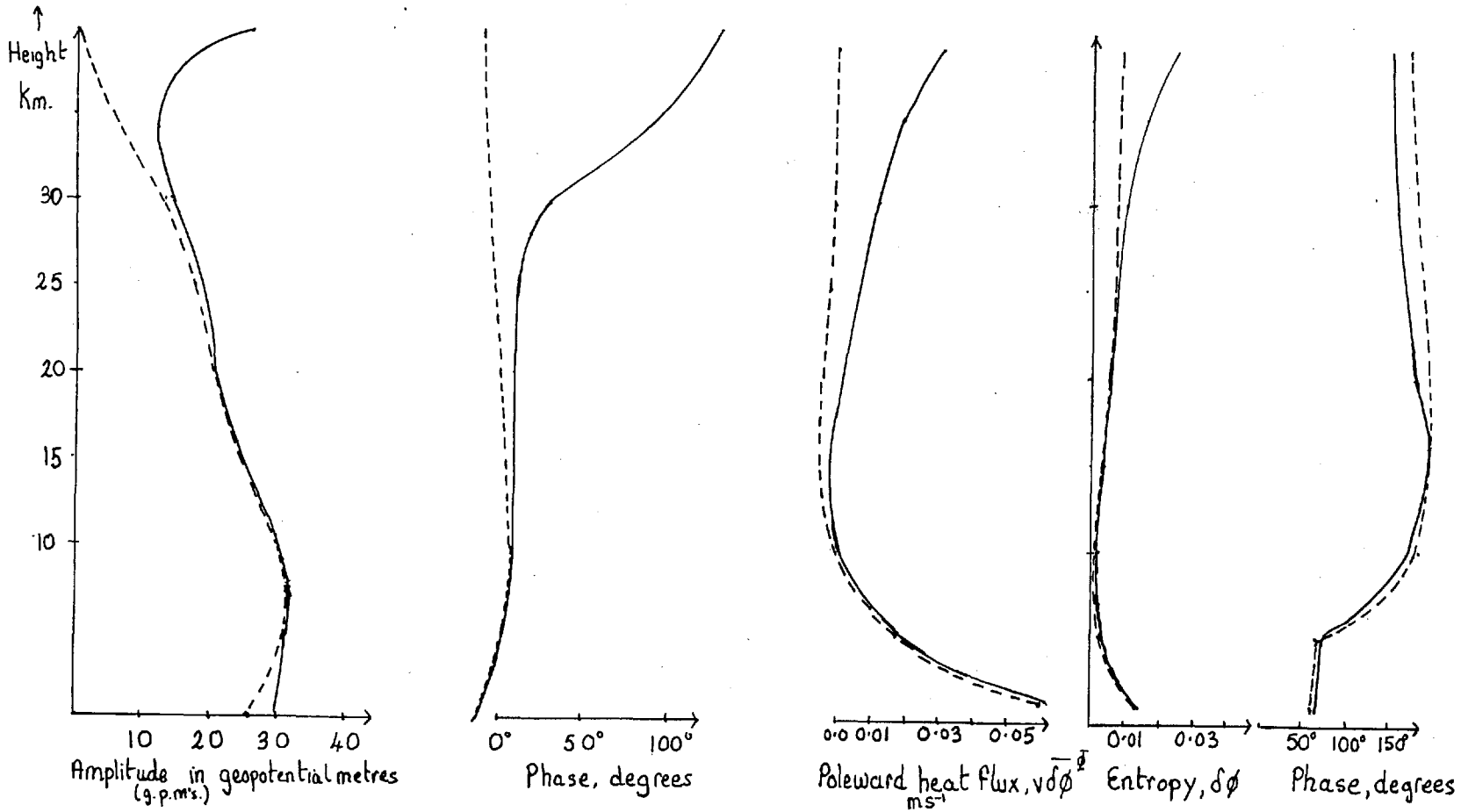

Figure 75. The same as Figure 73, except with the upper lids at 40 km.

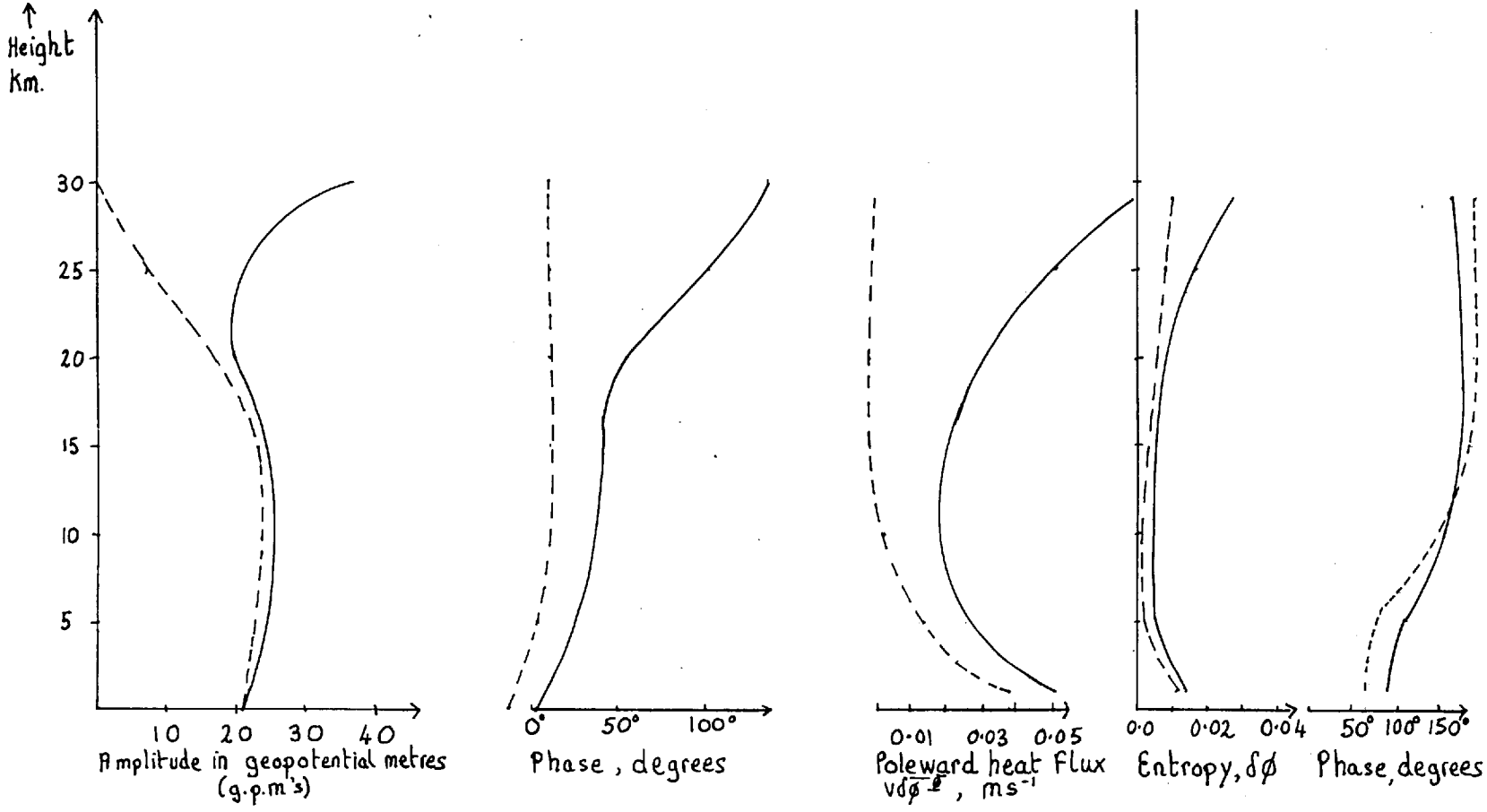

Figure 76 The same as Figure 74, except with a static stability B of $1.0 \times 10^{-5}\ m^{-1}$

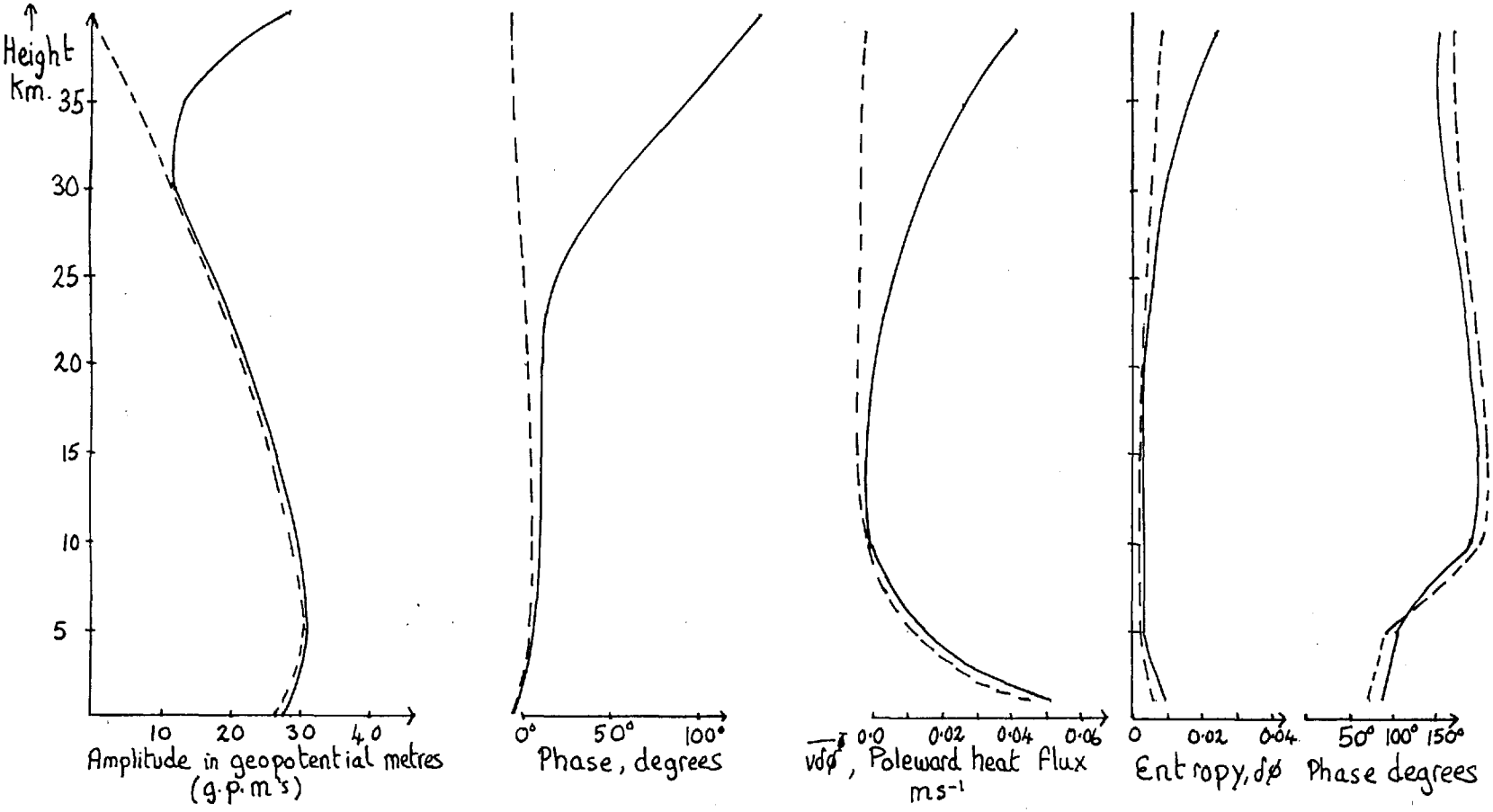

Figure 77. The same as Figure 75, except with an inverse newtonian radiative damping time constant of $9.9 \times 10^{-5} s^{-1}$.

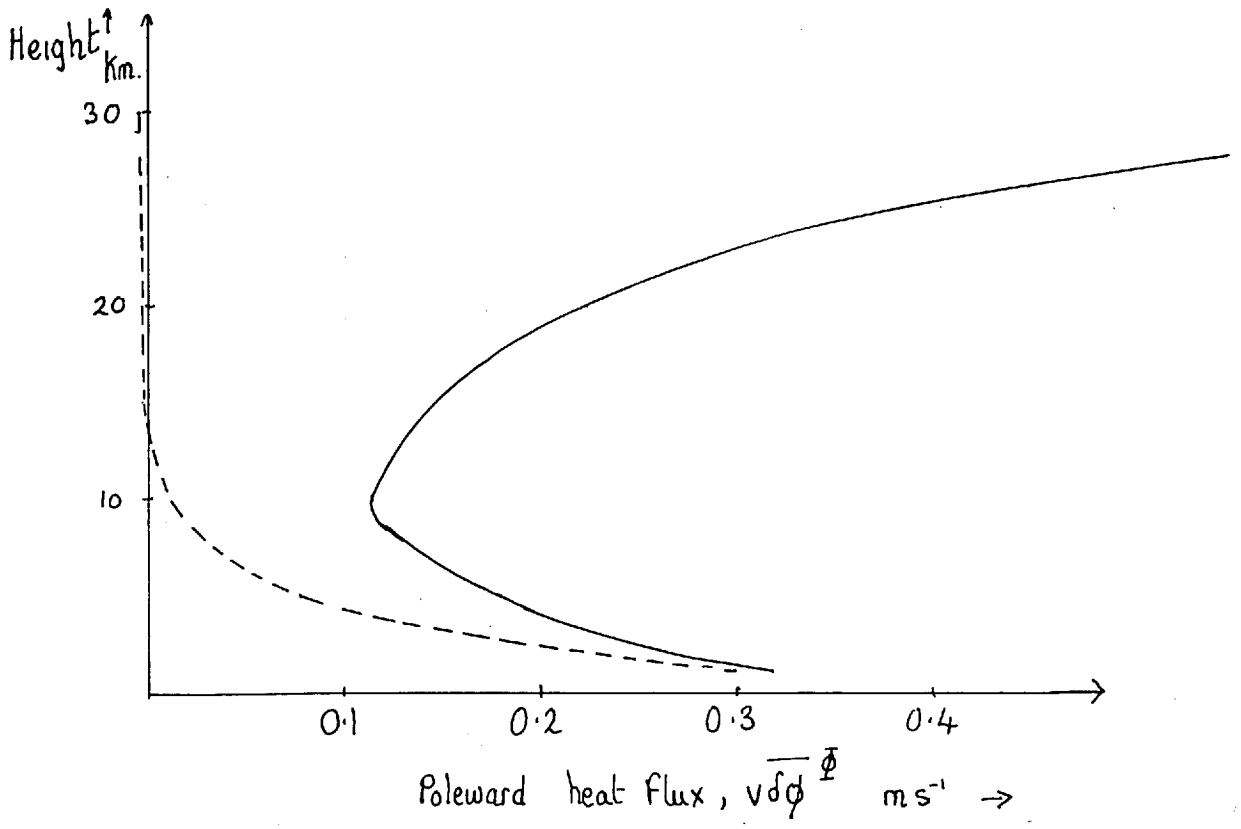

Figure 78. Vertical profile of heat fluxes with the same input data as on Figure 74, except with a wind scale height of 20km.

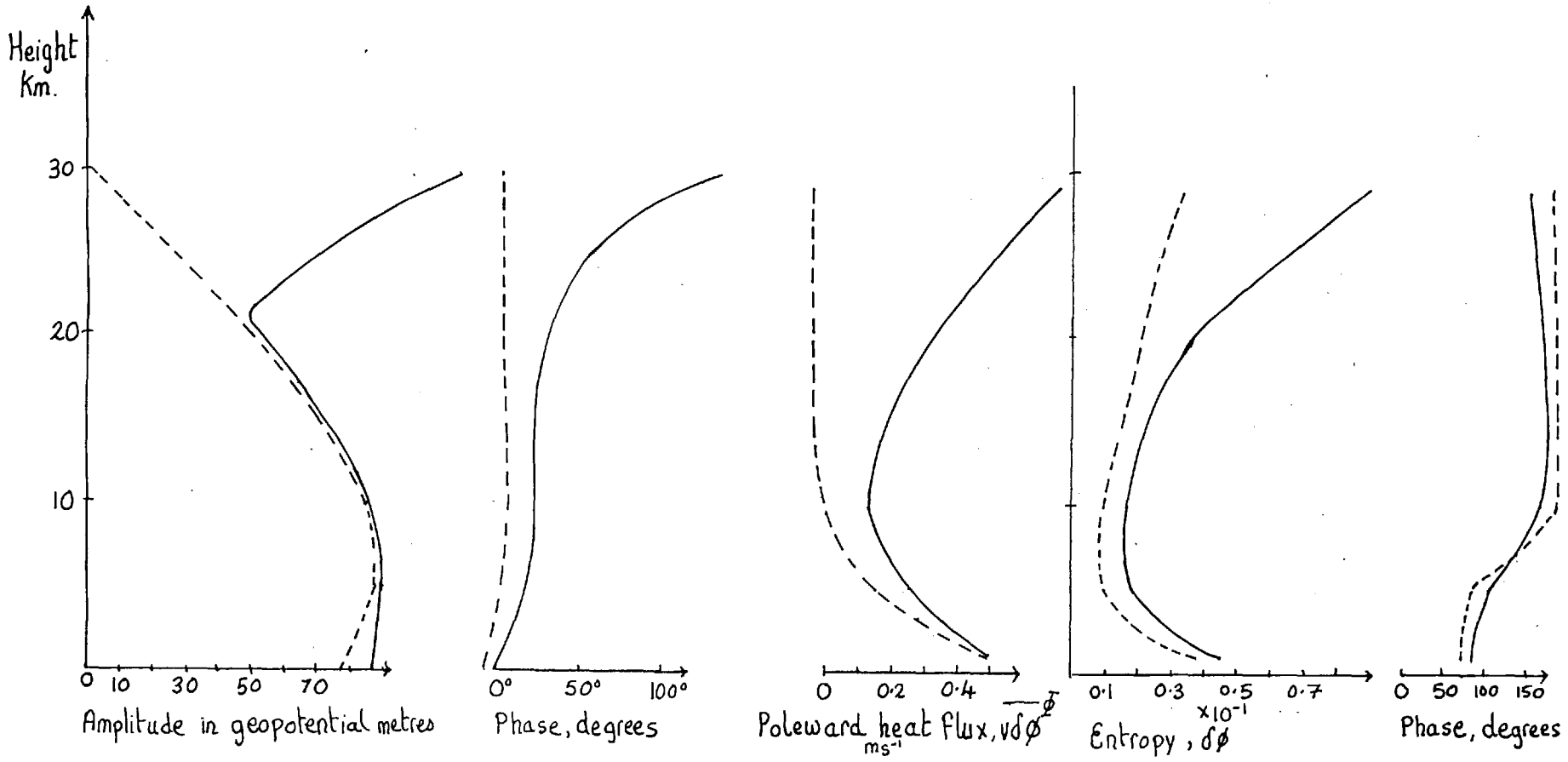

Figure 79. The same as Figure 74, except with a forcing function amplitude 'a' of 3km.

longwaves. Anomalous resutls, noticed but not understood by other researchers, are mentioned (Garcia and Geisler, 1974).

7.4.1 Varying the height of the upper lid

Graphs 73, 74 and 75 indicate the amplitude and phase of the function F with height, for the same values of static stability and Newtonian damping. The results for the poleward heat fluxes and temperature fields are also included.

The amplitudes of the waves, expressed in geopotential metres, give close agreement with the lids at 30 and 40 kilometres (Graphs 74 and 75) for the two different upper boundary conditions, providing that the comparison does not occur within 10 kilometres of the upper lid. This is especially true for the model with the radiation upper boundary. The phases show reasonable agreement, especially for the F=0 upper lid. With the lid at 20 kilometres, Graph 73, there is quite a degree of discrepancy both in amplitude and phase when compared with the Graphs 74 and 75. Thus we can conclude that, providing the upper lid is 30 kilometres or higher, the amplitude and phase of the wave is unaffected by the boundary, so long as one is not looking at the wave within 10 kilometres of the upper boundary.

With Graphs 74 and 75 there is also reasonably close agreement for the phases and amplitudes obtained for the different upper boundary conditions for each of the lid heights. Again, however, there is large disagreement for the phases and amplitudes when the lid is at 20 kilometres as in Graph 73. All the graphs show a westerly phase tilt with height in the lowest 10 kilometres, which coincides with a northwards flux of heat. On Graph 73 there is a large disagreement between the heat fluxes given by the two models, and this is probably due to the upper boundary affecting the whole fluid. Since the results given with the lid at 20 kilometres appear

anomalous, we shall not consider them as being representative of the Martian long waves; however it is interesting to note that in the bottom 12 kilometres, where the density effect ensures that the heat fluxes, $\overline{v\sigma\phi}^{\bar{\phi}}$, are important, the magnitude of these poleward heat fluxes are only a factor of 2 higher than the 30 and 40 kilometre models.

7.4.2 Varying the static stability

The effect of changing the static stability has also been considered. Graphs 74 and 76 give comparable results with static stabilities of 1.5 and $1.0\times10^{-5}\ m^{1}$. These results are similar and this indicates that the change in value of static stability effectively does not alter either the amplitude of the wave produced or the poleward heat flux.

7.4.3 Effect of Newtonian radiative damping

Increasing the radiative damping by 50% does not alter the results obtained from the model. On Graph 77, we can see that with an inverse damping time of $9.9\times10^{-5}\ s^{-1}$, there is very little difference from the results on Graph 75 with an inverse damping time of $6.5\times10^{-5}\ s^{-1}$. There is a marginal change in amplitude and phase of the function F near the upper boundary, and a slight decrease in poleward heat flux near the ground as we increase the Newtonian damping. This result has been verified with lids at other heights and, although surprising, we can deduce that the exact radiative damping need not be known in order to compute the heat fluxes in this stationary flow.

Newtonian damping, as we have formulated it, has an interesting effect on the trapping of waves. The term ν^2 in Section 6.2, Chapter 6, has now become complex and thus there will be a factor of the wave which is transmitted ($F \propto e^{(i\nu_{Re})\cdot z}$) and

a decaying solution $F \sim e^{-\nu_{Re} z}$ which traps the energy of the wave. The negative poleward heat fluxes coincide with the phase of the function F tilting eastwards with height. Garcia and Geisler (1974) found in their study of planetary waves with Newtonian cooling on a Beta plane, negative poleward heat fluxes which could not be fully explained. Garcia and Geisler use the radiational upper boundary condition only. The vertical energy flux $w\delta\rho/\rho$ is always positive from our results, except for a few models within two or three kilometres of the boundaries and so, as Garcia and Geisler have done, we shall use the poleward heat flux to consider some aspects of the attenuation of the wave.

Garcia and Geisler try to confine the occurrence of the negative poleward heat fluxes to a region where the Charney Drazin (C.D.) limit is exceeded. This limit occurs when, on increasing wind speed u,

$$\nu^2 = \frac{gB}{f^2}\left(\frac{2 - n(n+1)}{R^2} + \frac{2\Omega}{\overline{\psi}\bar{q}}\right) - \left(\frac{1}{4H_e^2}\right) \quad \text{is negative.}$$

For n=2, with typical Martian input parameters as defined earlier we have $u_c = 40\ ms^{-1}$ and for n=3 we have $u_c = 20\ ms^{-1}$. This limit ignores the effect of Newtonian radiative damping.

Dickinson (1969) considers the effect of constant Newtonian damping on the Charney-Drazin limit. By defining a new critical velocity where the decay and oscillation rates are equal, he finds that the sharp change form the evanescent to propagating solutions at the C.D. limit becomes diffuse. The region where the wave was previously purely propagating, when we add the damping, becomes primarily propagating with an evanescent component, whereas above the C.D. limit, the opposite is true: the propagating component is reduced when we increase the westerly wind speed and reduce the radiational damping.

On Graph 75, using the radiational upper boundary condition, we notice that the poleward heat flux is negative between about 10 and 18 kilometres, even though the wind is greater than 60 ms^{-1} at 10 kilometres for this n=3 wave. However their general argument by Garcia and Geisler that the negative poleward heat flux is associated with the reflected component, which interferes with the upward propagating wave, is probably correct. The larger the depth over which the wave is evanescent, the larger the amplitude of the reflected wave. Thus it is encouraging to note that we only obtain southward heat fluxes when the lid is at 40 kilometres - for the radiational upper boundary condition.

7.4.4 Different wind profiles

If we use an exponential wind profile with a wind scale height of about 20 kilometres, in equation (7.0) we are inputting parameters typical of the equinox conditions on Mars. We find that the amplitudes of the function F are twice as large and the temperature fields are similar to those in Graph 74, using otherwise the same input data. Graph 78 gives the poleward heat flux and indicates that the long-wave transport could be important in, for example, melting the polar ice caps in spring and hindering their formation in autumn. These results are produced whichever upper boundary condition is used.

With an easterly wind at the surface of 5 ms^{-1} and with an easterly shear of 2 $ms^{-1}\,km^{-1}$, corresponding to a wind scale height of 30 kilometres, we find that both the poleward heat flux is 10-20 times smaller and the temperature field is smaller by a factor of 20, than the results found on Graph 74. This would correspond to a summer situation and shows that evanescent stationary waves could be formed but they would have a very small contribution to any meridional heat flux.

7.4.5 Other modifications

Results were obtained using values for the wavenumbers of n=4 and m=3 for the input data used in Graph 74. The heat fluxes, the amplitude of the wave and the temperature fields agree to within a factor of two of the results shown on Graph 74. Thus this is a justification for our use throughout this section of wavenumbers n=3, m=2.

We also have increased the amplitude 'a' of the forcing function to 3 kilometres. The lower boundary condition is worrying since the density scale height of the atmosphere is only 12 kilometres. There is no friction and it is possible that the air, under these circumstances, might prefer to go around rather than over the mountains. Graph 79 indicates the amplitude, phase and poleward heat flux corresponding to this input data. The poleward heat fluxes are larger by a factor of eight than on Graph 74.

7.5 Concluding remarks

In this chapter we have considered and discussed orographically forced stationary long-waves on Mars. The poleward heat fluxes of this quasievanescent waves are important and could play a crucial part in reducing the size of the polar ice caps. These fluxes in winter are comparable with the poleward heat fluxes obtained from baroclinic eddy transfer theory (about 0.2 ms^{-1}). Unfortunately no attempt has been made to investigate the poleward heat fluxes produced by thermally forced longwaves, since we have no knowledge of heating functions to use.

The vertical heat fluxes $\overline{w\sigma\phi^{\phi}}$ have not so far been mentioned in this chapter. Results from the numerical solutions indicate that their magnitudes are less than 10^{-4} ms^{-1} and thus there is little effect on the vertical thermal structure of the atmosphere. For this reason we have not discussed them in this thesis.

In terms of heating the atmosphere poleward of say 60° latitude

in the northern hemisphere, the magnitude of the heating rate can be calculated using all the poleward heat fluxes. We can conclude that the effective heating rate in the lowest 10 kilometres of the atmosphere is approximately 2-3^{o}K/day from data on Graph 74, or in the winter hemisphere, approximately 15^{o}K/day from data on Graph 78, or in the spring hemisphere, and about 20^{o}K/day for the data with a forcing amplitude of 3 km, Graph 79. The poleward heat flux will be generally larger than the heat flux produced by one stationary wave component since at any one time there will be more than one wave. Thus these waves are responsible for heating the polar regions by many degrees a day.

CHAPTER 8: SUMMARY

In this thesis we have tried to provide a general synopsis of some of the dynamical and radiative properties in the winter hemisphere of the Martian atmosphere. In Chapter 2 we have produced a Martian tephigram, assuming that the atmosphere is composed of carbon dioxide, with a little water vapour. With the temperature profiles given in the appendix and with the water vapour content of the atmosphere giving a saturated mixing ratio of 10^{-3}, we can deduce from the tephigram that all the profiles are stable and that the lee waves consist of water ice. Thus from the Mariner 9 data it appears that both wet and dry vertical convection is unlikely to occur: this I suspect is a fallacy, especially at the equator and is due to the inaccurate temperature profiles. With a much smaller temperature discontinuity at the ground convection would be likely but, for a more complete analysis, we shall have to wait for the Viking 1976 results.

The photographs, Figures 31-35, indicate wave-like motions in the winter hemisphere, which we have shown are consistent with the belief that they are baroclinic eddies. The observed phase speeds are about 10 ms^{-1}, whereas our Beta plane theory predicts generally about 12-15 ms^{-1}. However the large mountains and basins probably have an important effect on the growth rates, phase speeds and wavelengths of these eddies. Further work needs to be done on the growth of these eddies in large basins as on Mars, since it is unknown whether the air would prefer to go over or around these mountain ranges. Newtonian radiative damping noticeably reduces the growth rates, but only makes a minor modification to the phase speeds of the cyclones. The wavelength of the predicted disturbances agrees well with the values observed on the photographs.

The dynamics of stationary long waves has also been considered and found to be very important. The large fourier components of the surface terrain are 5-10 times greater on Mars than on the earth, and directly force

the stationary longwaves. The computation of the poleward heat fluxes has been made in spherical polar co-ordinates. The Newtonian damping has been parameterised, as in the baroclinic theory, and shown that it is crucial when considering long waves, although the exact damping time constant need not be exactly known. These waves were neglected in Leovy and Mintz's (1969) numerical model and this caused the size of the polar ice cap to be largely overestimated. We calculate that these poleward heat fluxes, with spring type wind profiles are at least comparable with and probably greater than the baroclinic fluxes, which have been crudely estimated (probably over-estimated) by means of Green's (1970) transfer theory. The combination of several stationary long waves is likely to increase this poleward heat flux. If all the heat passing north across the 60° North latitude circle were used to heat the first density scale height of the atmosphere of that polar region, we have calculated that the heating rate would be about 10°K per day.

On the earth thermal forcing has been found to be important in the production of stationary long waves and thus this is likely to be important on Mars. Although we can postulate that the mountains have a constant surface temperature (Sagan, 1968) we have at present no idea of the vertical heating function.

In conclusion it is apparent that the carbon dioxide radiational damping plays an important role in our understanding of the circulation of the atmosphere of Mars. Unless large quantities of dust absorbing the solar radiation are found in the atmosphere we find that we cannot explain the differences between the observed and the theoretical radiative equilibrium temperature profiles. When more measurements are made the answers to this and the many other questions posed in this thesis will be known.

REFERENCES

Charney, J. and Drazin, P.	1961	'Propagation of planetary-scale disturbances from the lower into upper atmosphere', J.Geophys.Res., 66, pp.88-109.
Charney, J. and Pedlosky, J.	1963	'On the trapping of unstable planetary waves in the atmosphere', J.Geophys.Res., 68, 24, pp.6441/2.
Christensen, E.	1975	'Martian topography derived from occultation, radar spectral and optical measurements', J.Geophys.Res., 80, 20, pp.2909/13.
Cutts, J.	1973	'Nature and origin of layered deposits of the Martian polar regions', J.Geophys.Res., 18, 20, pp.4231-49.
Dickinson, R.	1969	'Vertical propagation of planetary Rossby waves through an atmosphere with Newtonian cooling', J.Geophys.Res., 74, 4, pp.929/38.
Garcia, R. and Geisler, J.	1974	'Vertical structure of stationary planetary waves in the presence of altitude dependent zonal winds and dissipation', 79, 36, p.5613.
Gierasch, P. and Goody, R.	1968	'A study of the thermal and dynamical structure of the Martian lower atmosphere', Planetary and Space Physics, pp.615/46.
Gierasch, P. and Goody, R.	1972	'The effect of dust on the temperature of the Martian atmosphere', J.Atmos.Sci., 29, pp.400/2.
Gierasch, P. and Sagan, C.	1971	'A preliminary assessment of the Martian wind regimes', Icarus, 14, pp.312/8.
Goody, R. and Belton, M.	1967	'Radiative relaxation times for Mars', Planetary and Space Science, 15, pp.247-56.
Goody, R. and Gierasch, P.	1967	'Radiation in the Martian atmosphere', Planetary and Space Science, 15, pp.1465/77.
Green, J.S.A.	1960	'A problem in baroclinic instability', Q.J.Roy.Met.Soc., 86, pp.237/51.
Green, J.S.A.	1970	'Transfer properties of the large scale eddies and the general circulation of the atmosphere', Q.J.Roy.Met.Soc., 96, pp.157/85.
Hanel, R. et.al.	1972	'The Martian Environment', Icarus, 17, pp.423/39.
Hide, R.	1976	'Motions in planetary atmospheres', Q.J.Roy.Met.Soc., 102, pp.1/23.
Kane, I.	1973	'A numerical investigation in the stability of zonal flows in the atmosphere', Ph.D. thesis, University of London.

Ksanfomalitee,	1974	'Mars 5 - surface and atmosphere of the red planet', Zemlya-I-Vasalennaya, Part 5, pp.7/11.
Kuo, N.	1952	'3 dimensional disturbances in a baroclinic current', J.Met., pp.260/78.
Leovy, C. and Briggs, G.	1974	'Mariner 9 observations of the Mars north polar hood', Bull.Amer.Met.Soc., 55, pp. 278/97.
Leovy, C. and Mintz, Y.	1969	'Numerical simulation of the atmospheric circulation of Mars', J.At.Sci., 26, pp.1167/90.
Lindzen, R. and Kuo, N.	1969	'A reliable method for the numerical integration of a large class of ordinary and partial differential equations', Mon.Wea.Rev., 97, pp.732/4.
N.A.S.A.	1972	'The face of Mars'.
National Bureau of Standards	1955	U.S. circ. 564, p.105, p.161.
Pedlosky, J.	1964	'Stability currents in the atmosphere and ocean', J.At.Sci., 21, pp.201/19.
Pirraglia, J.	1975	'Martian atmospheric lee waves', Goddard Space Flight Center, X-622-75 123.
Pirraglia, J. and Conrath, B.	1974	'Martian tidal pressure and wind fields obtained from Mariner 9 I.R. spectroscopy expt', J.Atm.Sci., 31, pp.318/29.
Runcorn, S.	1973	'On the implications of the shape of Mars', Icarus, 18, pp.109-12.
Sagan, C.	1968	'Elevation differences on Mars', J.Geophys.Res., 73, 4, pp.1373/89.
Sagan, C. and Pollack, J.	1969	'Wind blown dust on Mars', Nature 223, pp.791/4.
Saltzman, B.	1968	'Axially symmetric climate variables', Pure and Applied Geophys., 69, p.247.
Scorer, R. and Wilkinson, M.	1956	'Waves in the lee of an isolated hill', Q.J.Roy.Met.Soc., 82, pp.419/27.
Simmons, A.	1974	'Planetary-scale disturbances', Q.J.Roy. Met.Soc., 100, pp.76/108.
Soderblom, L. et.al.	1973	'Mariner 9 observations of the surface of Mars in the north polar region', J.Geophys. Res., 78, 20, p.4202.
Stone, P.	1972	'A simplified radiative-dynamical model for the static stability of rotating atmospheres', J.At.Sci., 29, pp.405/17.

White, A.A. 1976 'Modified quasi Boussinesq equations using geometric height as a vertical co-ordinate', Q.J.Roy.Met.Soc., in press.

Wilkinson, J.H. 1965 'The algebraic eigenvalue problem', Chapter 8, Clarendon Press.

ACKNOWLEDGEMENTS

The author wishes to thank all members of the Atmospheric Physics Group for encouragement and guidance throughout the years. He also wishes to express his sincere thanks to Jan Wilkinson for typing the thesis.

APPENDIX

Introduction

This section contains temperature profiles obtained by Mariner 9 infra-red measurements. The subsolar latitude is approximately 6° South except where shown. The aim of this selection is to give a general idea of the temperatures obtained on Mars. This is not a consistent set, since although the measurements were taken after the dust storm, they are a collection over a period of several weeks. Thus, for example, the hourly results obtained for latitude 60° South do not represent the progression of the temperature profiles through one day from 7.00 to 13.00 hours. Although we have not used these summer hemisphere temperature profiles, I have enclosed them for completeness.

The temperatures are produced by analysis of the amplitude of the 14/15 micron emission band of carbon dioxide. For different parts of the band, the transmission function has a different vertical form, and thus we can obtain the vertical structure of the temperature pattern. The results, although accurate measurements, are means over more than half a density scale height and thus are not a correct representation of temperature against height. The presence of a superadiabatic layer, for example on latitude 40° South, 9.0 Martian local time, page A12, cannot be determined and instead there is a surface temperature discontinuity of about 7°K.

A brief summary of the temperature profiles

The index on page A3 provides a list of the profiles taken from latitude 60° South to 60° North, at hourly intervals wherever possible. At 40°, 50°, 60° North, in early spring we have profiles that are predominantly isothermal, or sometimes colder near the ground than all the levels above. These later results are probably caused by cold air advection in the first scale height. With no solar radiation reaching the ground, because of the north polar cloud canopy, these results can be understood

(Leovy and Briggs 1974). Nearer the equator and in the summer hemisphere the profiles become less stable, although there is no evidence of any unstable lapse rates. This seems a little dubious, however because of the large inputs of solar radiation and the equator. The corrected results are computed for high surface temperatures, linearly interpolating the temperatures from the 1-2 mb. region. This was designed by the N.A.S.A. scientists to overcome the problem of having a temperature discontinuity at the ground. However for more accurate results we will have to wait for the results from the Viking mission.

INDEX FOR THE TEMPERATURE PROFILES

Latitude	Martian Local Time	Page No.
$60^{o}N$	14hrs, 15hrs, 16hrs	A4
$50^{o}N$	15hrs, 16hrs	A5
$40^{o}N$	15hrs, 16hrs	A5
$30^{o}N$	16hrs	A6
$20^{o}N$	15hrs, 16hrs	A6
$10^{o}N$	15hrs, 16hrs	A7
Equator	7hrs, 13hrs, 14hrs, 15hrs	A8
$10^{o}S$	7hrs, 13hrs, 15hrs,	A9
$20^{o}S$	8hrs, 12hrs, 14hrs	A10
$30^{o}S$	8hrs, 12hrs, 13hrs, 14hrs	A11
$40^{o}S$	7hrs, 8hrs, 9hrs, 13hrs	A12
$40^{o}S/50^{o}S$	14hrs	A13
$50^{o}S$	7hrs, 8hrs, 10hrs, 11hrs	A14
$60^{o}S$	7hrs, 8hrs, 9hrs, 10hrs	A15
$60^{o}S$	11hrs, 12hrs, 13hrs	A16

60° North

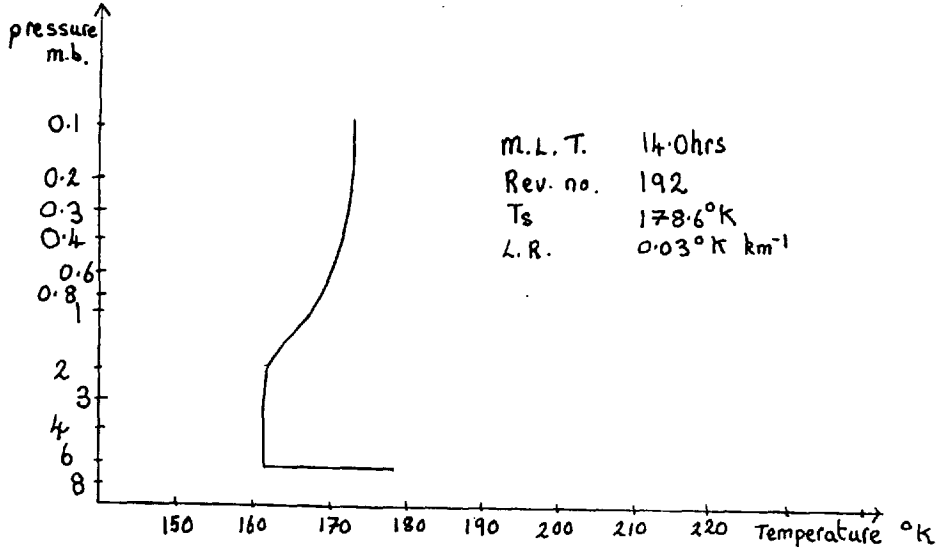

M.L.T. 14·0hrs
Rev. no. 192
T_s 178·6°K
L.R. 0·03°K km^{-1}

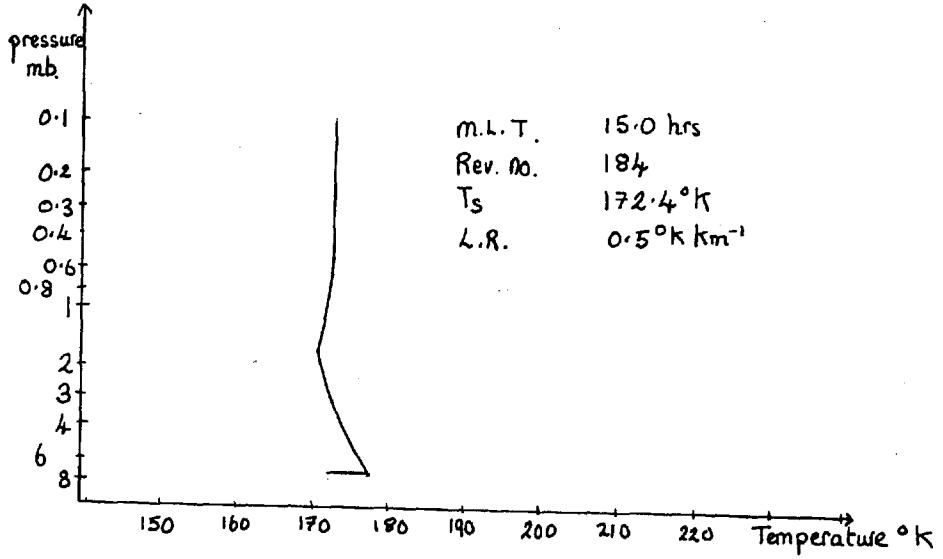

M.L.T. 15·0 hrs
Rev. no. 184
T_s 172·4°K
L.R. 0·5°K km^{-1}

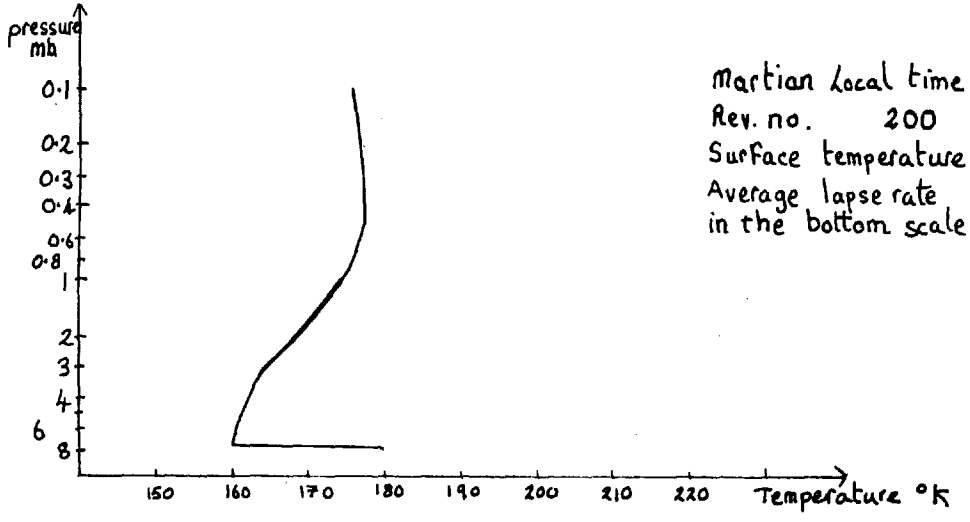

Martian Local time (M.L.T.) 16·0hrs.
Rev. no. 200
Surface temperature (T_s.) 180·7°K
Average lapse rate in the bottom scale ht (L.R.) −0·6°K km^{-1}

50° North

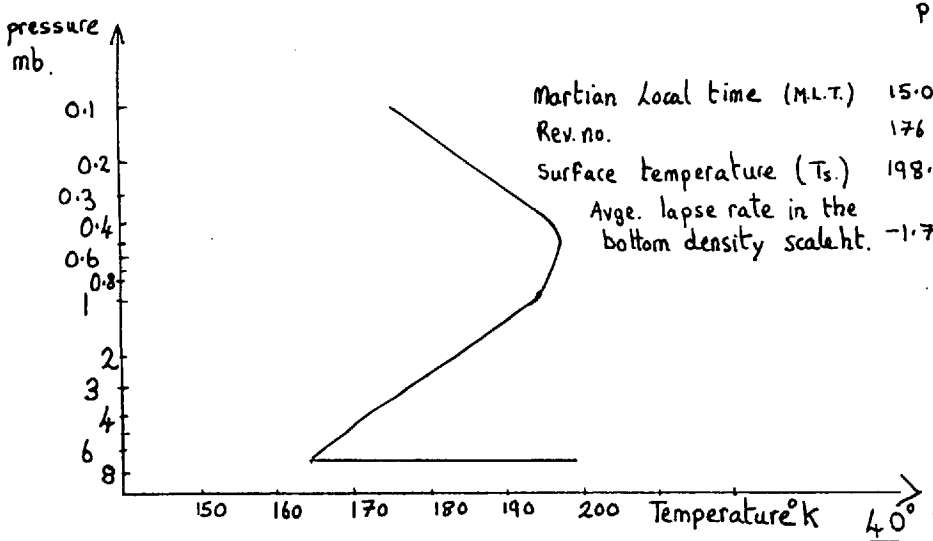

Martian Local time (M.L.T.) 15·0 hrs
Rev. no. 176
Surface temperature (T_s) 198·6° K
Avge. lapse rate in the bottom density scale ht. $-1·7°K\ km^{-1}$

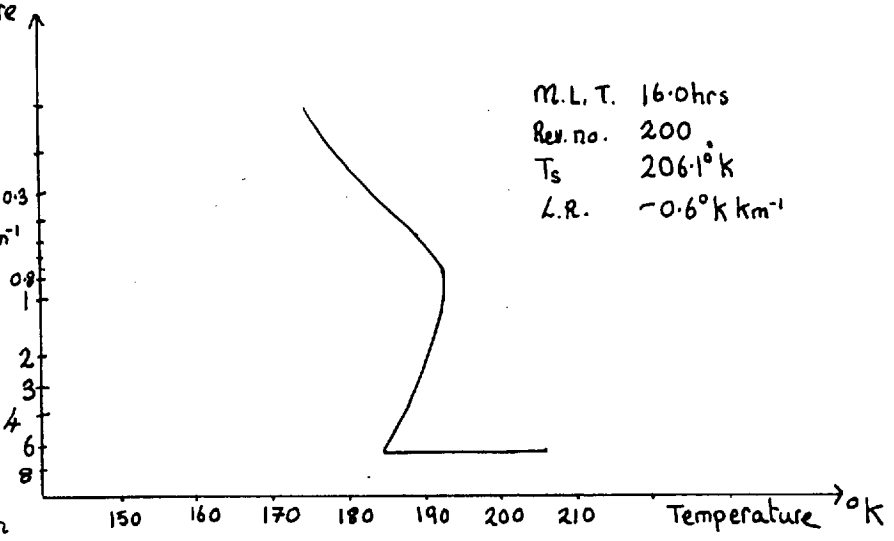

M.L.T. 16·0 hrs
Rev. no. 200
T_s 206·1° K
L.R. $-0·6°K\ km^{-1}$

40° North

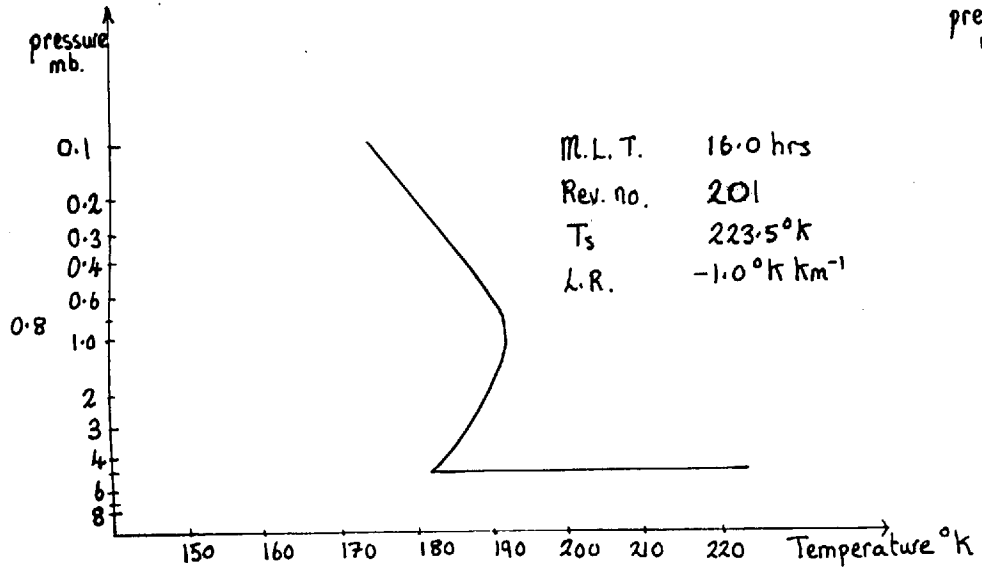

M.L.T. 16·0 hrs
Rev. no. 201
T_s 223·5° K
L.R. $-1·0°K\ km^{-1}$

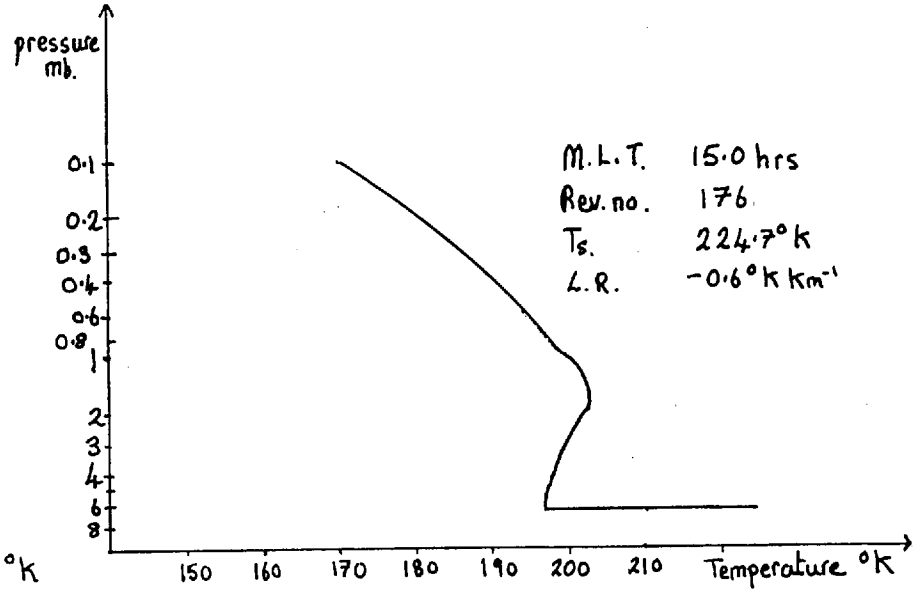

M.L.T. 15·0 hrs
Rev. no. 176
T_s 224·7° K
L.R. $-0·6°K\ km^{-1}$

30° North

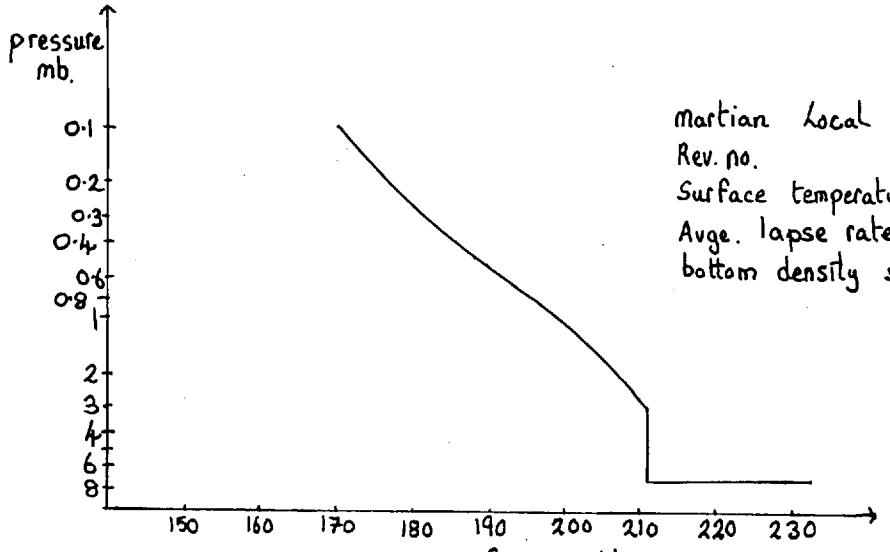

Martian Local time (M.L.T.) ~16·0 hrs
Rev. no. ~200
Surface temperature (T_s) ~232·4°K
Avge. lapse rate in the bottom density scale ht. (L.R.) ~ 0·05°K km^{-1}

20° North

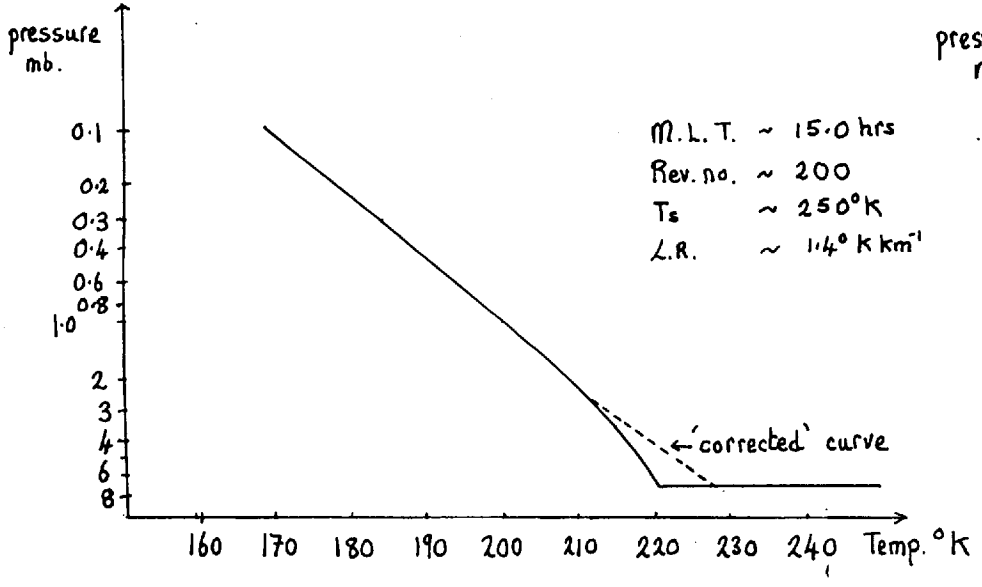

M.L.T. ~ 15·0 hrs
Rev. no. ~ 200
T_s ~ 250°K
L.R. ~ 1·4° K km^{-1}

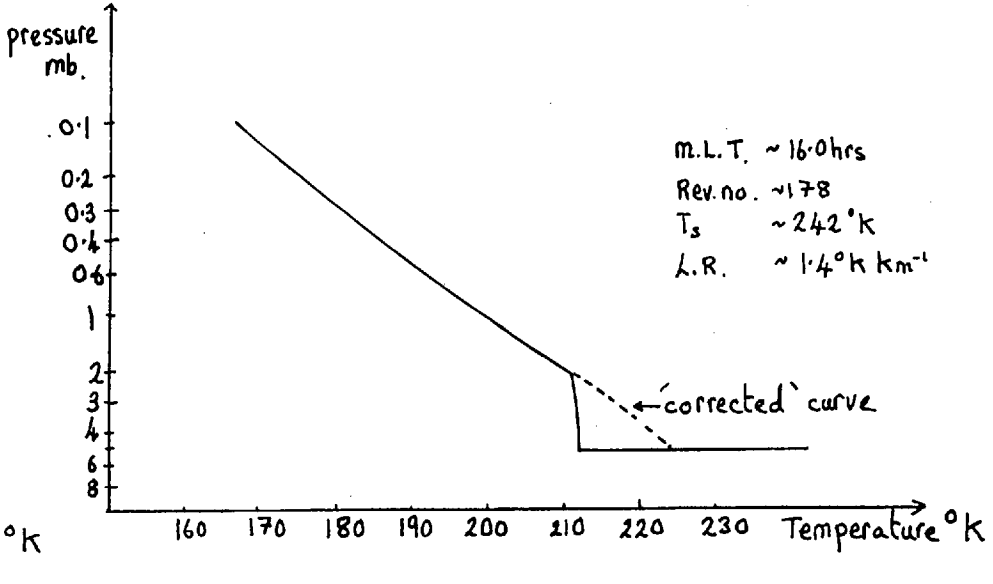

M.L.T. ~ 16·0 hrs
Rev. no. ~178
T_s ~ 242°K
L.R. ~ 1·4° K km^{-1}

10° North

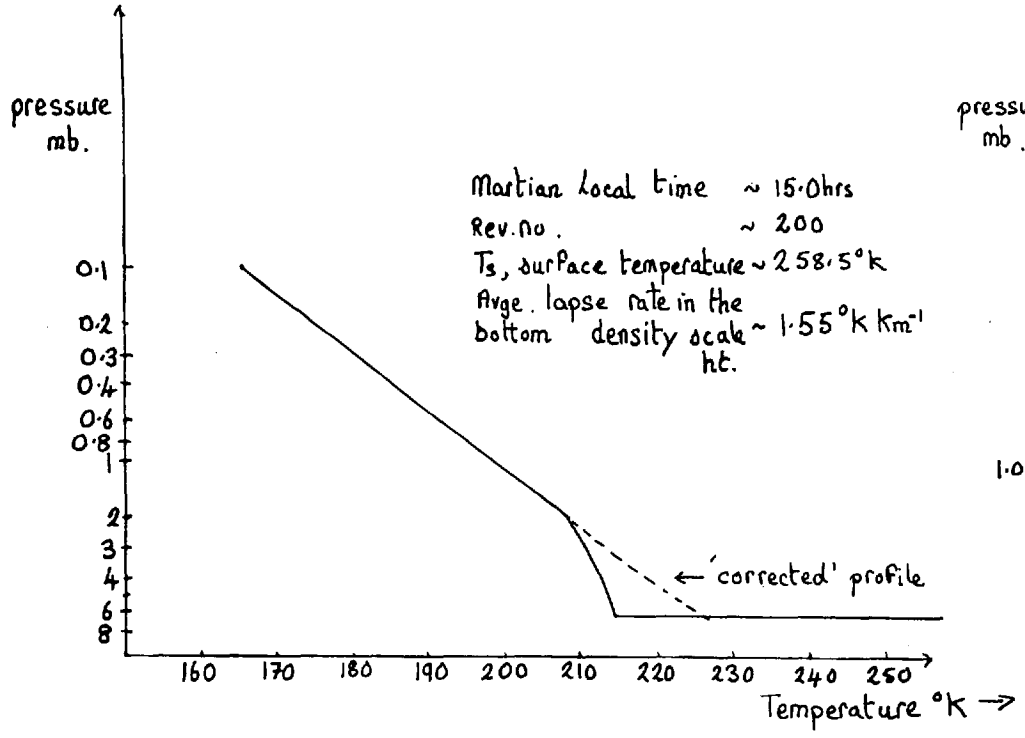
pressure mb.
0·1
0·2
0·3
0·4
0·6
0·8
1
2
3
4
6
8
160
170
180
190
200
210
220
230
240
250
Temperature °K →
Martian local time ~ 15·0hrs
Rev. no. ~ 200
Ts, surface temperature ~ 258·5°K
Avge. lapse rate in the bottom density scale ht. ~ 1·55°K km⁻¹
← 'corrected' profile

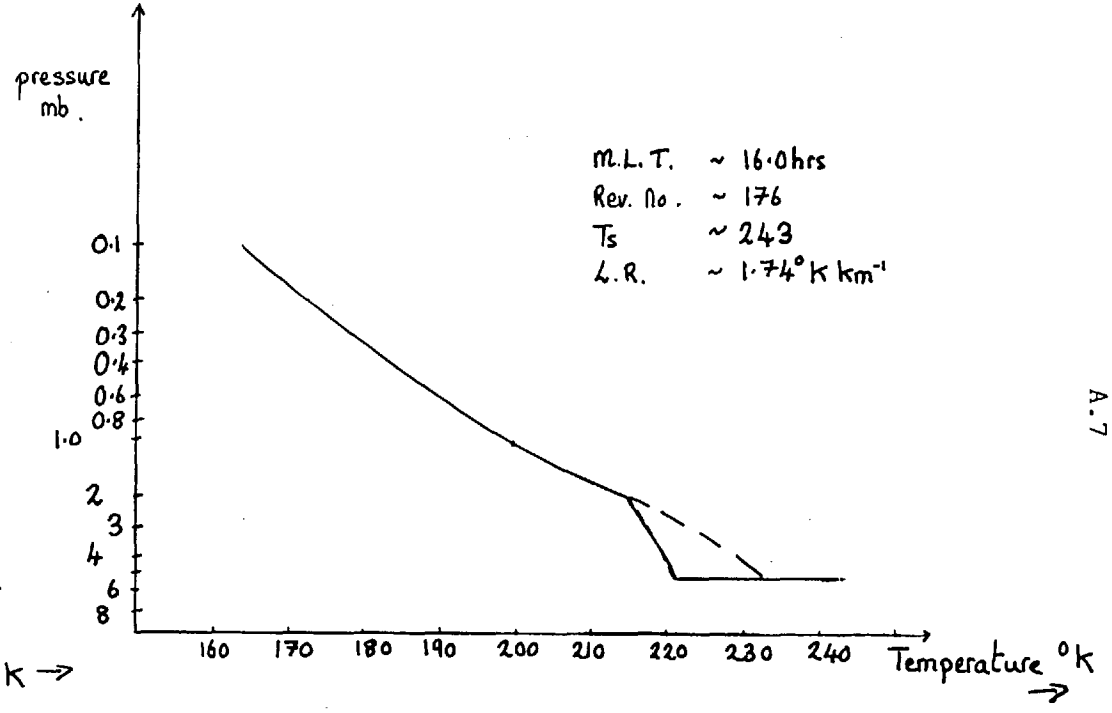
pressure mb.
0·1
0·2
0·3
0·4
0·6
0·8
1·0
2
3
4
6
8
160
170
180
190
200
210
220
230
240
Temperature °K →
M.L.T. ~ 16·0hrs
Rev. No. ~ 176
Ts ~ 243
L.R. ~ 1·74° K km⁻¹

Equator

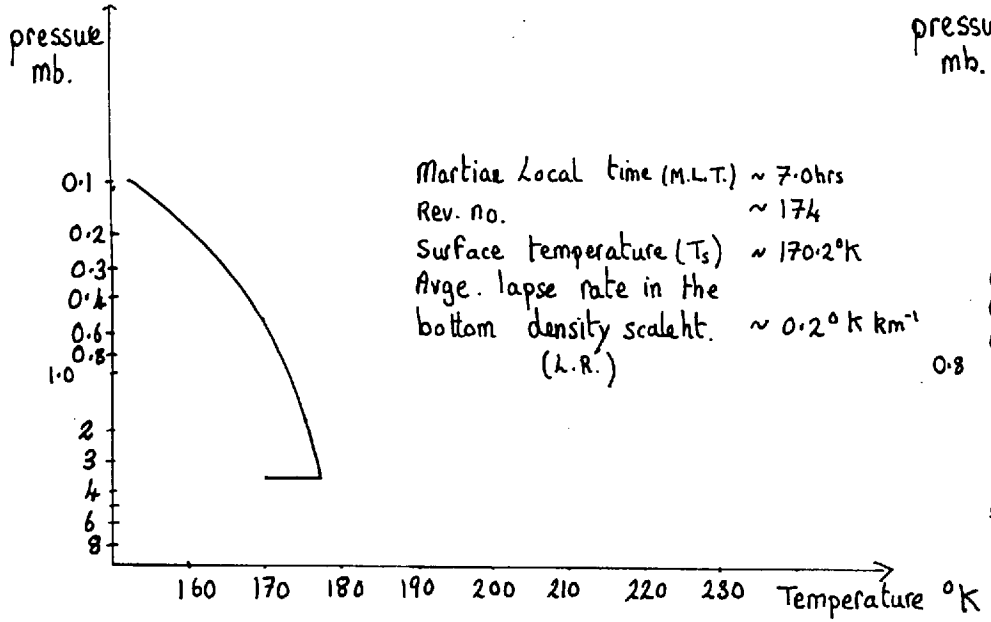

Martian Local time (M.L.T.) ~ 7·0 hrs
Rev. no. ~ 174
Surface temperature (T_s) ~ 170·2°K
Avge. lapse rate in the bottom density scale ht. (L.R.) ~ 0·2° K km^{-1}

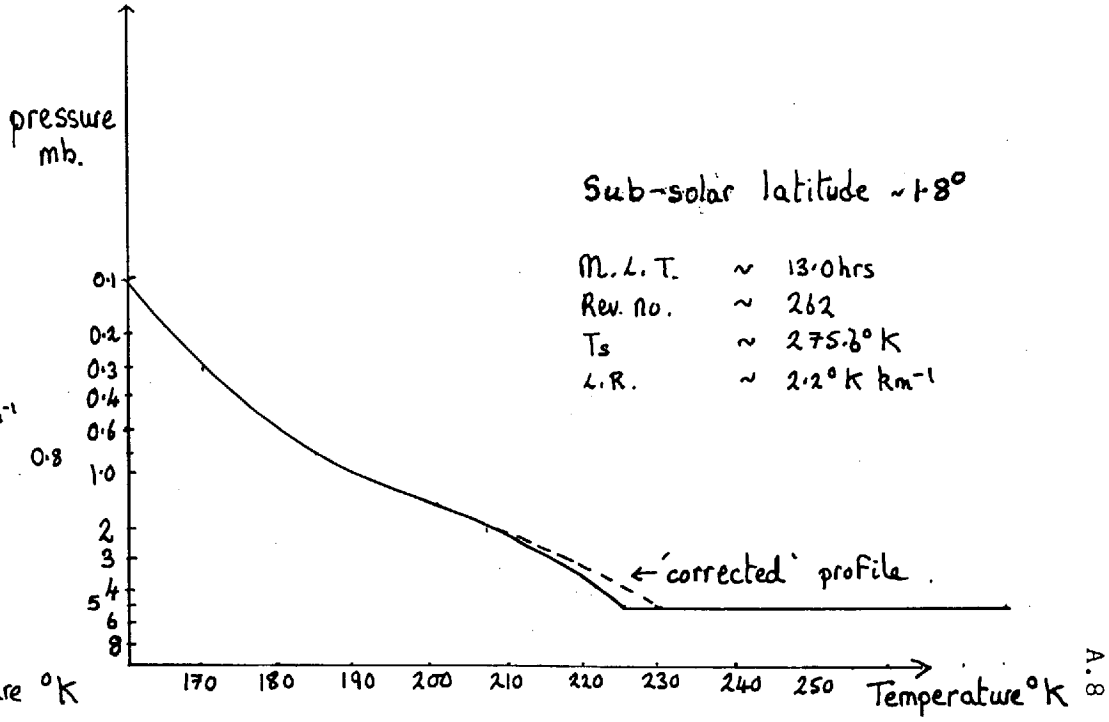

Sub-solar latitude ~ 1·8°

M.L.T. ~ 13·0 hrs
Rev. no. ~ 262
T_s ~ 275·6° K
L.R. ~ 2·2° K km^{-1}

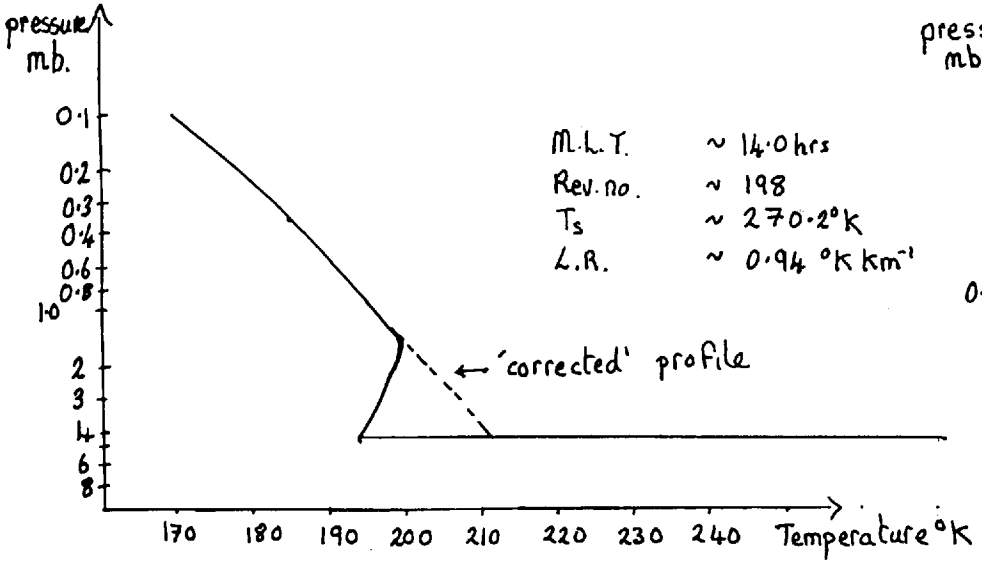

M.L.T. ~ 14·0 hrs
Rev. no. ~ 198
T_s ~ 270·2°K
L.R. ~ 0·94 °K km^{-1}

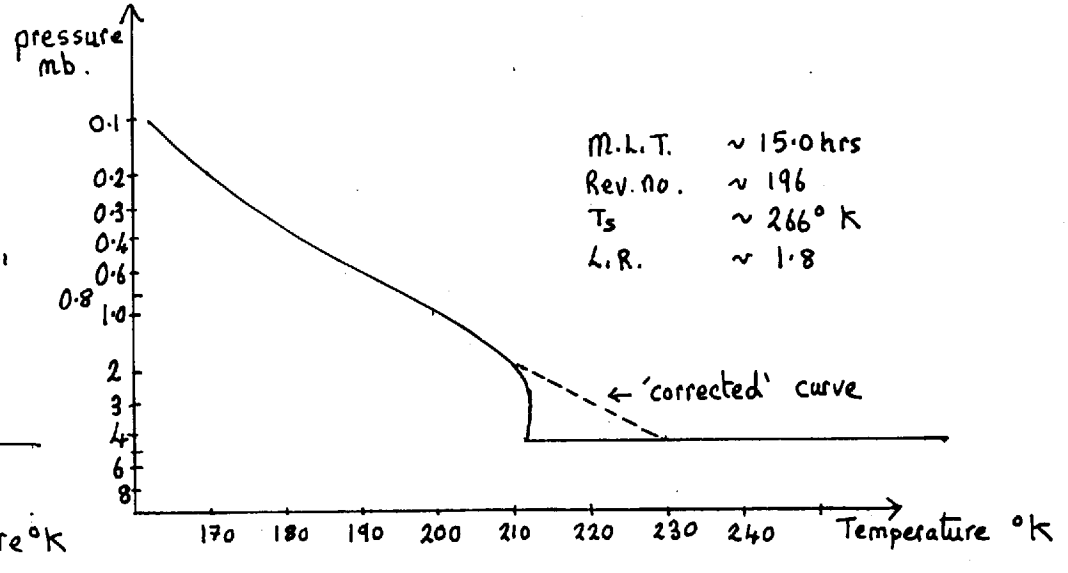

M.L.T. ~ 15·0 hrs
Rev. no. ~ 196
T_s ~ 266° K
L.R. ~ 1·8

10° South

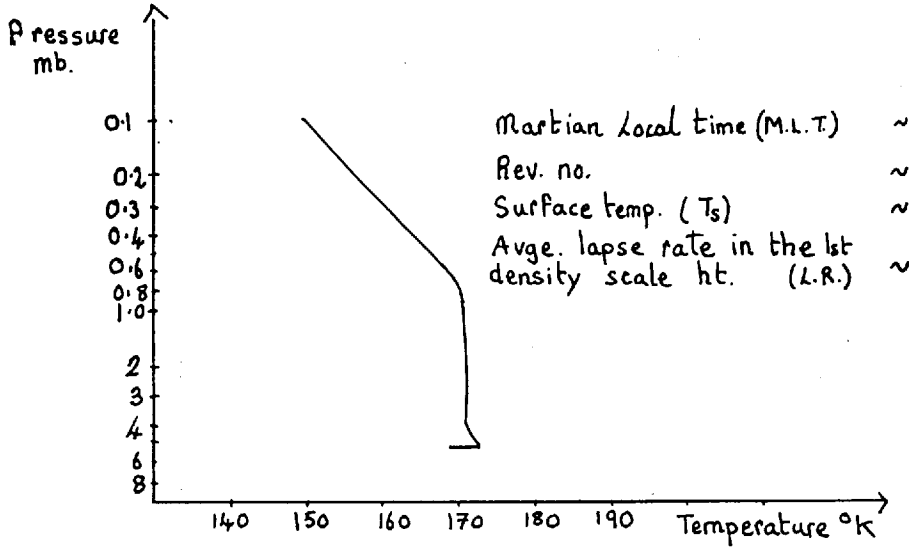

Martian Local time (M.L.T.) ~ 7·0 hrs.
Rev. no. ~ 190
Surface temp. (T_s) ~ 169°K
Avge. lapse rate in the lst density scale ht. (L.R.) ~ 0·18°K Km^{-1}

Subsolar latitude ~ 1·8° N.

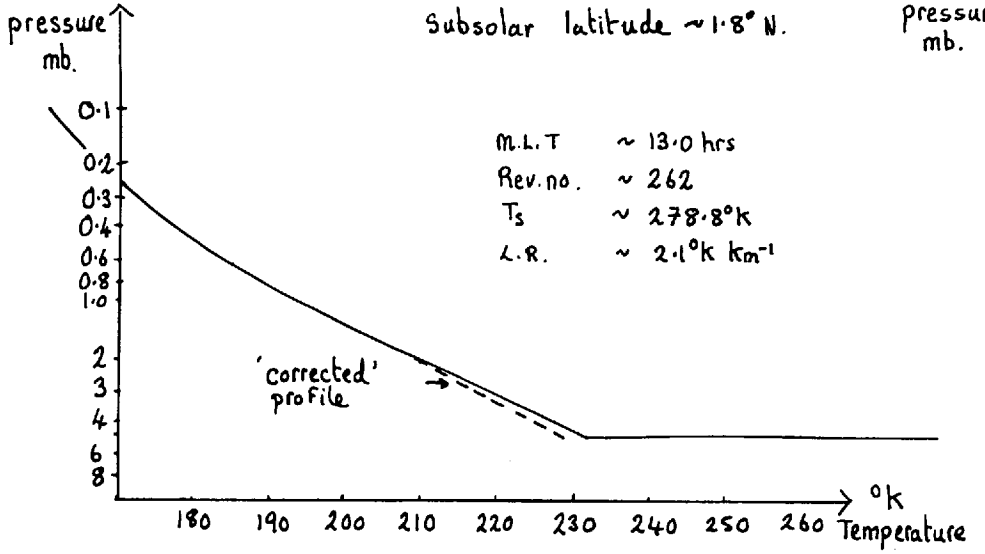

M.L.T ~ 13·0 hrs
Rev.no. ~ 262
T_s ~ 278·8°K
L.R. ~ 2·1°K km^{-1}

M.L.T. ~ 15·0 hrs
Rev.no. ~ 176
T_s ~ 267·9°K
L.R. ~ 1·2°K/km^{+1}

20° South

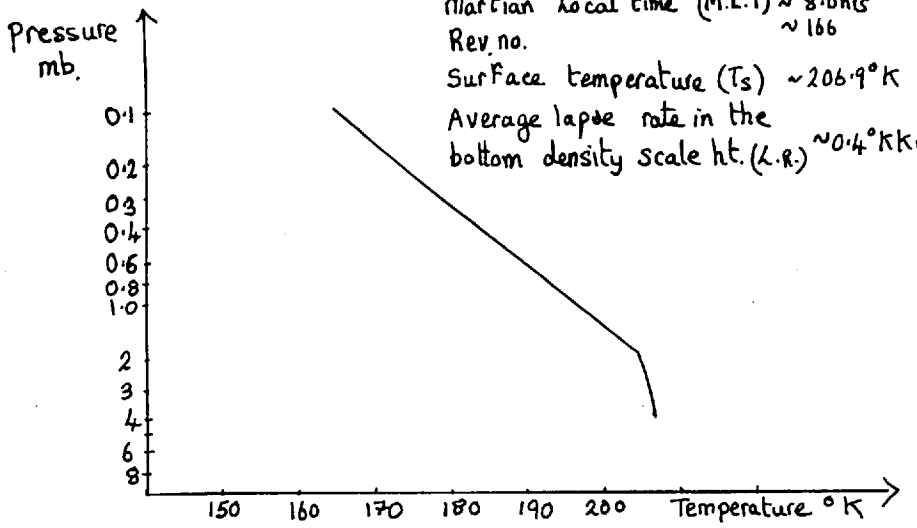

Martian local time (M.L.T) ~ 8·0hrs
Rev. no. ~ 166
Surface temperature (T_s) ~ 206·9°K
Average lapse rate in the bottom density scale ht. (L.R.) ~ 0·4°K km^{-1}

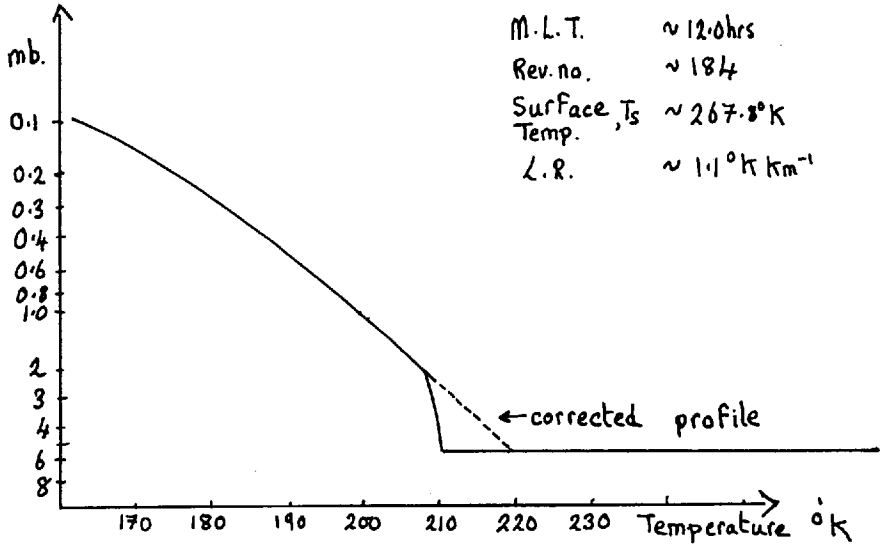

M.L.T. ~ 12·0hrs
Rev. no. ~ 184
Surface Temp., T_s ~ 267·8°K
L.R. ~ 1·1°K km^{-1}

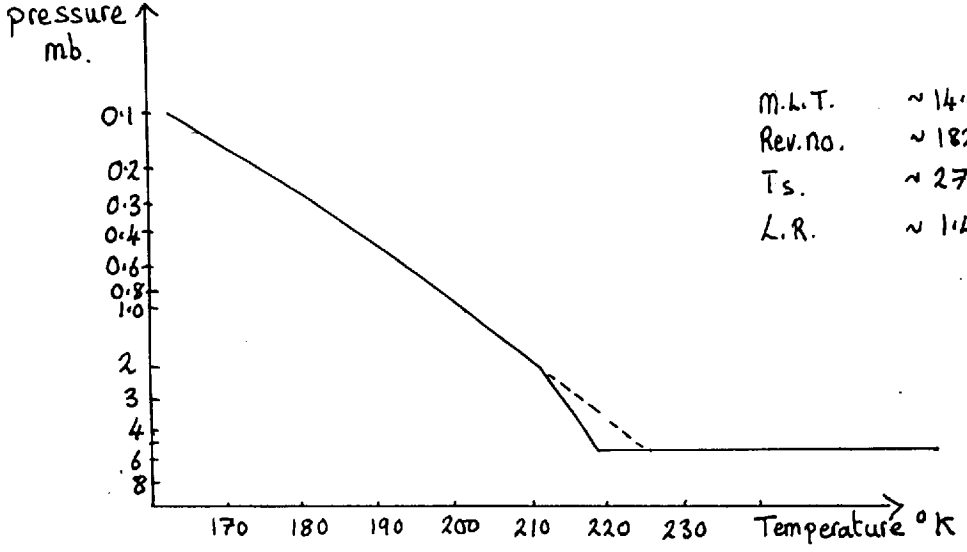

M.L.T. ~ 14·0hrs
Rev. no. ~ 182
T_s. ~ 273·1°K
L.R. ~ 1·4°K km^{-1}

30° South

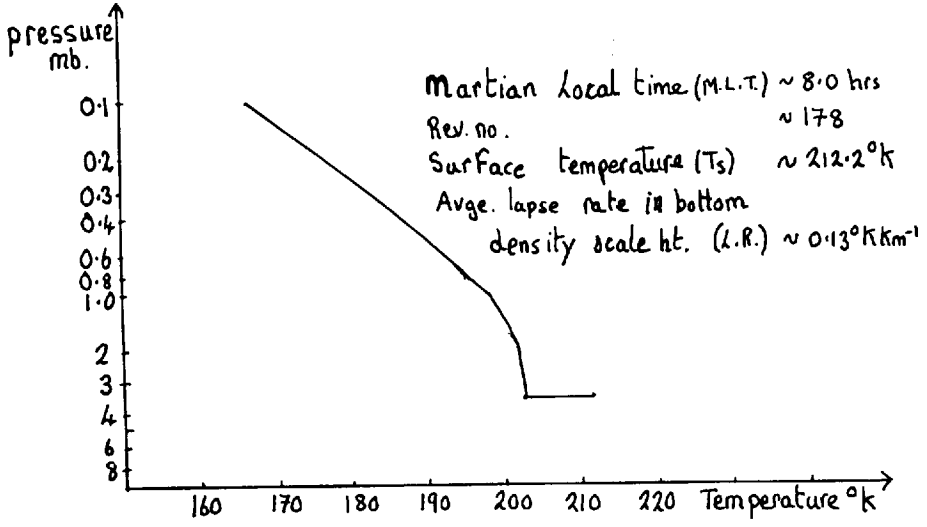
pressure mb.
0·1
0·2
0·3
0·4
0·6
0·8
1·0
2
3
4
6
8
160 170 180 190 200 210 220 Temperature °K
Martian local time (M.L.T.) ~ 8·0 hrs
Rev. no. ~ 178
Surface temperature (T_s) ~ 212·2°K
Avge. lapse rate in bottom density scale ht. (L.R.) ~ 0·13°K km⁻¹

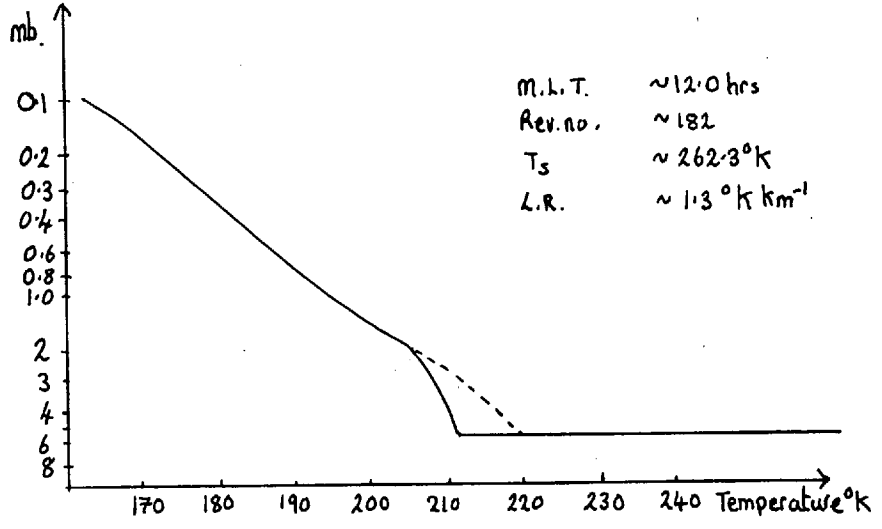
mb.
0·1
0·2
0·3
0·4
0·6
0·8
1·0
2
3
4
6
8
170 180 190 200 210 220 230 240 Temperature °K
M.L.T. ~12·0 hrs
Rev. no. ~ 182
T_s ~ 262·3°K
L.R. ~ 1·3 °K km⁻¹

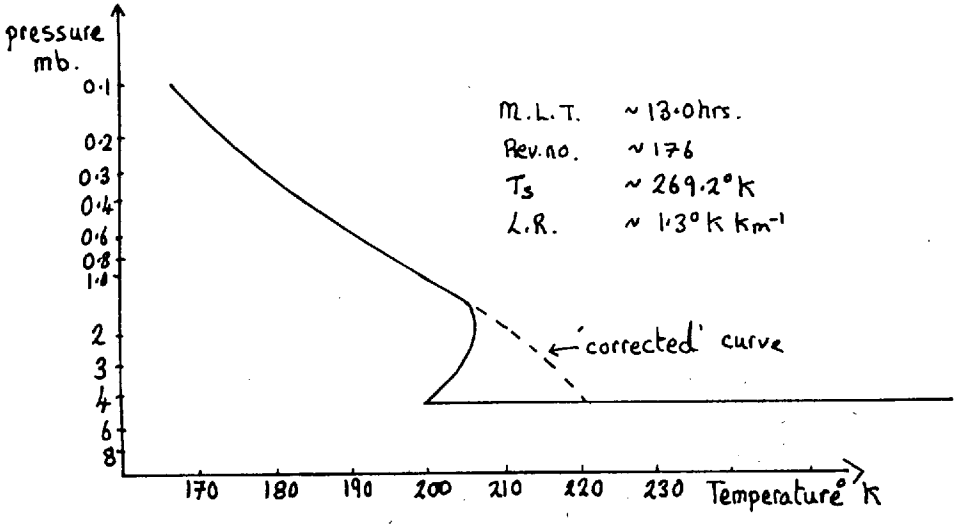
pressure mb.
0·1
0·2
0·3
0·4
0·6
0·8
1·0
2
3
4
6
8
170 180 190 200 210 220 230 Temperature °K
M.L.T. ~ 13·0 hrs.
Rev. no. ~ 176
T_s ~ 269·2°K
L.R. ~ 1·3° K km⁻¹
'corrected' curve

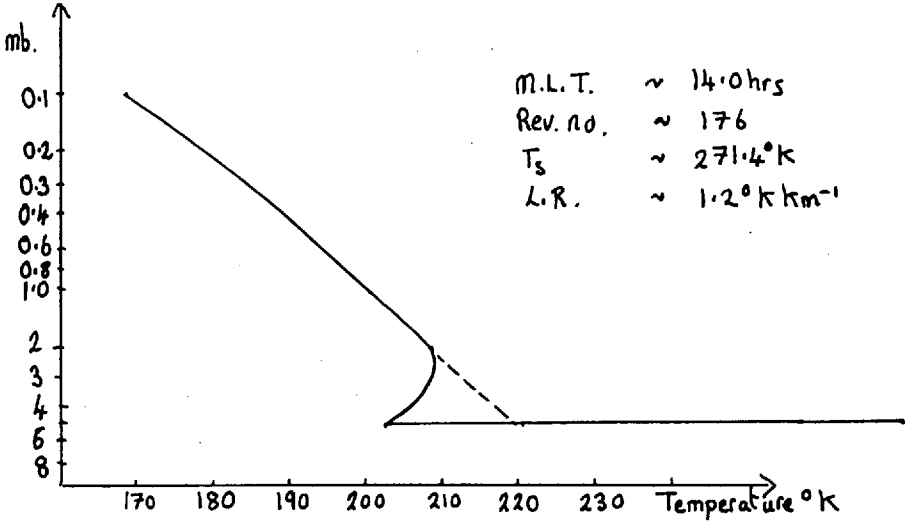
mb.
0·1
0·2
0·3
0·4
0·6
0·8
1·0
2
3
4
6
8
170 180 190 200 210 220 230 Temperature °K
M.L.T. ~ 14·0 hrs
Rev. no. ~ 176
T_s ~ 271·4°K
L.R. ~ 1·2° K km⁻¹

40° South

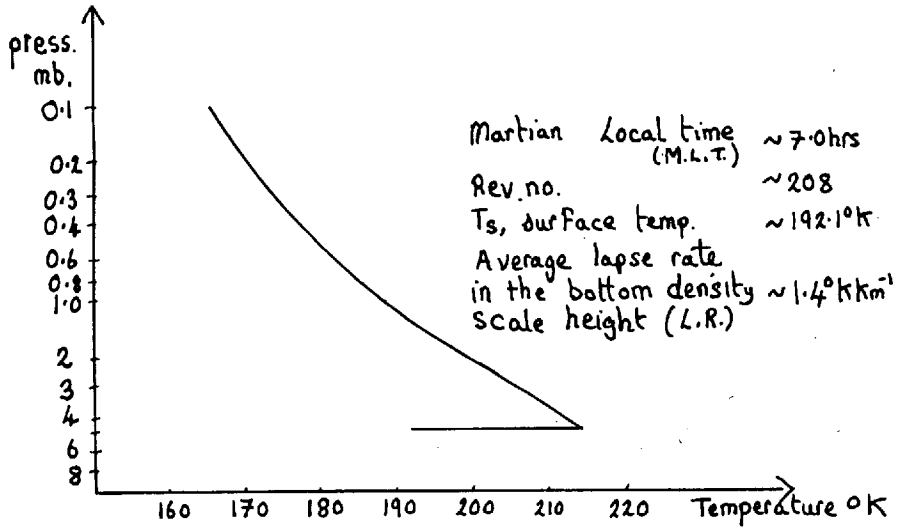

Martian Local time (M.L.T.) ~7·0hrs
Rev. no. ~208
T_s, surface temp. ~192·1°K
Average lapse rate in the bottom density scale height (L.R.) ~1·4°K km^{-1}

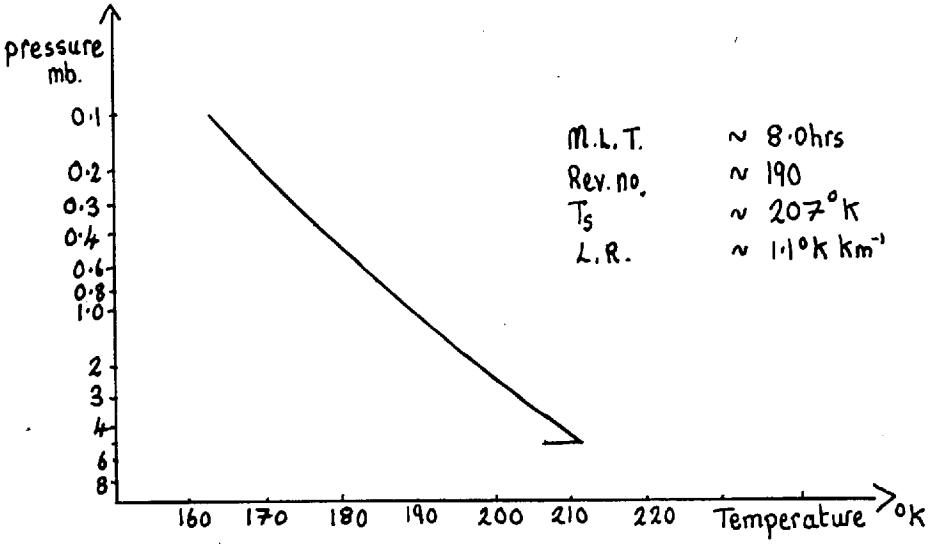

M.L.T. ~8·0hrs
Rev. no. ~190
T_s ~207°K
L.R. ~1·1°K km^{-1}

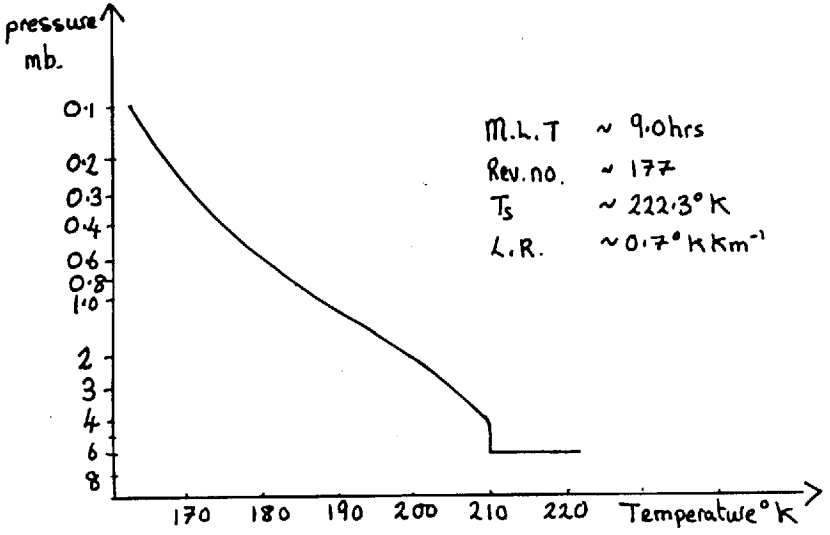

M.L.T ~9·0hrs
Rev. no. ~177
T_s ~222·3°K
L.R. ~0·7°K km^{-1}

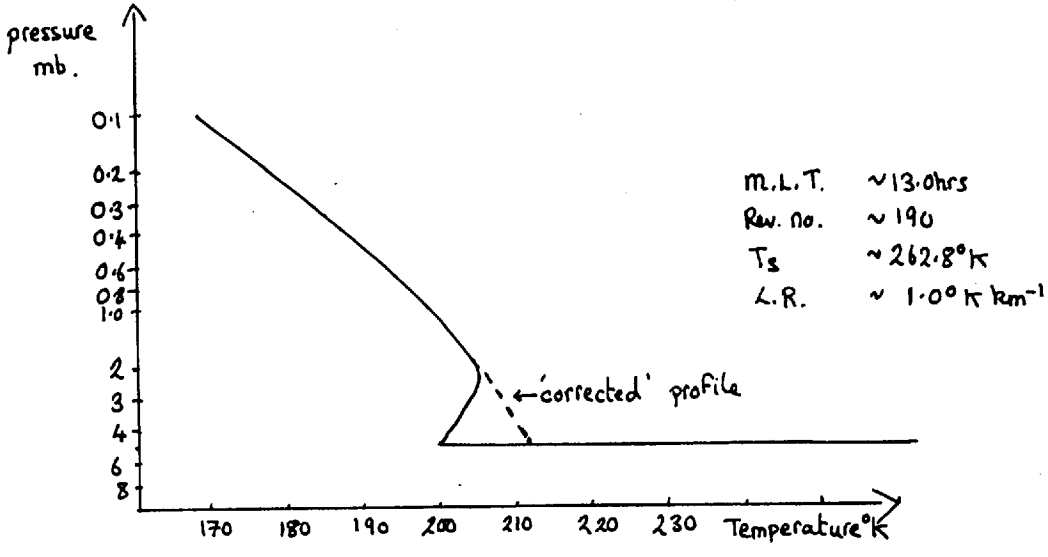

M.L.T. ~13·0hrs
Rev. no. ~190
T_s ~262·8°K
L.R. ~1·0°K km^{-1}

40° South

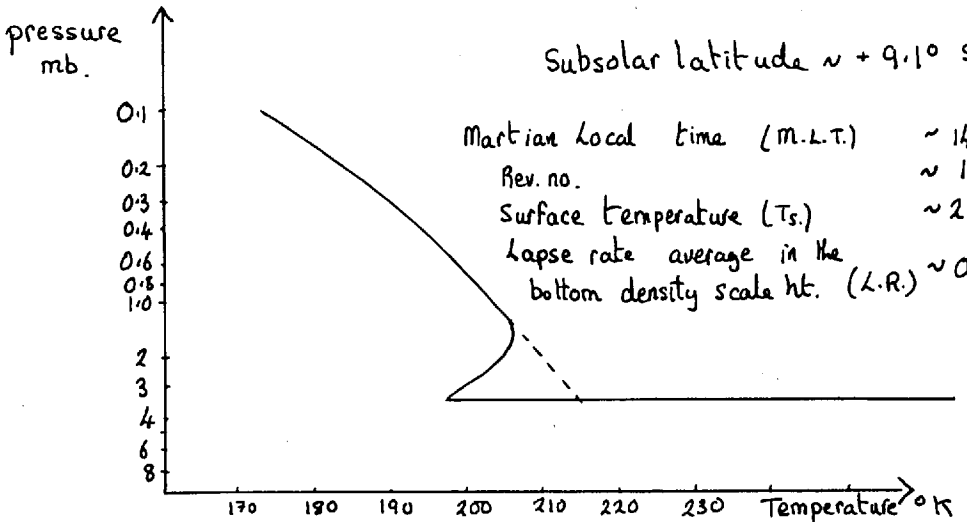

Subsolar latitude ~ + 9.1° South.

Martian Local time (M.L.T.)	~ 14·0 hrs
Rev. no.	~ 160
Surface temperature (T_s.)	~ 264·1°K
Lapse rate average in the bottom density scale ht. (L.R.)	~ 0·9°K km^{-1}

50° South

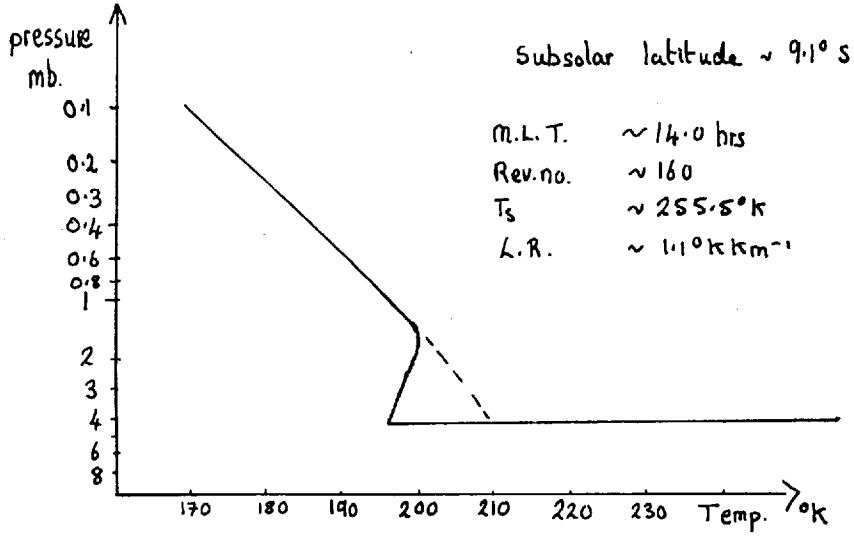

Subsolar latitude ~ 9·1° South

M.L.T.	~ 14·0 hrs
Rev.no.	~ 160
T_s	~ 255·5°K
L.R.	~ 1·1°K km^{-1}

50° South

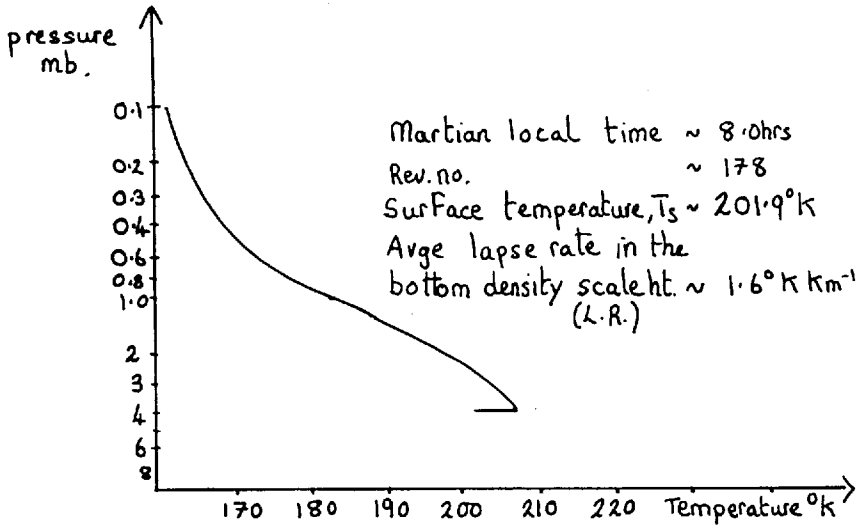

Martian local time ~ 8·0hrs
Rev. no. ~ 178
Surface temperature, T_s ~ 201·9°K
Avge lapse rate in the bottom density scale ht. ~ 1·6°K Km^{-1} (L.R.)

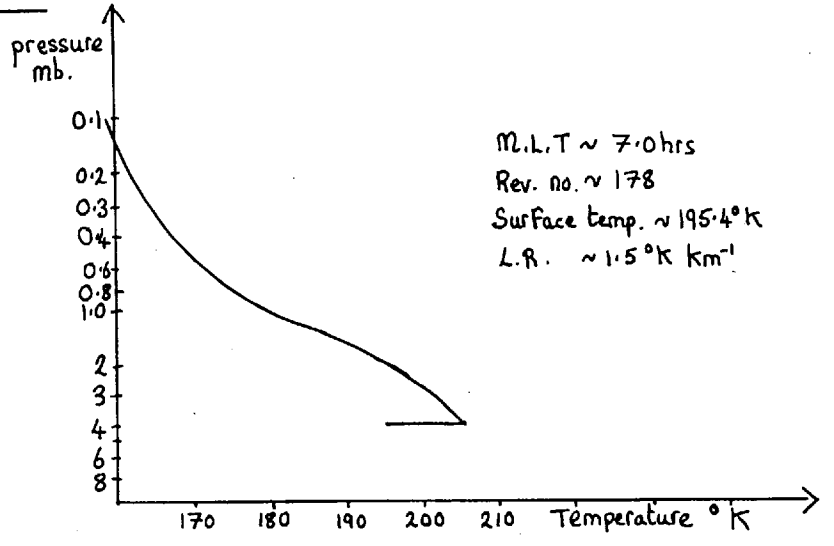

M.L.T ~ 7·0hrs
Rev. no. ~ 178
Surface temp. ~ 195·4°K
L.R. ~ 1·5°K Km^{-1}

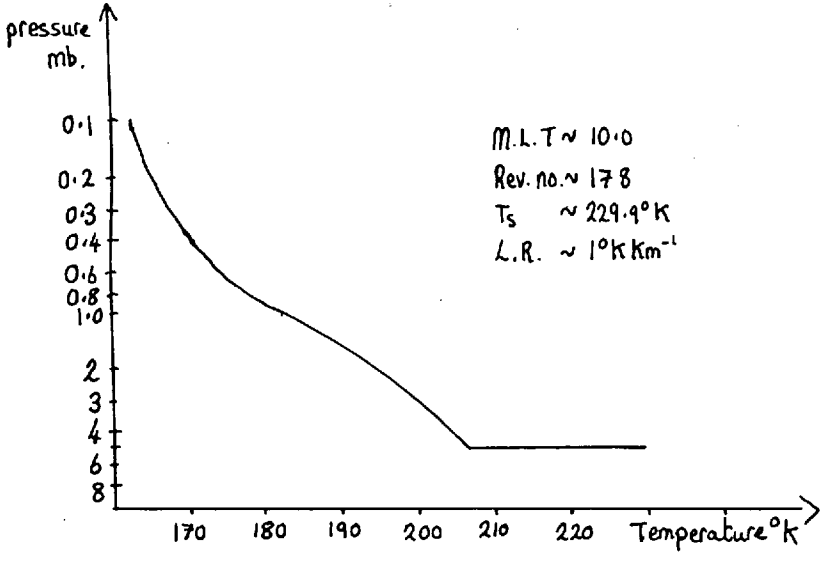

M.L.T ~ 10·0
Rev. no. ~ 178
T_s ~ 229·9°K
L.R. ~ 1°K Km^{-1}

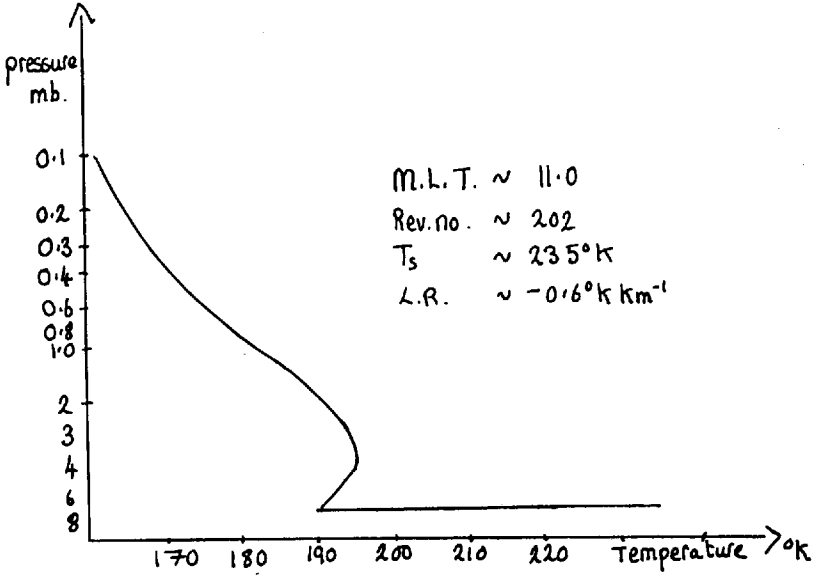

M.L.T. ~ 11·0
Rev. no. ~ 202
T_s ~ 235°K
L.R. ~ −0·6°K Km^{-1}

60° South

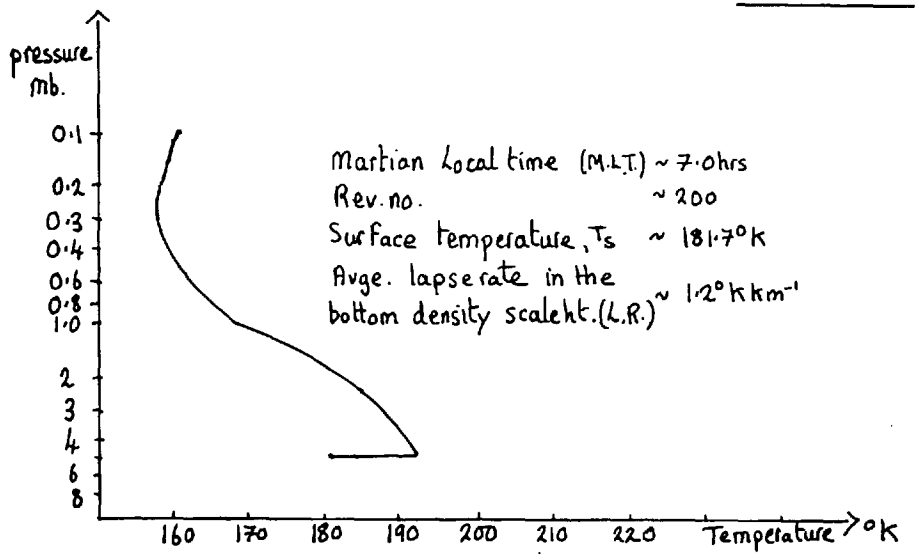

Martian Local time (M.L.T.) ~ 7·0hrs
Rev. no. ~ 200
Surface temperature, T_s ~ 181·7°K
Avge. lapse rate in the bottom density scaleht. (L.R.) ~ 1·2° K km^{-1}

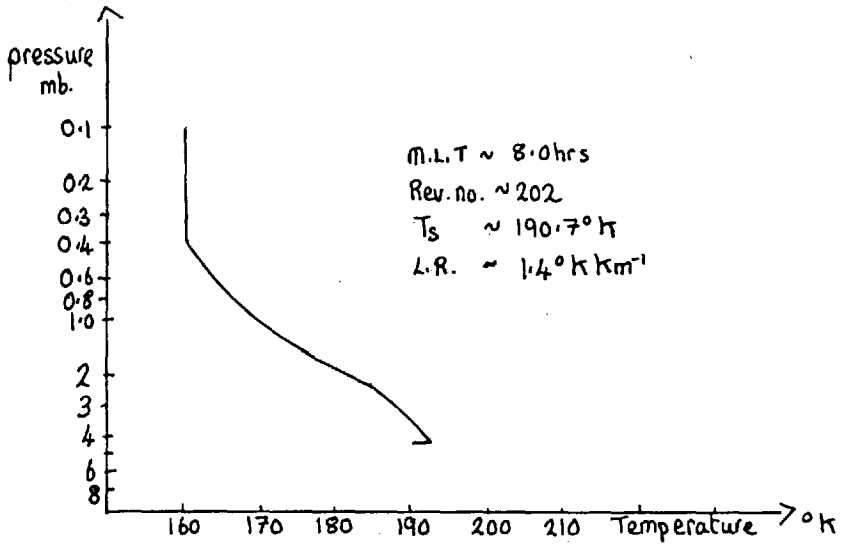

M.L.T ~ 8·0hrs
Rev. no. ~ 202
T_s ~ 190·7° K
L.R. ~ 1·4° K km^{-1}

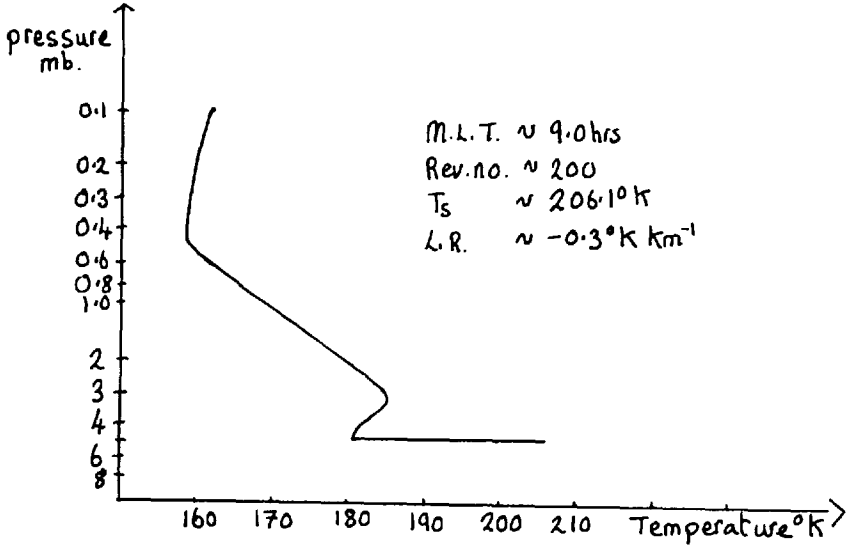

M.L.T. ~ 9·0hrs
Rev. no. ~ 200
T_s ~ 206·1° K
L.R. ~ −0·3° K km^{-1}

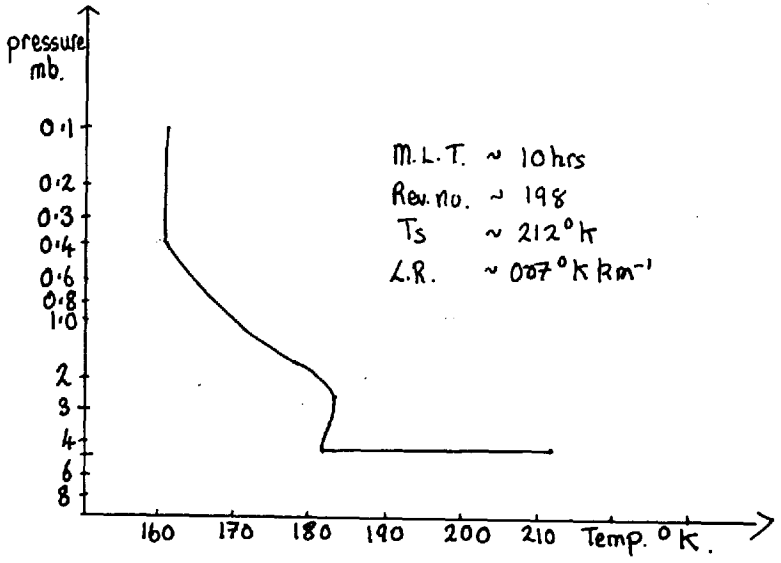

M.L.T. ~ 10hrs
Rev. no. ~ 198
T_s ~ 212° K
L.R. ~ 0·7° K km^{-1}

60° South

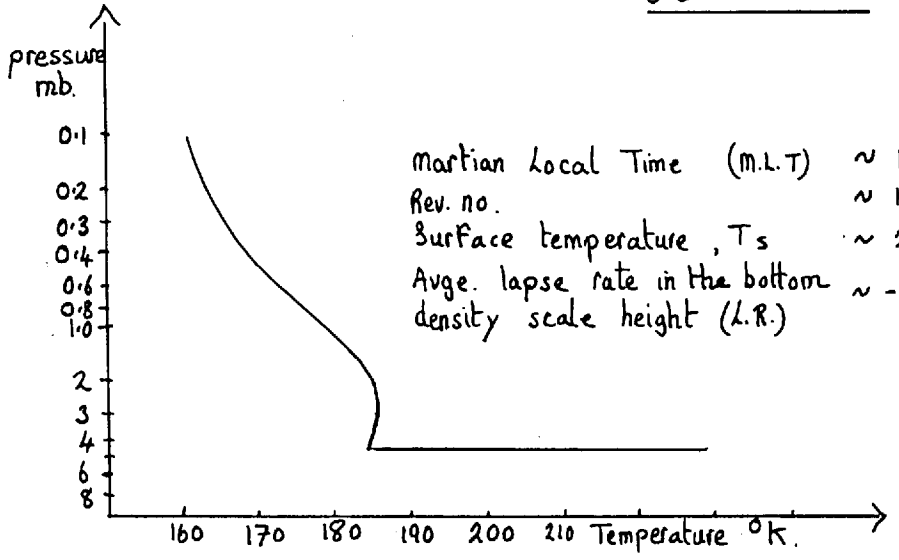

Martian Local Time (M.L.T) ~ 11·0hrs
Rev. no. ~ 186
Surface temperature, T_s ~ 229·9°K
Avge. lapse rate in the bottom density scale height (L.R.) ~ $-0{\cdot}02°K\,km^{-1}$

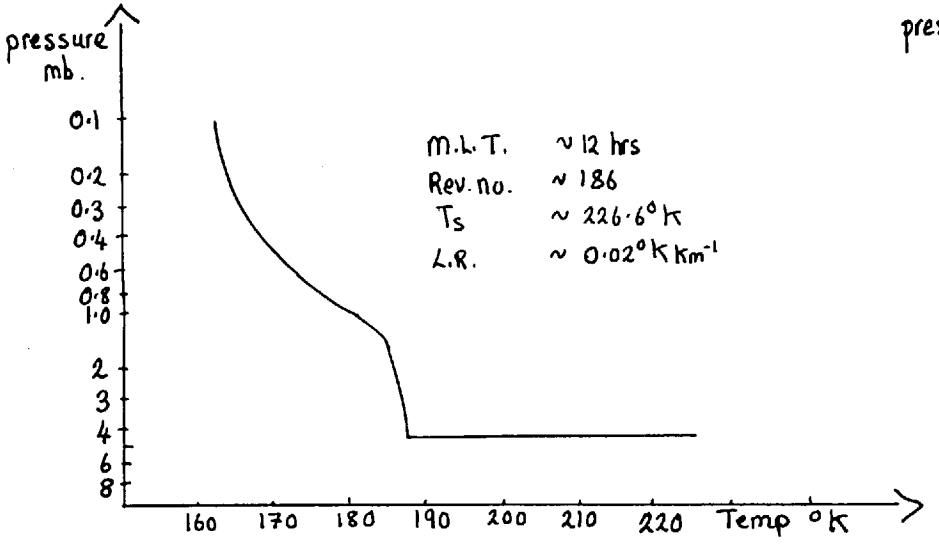

M.L.T. ~ 12 hrs
Rev. no. ~ 186
T_s ~ 226·6°K
L.R. ~ $0{\cdot}02°K\,km^{-1}$

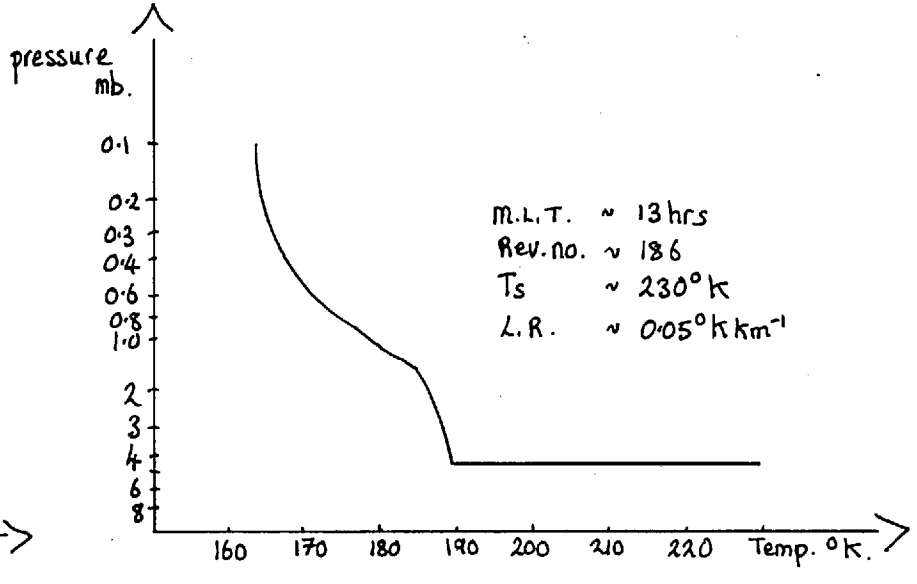

M.L.T. ~ 13 hrs
Rev. no. ~ 186
T_s ~ 230°K
L.R. ~ $0{\cdot}05°K\,km^{-1}$